



University
of Glasgow

McNicoll, Eilidh F. (2010) *Eta photoproduction study with the upgraded Glasgow tagger at MAMI*. PhD thesis

<http://theses.gla.ac.uk/1469/>

Copyright and moral rights for this thesis are retained by the author

A copy can be downloaded for personal non-commercial research or study, without prior permission or charge

This thesis cannot be reproduced or quoted extensively from without first obtaining permission in writing from the Author

The content must not be changed in any way or sold commercially in any format or medium without the formal permission of the Author

When referring to this work, full bibliographic details including the author, title, awarding institution and date of the thesis must be given

η Photoproduction Study with the Upgraded Glasgow Tagger at MAMI

Eilidh Fiona McNicoll

A thesis presented for the degree of
Doctor of Philosophy



Nuclear Physics Experiment Group
Department of Physics and Astronomy
University of Glasgow
Scotland

January 2010

Abstract

Photoproduction of mesons provides an excellent means by which to study the proton excitation spectrum. The existence and properties of some nucleon resonances are well established, but many more are still debated, meriting much theoretical and experimental attention. The proximity and widths of such excited states result in difficulties in separating contributions from individual resonances. However, the $S_{11}(1535)$ is the only state in the second resonance region to couple strongly to an $N\eta$ final state. Consequently, η production provides clean selection of this S_{11} intermediate state, for incident photons in the energy range 700 to 1400 MeV. The $S_{11}(1535)$ is a well-established resonance, but its composition is a contentious topic, requiring further experimental data to distinguish between competing theories.

The MAMI electron accelerator was upgraded in 2006 to increase its maximum beam energy from 885 to 1508 MeV. The A2 collaboration use tagged Bremsstrahlung to produce the necessary photons for photoproduction experiments. The upgrade granted access to the second resonance region of the proton excitation spectrum, which covers the centre-of-mass energy range $1.3 \lesssim W \lesssim 1.6$ GeV. This exceeds the η production threshold of $W = 1485$ MeV ($E_\gamma = 707$ MeV) and encompasses the full width of the $S_{11}(1535)$. For exclusive measurements of η photoproduction, a reasonably precise knowledge of the incident photon energy is required. This is provided for the A2 collaboration by the Glasgow Photon Tagging Spectrometer (the “tagger”). The upgrade of MAMI necessitated the corresponding upgrade of the tagger.

The work of this thesis included assisting in the upgrade and calibration of the tagger before using the completed spectrometer in the measurement of differential cross-sections of η photoproduction on the proton from threshold to 1403 MeV incident photon energy. The agreement of this analysis with previous experiments demonstrates the success of both upgrade and calibration.

Declaration

The work in this thesis is based on research carried out within the Nuclear Physics Experimental Group, Department of Physics and Astronomy, University of Glasgow, Scotland and within the A2 Collaboration at the Institut für Kernphysik, Johannes Gutenberg Universität, Mainz, Germany. No part of this thesis has been submitted elsewhere for any other degree or qualification and it is all my own work unless referenced to the contrary in the text.

Copyright © 2010 by Eilidh Fiona McNicoll.

“The copyright of this thesis rests with the author. No quotations from it should be published without the author’s prior written consent and information derived from it should be acknowledged”.

Acknowledgements

I must begin by acknowledging the support of my supervisors, Günther Rosner and John Annand. Thanks to Günther for admitting me to the Glasgow NPE group in the first instance. Thanks to John for imparting his enormous expertise at every stage — in tagger construction, analysis and thesis scrivening — and perhaps most pertinently for tolerating my excessive verbosity for four years. To my honorary supervisor, Cameron McGeorge, I will be eternally grateful — for help with technical work on and calibration of the tagger, for the most thorough and comprehensible explanations possible, for proof-reading this thesis so meticulously (in spite of being officially retired) and for advice on Munro bagging. Good luck with your last few ticks!

I have also depended greatly on the NPE technicians, Scott Lumsden and Tony Clarkson: on their technical expertise during construction of the tagger and on their excellent coffee, not to mention almond croissants and breakfast rolls. Several others have made indispensable contributions to my analysis. My thanks go to Evie Downie for invaluable assistance with *AcquRoot*, to David Hamilton for endless help with my acceptance calculation and to Bryan McKinnon for advice on fitting functions and acceptance. I am also much obliged to Ken Livingston, Bob Owens and Douglas MacGregor for weekly analytical debates and to the Glaswegian A2 students, Richard Codling, Jamie Robinson, David Howdle and Joe Mancell, for company on shift and *AcquRoot* discussions.

I am indebted to my many office-mates from the past four years: Morgan Murray, Gordon Hill, Jonathan Burns, Seian al Jebali and Jen Bowles, for their excellent company and (by and large) their forbearance of my frequent operatic outbursts. Thanks to my contemporaries, Russell Johnstone and Laurence Carson, for the

empathy and moral support that I have needed in such abundance, especially over the past year. Thanks to all of my fellow NPE students for the essential coffee breaks, the post-office tipples and that memorable excursion to Newcastle.

Collation of the data presented herein relied on the work of many members of the A2 / CB@MAMI collaboration, whose contributions I gratefully acknowledge. Particularly, I am obliged to the UCLA contingent, Sergey Prakhov, Indara Suarez, Sasha Starostin and Ben Nefkens, for being such good hosts during my visit and for all of their help with my analysis. Elsewhere in the collaboration I would like to thank Jürgen Ahrens, Olli Jahn, Michael Lang, Erik Heid, Matthias Rost, Karo Akasoy, Milorad Korolija, Dave Hornidge, Arnis Kulbardis and Michaela Thiel, variously for technical and analytical advice and for company on shifts and in Bosen.

Finally, thanks to Mum, Dad and Philip for their support and patience over the course of my PhD.

Contents

Abstract	ii
Declaration	iii
Acknowledgements	iv
1 Introduction	1
1.1 Motivation	1
1.2 Nucleon Resonances in the Reaction $\gamma p \rightarrow \eta p$	5
1.3 Reaction Models	8
1.3.1 Constituent Quark Models	8
1.3.2 Effective Lagrangian Approaches	11
1.3.3 Isobar and Reggeized Models	13
1.3.4 Chiral Effective Lagrangians	15
1.3.5 Summary	16
2 Previous Work	18
2.1 SAID Database	18
2.2 ELSA 2007	22
2.2.1 Experimental Set-up	23
2.2.2 Analysis	23
2.2.3 Results	24
2.3 GRAAL 2007	24
2.3.1 Experimental Set-up	24
2.3.2 Analysis	25

2.3.3	Results	27
2.4	A2 2007	28
3	Bremsstrahlung and the Glasgow-Mainz Photon Tagging Spectrometer	29
3.1	Tagging	29
3.2	Goniometer and Photon Television	30
3.3	Tagger History	31
3.4	Dipole	31
3.4.1	Vacuum Window	33
3.4.2	Field Inhomogeneities	34
3.4.3	Nuclear Magnetic Resonance Probe	35
3.4.4	Field Settling Time	35
3.4.5	Stray Magnetic Field	36
3.5	Focal Plane Detector and Tagger Electronics	37
3.5.1	Scintillator Tests	42
3.5.2	A/D Card Tests	42
3.5.3	Refurbishing the Focal Plane Detector	44
3.5.4	Cabling: HV Supply, LV Supply and Signal Read-Out	45
3.6	Beam Collimation and Tagging Efficiency	48
3.7	Energy Calibration	49
3.7.1	MAMI Data	49
3.7.2	Calculation	51
4	Experimental Set-Up	57
4.1	Overview	57
4.2	MAMI	58
4.2.1	MAMI Race Track Microtron Cascade	59
4.2.2	Harmonic Double-Sided Microtron	60
4.3	Target	62
4.4	Crystal Ball System	63
4.4.1	Crystal Ball	64

4.4.2	Particle Identification Detector	67
4.5	TAPS	68
4.5.1	BaF ₂ Crystals	69
4.5.2	Veto Counters	70
4.6	Data Acquisition	71
4.6.1	Crystal Ball Electronics	71
4.6.2	PID Electronics	72
4.6.3	TAPS Electronics	72
4.6.4	Triggers	73
4.6.5	DAQ Control	73
5	Data Analysis	76
5.1	Detector Calibration	76
5.1.1	Tagger	76
5.1.2	Crystal Ball	77
5.1.3	PID	77
5.2	Event Reconstruction and Identification	78
5.2.1	Random Subtraction	78
5.2.2	Event Reconstruction	79
5.2.3	Particle Identification	79
5.3	η Photoproduction Differential Cross-Sections	80
5.4	Constant Factors	81
5.4.1	Branching Ratios	81
5.4.2	Effective Target Thickness	82
5.5	Photon Flux	82
5.6	Yield Extraction	84
5.6.1	Event Selection	84
5.6.2	Energy and Angular Dependent η Yields	86
5.6.3	Corrected Yield	88
5.7	Acceptance Determination	88
5.7.1	Event Generation	89
5.7.2	Experimental Model	89

5.7.3	Physics Analysis	90
5.7.4	Acceptance Calculation	92
5.8	2D Differential Cross-Sections	92
5.9	Error Evaluation	93
5.9.1	Statistical Uncertainties	93
5.9.2	Systematic Uncertainties	94
6	Results and Discussion	95
6.1	η Photoproduction Differential Cross-Sections	95
6.1.1	Results	95
6.1.2	Comparison with Previous Data	99
6.2	Tagger Upgrade Appraisal	102
6.3	Conclusions	103
	Bibliography	105
	Appendix	115
A	Definitions	115
A.1	Quantum Numbers	115
A.2	Properties of Particles and Resonances	116
A.3	Mandelstam Variables	117
A.4	Electric and Magnetic Multipoles	118
A.5	η Electroproduction	119
B	Tables of $\eta \rightarrow 2\gamma$ Results	120
C	Tables of $\eta \rightarrow 6\gamma$ Results	138

List of Figures

1.1	Cross-section for total photoabsorption on the proton [6].	2
1.2	Total and partial photoabsorption cross-sections for photoproduction on the proton.	7
1.3	Contributions of resonances to π^0 and η photoproduction [13].	8
1.4	Schematic of nucleon excitations [13].	9
1.5	Tree-level contributions to η photoproduction [25].	12
1.6	Regge trajectories of ω and ρ mesons.	14
2.1	(θ_η, E_γ) range covered by measurements of η photoproduction differ- ential cross-sections, as listed in the SAID database [40].	19
2.2	Experimental set-up at ELSA [58].	23
2.3	Experimental set-up at GRAAL [59].	25
2.4	Comparison of differential cross-section measurements from GRAAL and CB-ELSA.	26
2.5	Comparison of total cross-section estimates [59] from GRAAL, CLAS, CB-ELSA and LNS-GeV- γ	27
3.1	Schematic of the photon camera system.	30
3.2	Upgraded tagger magnet.	32
3.3	3D model and cross-section of the upgraded tagger magnet [5].	33
3.4	Schematic of the lower pole and FPD array.	34
3.5	Measurement and TOSCA prediction of the tagger field.	35
3.6	Settling time of the tagger dipole field, with a dipole current of 132 A.	36
3.7	Schematic of a focal plain detector section.	37
3.8	Various widths of scintillator through the stages of wrapping.	38

3.9	Circuit diagram of the amplifier-discriminator cards [5].	39
3.10	Tagger electronics rack.	40
3.11	Schematic of the tagger electronics rack [71].	41
3.12	Schematic of the A/D card test setup [72].	42
3.13	Diagram of a tagger A/D card, with test points highlighted in blue [72].	43
3.14	Specimen scope display for LVDS ₊ - LVDS ₋ , A2 and TP1 signals. . .	43
3.15	The focal plane detector frame and scintillators mounted therein. . .	44
3.16	A/D Cards mounted in the FPD frame.	45
3.17	The tagger from above.	47
3.18	The completed Glasgow-Mainz Photon Tagging Spectrometer.	48
3.19	Channel hit against tagger dipole field for the 1002 MeV electron beam.	50
3.20	Initial tagger calibration calculation.	52
3.21	Effective uniform field.	53
3.22	Position of the effective field boundary.	54
3.23	Final tagger energy calibration.	55
3.24	Deviation in electron trajectories caused by dips in the magnetic field.	56
4.1	Schematic of MAMI and the experimental halls [78].	58
4.2	Schematic of a race track microtron [78].	59
4.3	Schematic of the harmonic double sided microtron [78].	61
4.4	Liquid hydrogen target cell [80].	62
4.5	Schematic of the target cell [80].	63
4.6	Schematic of the detector system.	64
4.7	Crystal Ball.	65
4.8	Geometry of the Crystal Ball.	66
4.9	A truncated pyramidal <i>NaI(Tl)</i> crystal from the Crystal Ball.	66
4.10	Particle Identification Detector [89].	67
4.11	Schematic of the Particle Identification Detector [89].	68
4.12	TAPS.	69
4.13	An hexagonal <i>BaF₂</i> crystal from TAPS.	70
4.14	Schematic of the Crystal Ball read-out electronics [90].	71
4.15	Schematic of TAPS read-out electronics [95].	73

4.16	Tagger triggering diagram [71].	74
4.17	Crystal Ball triggering diagram [96].	75
5.1	PID calibration plots.	78
5.2	Time OR of tagger TDC hits.	79
5.3	A cluster within the CB [85].	80
5.4	Scaler counts, average tagging efficiency and photon flux.	83
5.5	Invariant mass distributions of 2γ pairs and 6γ events.	84
5.6	m_{miss} for all accepted $\eta \rightarrow 2\gamma$ and $\eta \rightarrow 6\gamma$ events.	85
5.7	m_{miss} against T_{ch} against $\cos\theta_\eta^*$ for 2γ events.	86
5.8	m_{miss} fit.	86
5.9	Y_η as a function of E_γ and $\cos\theta_\eta^*$ for the 2γ and 6γ decays.	87
5.10	Corrected Y_η for the 2γ and 6γ decay modes.	88
5.11	Generated η events for the 2γ and 6γ decay modes.	89
5.12	<i>A2</i> simulation representation of the CB and TAPS detectors [107]. . .	90
5.13	η mass peak in the invariant mass for experimental and simulated data.	91
5.14	Monte Carlo m_{miss} versus E_γ against $\cos\theta_\eta^*$ from <i>AcquRoot</i> analysis. .	91
5.15	Monte Carlo Y_η as a function of E_γ and $\cos\theta_\eta^*$ after full analysis. . .	91
5.16	Acceptance as a function of E_γ and $\cos\theta_\eta^*$	92
5.17	$\frac{d\sigma}{d\Omega}$, in $\mu\text{b}/\text{sr}$, as a function of E_γ and $\cos\theta_\eta^*$	93
6.1	$\frac{d\sigma}{d\Omega}$ as a function of $\cos\theta_\eta^*$ for E_γ in the range 718 to 1100 MeV.	96
6.2	$\frac{d\sigma}{d\Omega}$ as a function of $\cos\theta_\eta^*$ for E_γ in the range 1124 to 1395 MeV.	97
6.3	Integrated cross-section as a function of E_γ for the 2γ decay.	98
6.4	Comparison of $\frac{d\sigma}{d\Omega}$ for E_γ in the range 718 to 1110 MeV between results of the present work, GRAAL [59] and the SAID fit [40].	100
6.5	Comparison of $\frac{d\sigma}{d\Omega}$ for E_γ in the range 1124 to 1395 MeV.	101
6.6	Tagger scalers from April 2009 [109].	103
A.1	4-momenta of particles in a scattering process for which Mandelstam variables are defined.	118
A.2	Feynman diagrams for s , t and u -channels.	118

List of Tables

1.1	Properties of the η meson [7].	3
1.2	Properties of the most firmly established N^* resonances [7] within the energy range of the present work.	6
3.1	LV PSU voltages, currents and limits thereof [71].	46
4.1	Parameters of MAMI RTMs [78].	60
B.1	Minimum, maximum and flux-weighted average values for each incident photon energy bin.	121
B.2	Minimum, maximum and average values for each $\cos\theta_\eta^*$ bin used in the 2γ analysis.	122
B.3	$\frac{d\sigma}{d\Omega}$ for $E_\gamma = 718$ and 747 MeV from the $\eta \rightarrow 2\gamma$ decay mode.	123
B.4	$\frac{d\sigma}{d\Omega}$ for $E_\gamma = 788$ and 805 MeV from the $\eta \rightarrow 2\gamma$ decay mode.	124
B.5	$\frac{d\sigma}{d\Omega}$ for $E_\gamma = 833$ and 863 MeV from the $\eta \rightarrow 2\gamma$ decay mode.	125
B.6	$\frac{d\sigma}{d\Omega}$ for $E_\gamma = 890$ and 918 MeV from the $\eta \rightarrow 2\gamma$ decay mode.	126
B.7	$\frac{d\sigma}{d\Omega}$ for $E_\gamma = 945$ and 972 MeV from the $\eta \rightarrow 2\gamma$ decay mode.	127
B.8	$\frac{d\sigma}{d\Omega}$ for $E_\gamma = 999$ and 1024 MeV from the $\eta \rightarrow 2\gamma$ decay mode.	128
B.9	$\frac{d\sigma}{d\Omega}$ for $E_\gamma = 1050$ and 1075 MeV from the $\eta \rightarrow 2\gamma$ decay mode.	129
B.10	$\frac{d\sigma}{d\Omega}$ for $E_\gamma = 1100$ and 1124 MeV from the $\eta \rightarrow 2\gamma$ decay mode.	130
B.11	$\frac{d\sigma}{d\Omega}$ for $E_\gamma = 1147$ and 1171 MeV from the $\eta \rightarrow 2\gamma$ decay mode.	131
B.12	$\frac{d\sigma}{d\Omega}$ for $E_\gamma = 1193$ and 1215 MeV from the $\eta \rightarrow 2\gamma$ decay mode.	132
B.13	$\frac{d\sigma}{d\Omega}$ for $E_\gamma = 1236$ and 1257 MeV from the $\eta \rightarrow 2\gamma$ decay mode.	133
B.14	$\frac{d\sigma}{d\Omega}$ for $E_\gamma = 1277$ and 1297 MeV from the $\eta \rightarrow 2\gamma$ decay mode.	134
B.15	$\frac{d\sigma}{d\Omega}$ for $E_\gamma = 1315$ and 1338 MeV from the $\eta \rightarrow 2\gamma$ decay mode.	135

B.16	$\frac{d\sigma}{d\Omega}$ for $E_\gamma = 1358$ and 1380 MeV from the $\eta \rightarrow 2\gamma$ decay mode.	136
B.17	$\frac{d\sigma}{d\Omega}$ for $E_\gamma = 1396$ MeV from the $\eta \rightarrow 2\gamma$ decay mode.	137
C.1	Minimum, maximum and average values for each $\cos\theta_\eta^*$ bin used in the 6γ analysis.	139
C.2	$\frac{d\sigma}{d\Omega}$ for $E_\gamma = 718$ and 747 MeV from the $\eta \rightarrow 6\gamma$ decay mode.	139
C.3	$\frac{d\sigma}{d\Omega}$ for $E_\gamma = 778$ and 805 MeV from the $\eta \rightarrow 6\gamma$ decay mode.	140
C.4	$\frac{d\sigma}{d\Omega}$ for $E_\gamma = 833$ and 863 MeV from the $\eta \rightarrow 6\gamma$ decay mode.	140
C.5	$\frac{d\sigma}{d\Omega}$ for $E_\gamma = 890$ and 918 MeV from the $\eta \rightarrow 6\gamma$ decay mode.	141
C.6	$\frac{d\sigma}{d\Omega}$ for $E_\gamma = 945$ and 972 MeV from the $\eta \rightarrow 6\gamma$ decay mode.	141
C.7	$\frac{d\sigma}{d\Omega}$ for $E_\gamma = 999$ and 1024 MeV from the $\eta \rightarrow 6\gamma$ decay mode.	142
C.8	$\frac{d\sigma}{d\Omega}$ for $E_\gamma = 1050$ and 1075 MeV from the $\eta \rightarrow 6\gamma$ decay mode.	142
C.9	$\frac{d\sigma}{d\Omega}$ for $E_\gamma = 1100$ and 1124 MeV from the $\eta \rightarrow 6\gamma$ decay mode.	143
C.10	$\frac{d\sigma}{d\Omega}$ for $E_\gamma = 1147$ and 1171 MeV from the $\eta \rightarrow 6\gamma$ decay mode.	143
C.11	$\frac{d\sigma}{d\Omega}$ for $E_\gamma = 1193$ and 1215 MeV from the $\eta \rightarrow 6\gamma$ decay mode.	144
C.12	$\frac{d\sigma}{d\Omega}$ for $E_\gamma = 1236$ and 1257 MeV from the $\eta \rightarrow 6\gamma$ decay mode.	144
C.13	$\frac{d\sigma}{d\Omega}$ for $E_\gamma = 1277$ and 1297 MeV from the $\eta \rightarrow 6\gamma$ decay mode.	145
C.14	$\frac{d\sigma}{d\Omega}$ for $E_\gamma = 1315$ and 1338 MeV from the $\eta \rightarrow 6\gamma$ decay mode.	145
C.15	$\frac{d\sigma}{d\Omega}$ for $E_\gamma = 1358$ and 1380 MeV from the $\eta \rightarrow 6\gamma$ decay mode.	146
C.16	$\frac{d\sigma}{d\Omega}$ for $E_\gamma = 1396$ MeV from the $\eta \rightarrow 6\gamma$ decay mode.	146

Chapter 1

Introduction

1.1 Motivation

While the *Collins Gem English Dictionary* [1] defines a resonance merely as “echoing”, the *Oxford English Dictionary* [2] entry reads:

“**resonance** *n* **d.** (*iv*) *spec.* in *Nuclear Physics*, a short-lived particle or an excited state of a particle, manifested as an increase, at certain well-defined energies, in the probability of interaction of other particles.”

The proton excitation spectrum, shown in figure 1.1 contains contributions from many such resonances. The first, second and third resonance regions correspond to the three peaks in this spectrum, in ascending order of invariant mass. The existence and properties of some resonances are well established, but many more are still debated, meriting much theoretical and experimental attention. Traditionally, studies of the nucleon excitation spectra have centred on probing the first resonance region using pion beams [3]. This has led to a bias in knowledge in favour of resonances with large pion couplings.

Photoproduction of mesons, in spite of much lower cross-sections, provides an alternative approach without the complex initial state interaction effects arising from a strongly interacting hadronic probe [4]. For exclusive measurements of photoproduction reactions, a reasonably precise knowledge of the incident photon energy is required. Such measurements are the mainstay of experimental work within the

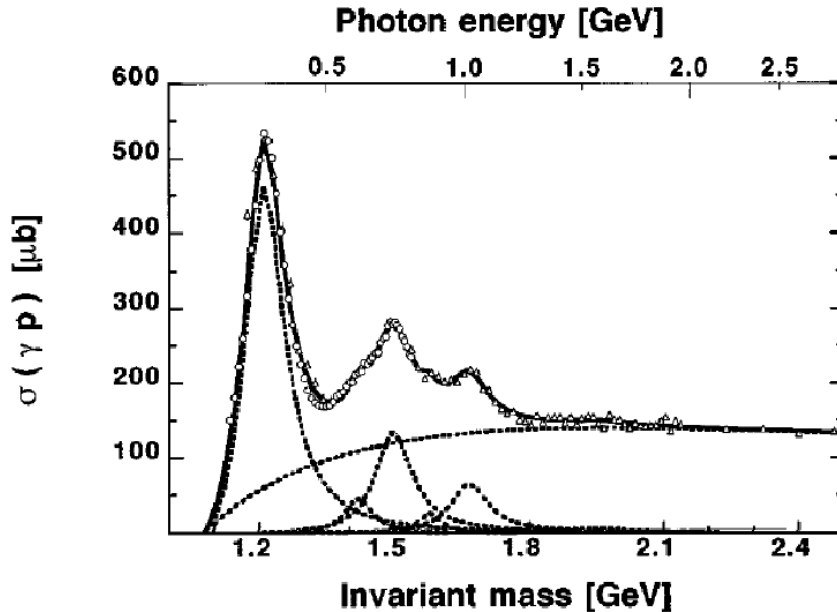


Figure 1.1: Cross-section for total photoabsorption on the proton as a function of invariant mass [6]. Points: experimental data. Curves: $P_{33}(1232)$, $P_{11}(1440)$, $D_{13}(1520)$, $S_{11}(1535)$, $F_{15}(1680)$ and $F_{37}(1950)$ resonances and a smoothly varying background.

A2 collaboration at the Mainzer Mikrotron (MAMI), Germany. Here, photons are produced using tagged Bremsstrahlung, by impinging an electron beam on a radiator, as described in section 3.1. Tagging is performed using the Glasgow-Mainz Photon Tagging Spectrometer, the “tagger”. In 2005, the upgrade of the maximum electron beam energy, E_{e^-} , from 885 to 1508 MeV made a corresponding upgrade of the tagger necessary [5]. The successful completion of this granted access to the complete second resonance region of the proton excitation spectrum, covering the centre-of-mass energy range $1.3 \lesssim W \lesssim 1.6$ GeV.

This region, as shown in figure 1.1, contains several overlapping resonances — the most prominent of which are the $P_{11}(1440)$, $D_{13}(1520)$ and $S_{11}(1535)$ (see section 1.2 for details of resonance notation). This makes discrimination between them potentially difficult. However, of these, only the $S_{11}(1535)$ couples strongly to the $N\eta$ channel, with 45–60% of its decays having this final state [7]. Consequently, η production provides clean selection of the $S_{11}(1535)$ intermediate state.

Property	Value
Mass	$(547.51 \pm 0.18) \text{ MeV}$
Valence Quarks	$\frac{1}{\sqrt{6}}(u\bar{u} + d\bar{d} - 2s\bar{s})$
Lifetime	$< 10^{-18} \text{ s}$
Charge (Q)	0
Isospin (I)	0
I_3	0
Orbital Angular Momentum (L)	0
Total Angular Momentum (J)	0
Strangeness (S)	0
Parity (P)	-
Charge Conjugation (C)	+

Table 1.1: Properties of the η meson [7].

The η is a pseudoscalar meson, with properties as detailed in table 1.1 [7]. Quantum numbers are defined in section A.1. It is a member of the meson nonet and is its own anti-particle. The η has no net strangeness, but does have strange quark content [8].

The existence of the $S_{11}(1535)$ is well established — the Particle Data Group (PDG) [7] assigns a maximum 4-star status to it — but some of its properties cannot yet be explained definitively. One example is the anomalously strong $S_{11}(1535)$ to $N\eta$ coupling. The third resonance region ($1.6 \lesssim W \lesssim 1.8 \text{ MeV}$) contains the next highest mass S -wave resonance, the $S_{11}(1650)$. This shares the same internal quantum numbers as the $S_{11}(1535)$, yet has a far smaller branching ratio for decay to $N\eta$ of only 3–10%. A conclusive explanation of this difference has yet to be agreed upon. This has led to debate as to the nature of the $S_{11}(1535)$: whether it is in fact a standard tri-quark state [9], a quark-diquark configuration [10] or a $K\Sigma$ molecule [11]. Further data on η photoproduction may help to explain the $S_{11}\eta$ coupling and to differentiate between conflicting models.

Analyses of previous experimental data, described in chapter 2, indicate that contributions to the total photoproduction cross-section of $\gamma p \rightarrow \eta p$ are dominated by coupling to the $S_{11}(1535)$ from threshold, at $E_\gamma = 707$ MeV, up to 900 MeV [12] with smaller contributions from higher mass resonances. At higher energy, vector meson (ρ and ω) exchange in the t -channel comes into play, along with lesser effects from Born terms. These processes constitute the non-resonant background in η photoproduction. In Born terms, the $N\eta$ final state is produced directly from the proton with no intermediate excitation. In ρ or ω exchange, the photon converts itself into said vector meson — with four-momentum t as defined in section A.3 — before interacting with the proton [6].

The proton can be excited to the S_{11} using photons with energies $E_\gamma \geq 707$ MeV [8], producing the reaction:

$$\gamma p \rightarrow S_{11}(1535) \rightarrow \eta p \quad (1.1)$$

The $S_{11}(1535)$ and η , having respective lifetimes of $\sim 10^{-24}$ s and $< 10^{-18}$ s, decay before detection. Of the various decays of the η , 72% occur via the following neutral modes:

$$\eta \rightarrow 2\gamma \quad (1.2)$$

$$\eta \rightarrow 3\pi^0 \rightarrow 6\gamma \quad (1.3)$$

with branching ratios of $(39.39 \pm 0.24)\%$ and $(32.52 \pm 0.26)\%$ respectively. Since the CB and TAPS detectors used within the A2 Hall (see chapter 4) are optimally used as photon calorimeters, these channels were analysed.

The two main aims of this thesis work were to assist in the upgrade of the Glasgow-Mainz Photon Tagging Spectrometer and to measure the differential cross-section of η photoproduction on the proton. The latter being a previously studied reaction allowed comparison to previous data, enabling an assessment of the tagger upgrade, while providing an increase in statistics for this reaction. Forward angular coverage was extended relative to previous measurement, improving the database from which partial wave analyses are performed, thus potentially aiding discrimination between competing phenomenological models, as described in section 1.3.

1.2 Nucleon Resonances in the Reaction $\gamma p \rightarrow \eta p$

Quantum Chromodynamics (QCD) is the accepted theory of the strong interaction. Perturbative QCD describes the high energy regime well, where quark-gluon interactions are relatively weak, allowing solution of the QCD Lagrangian by perturbative methods. However, this does not hold at lower energies around the nucleon mass, when the strong coupling constant, α_s , is too large for perturbative treatments. Lattice QCD promises the eventual solution to this problem, but at present realistic calculations of *uds*-quark baryon properties are beyond the available computing resources. Effective field theories, which employ meson-baryon — as opposed to quark-gluon — degrees of freedom, represent low energy approximations to QCD. Notably chiral perturbation theory, which embodies the (broken) chiral symmetry of QCD, has been highly successful in describing near-threshold meson production. However, its range of applicability is strictly limited to the low energy regime. For other situations, various phenomenological models exist, a selection of which are described in section 1.3. These agree that the $S_{11}(1535)$ resonance is dominant in η photoproduction, but predict different contributions from other excited states.

Resonances are labelled using the notation:

$$L_{2I2J}(W),$$

where W , I and J are, respectively, the mass in MeV, the isospin and the spin of the resonance; $L = 0, 1, 2, \dots$ is the angular momentum for decay to $N\pi$, denoted S, P, D, \dots in spectroscopic notation [13].

As mentioned in section 1.1, many individual resonances contribute to the inclusive photoexcitation spectrum of the proton, shown in figure 1.1. In all, the PDG [7], lists 22 N^* resonances, with $I = \frac{1}{2}$, and 22 Δ resonances, with $I = \frac{3}{2}$. Isospin selectivity forbids decay from a Δ state to $N\eta$. The W range of the present work was 1483 to 1874 MeV, corresponding to a photon energy range of $703 \leq E_\gamma \leq 1403$ MeV, covering the 9 N^* states listed in table 1.2. “Status” is assessed on a scale of 1 to 4, both overall — *ie.* considering experimental evidence from all reactions producing the given resonance — and specifically in decays to an $N\eta$ final state. Further resonance properties are summarised in section A.2.

Resonance	Status	$N\eta$ Status	Mass (MeV)	Γ (MeV)	$N\eta$ Decay %
$P_{11}(1440)$	****	*	1420-1470	200-450	
$D_{13}(1520)$	****	***	1515-1525	100-125	$(0.23 \pm 0.04) \%$
$S_{11}(1535)$	****	****	1525-1545	125-175	45–60 %
$S_{11}(1650)$	****	*	1645-1670	145-185	3–10 %
$D_{15}(1675)$	****	*	1670-1860	130-165	$(0.0 \pm 1.0) \%$
$F_{15}(1680)$	****	*	1680-1690	120-140	$(0.0 \pm 1.0) \%$
$D_{13}(1700)$	***	*	1650-1750	50-150	$(0.0 \pm 1.0) \%$
$P_{11}(1710)$	***	**	1680-1740	50-250	$(6.2 \pm 1.0) \%$
$P_{13}(1720)$	****	*	1700-1750	150-300	$(4.0 \pm 1.0) \%$

Table 1.2: Properties of the most firmly established N^* resonances [7] within the energy range of the present work.

Clearly, the main resonance contribution to η photoproduction is the $S_{11}(1535)$. Other resonances are estimated to contribute below 10% [7]. Close to the η production threshold of $E_\gamma = 707$ MeV, resonances dominate this process. The non-resonant background due to vector meson exchange and Born terms is negligible at this energy.

The $S_{11}(1535)$ lies in the second resonance region of the proton photoexcitation spectrum which covers the invariant mass range $1350 \lesssim W \lesssim 1600$ MeV, corresponding to incident photon energies of $500 \lesssim E_\gamma \lesssim 900$ MeV. While the first peak region is due entirely to the $\Delta(1232)$, the second region contains three resonances — $P_{11}(1440)$, $D_{13}(1520)$ and $S_{11}(1535)$ — as well as the high energy tail of the low-lying $\Delta(1232)$ and low energy tails of the 5 higher energy N^* states, in addition to background terms.

The measured total and partial photoabsorption cross-sections for different channels is shown in figure 1.2. Whereas the cross-section in the first resonance region arises predominantly from single pion production, the second resonance region is above the threshold for double pion and η production, complicating matters. Although η production has a relatively small cross-section compared to the total, it

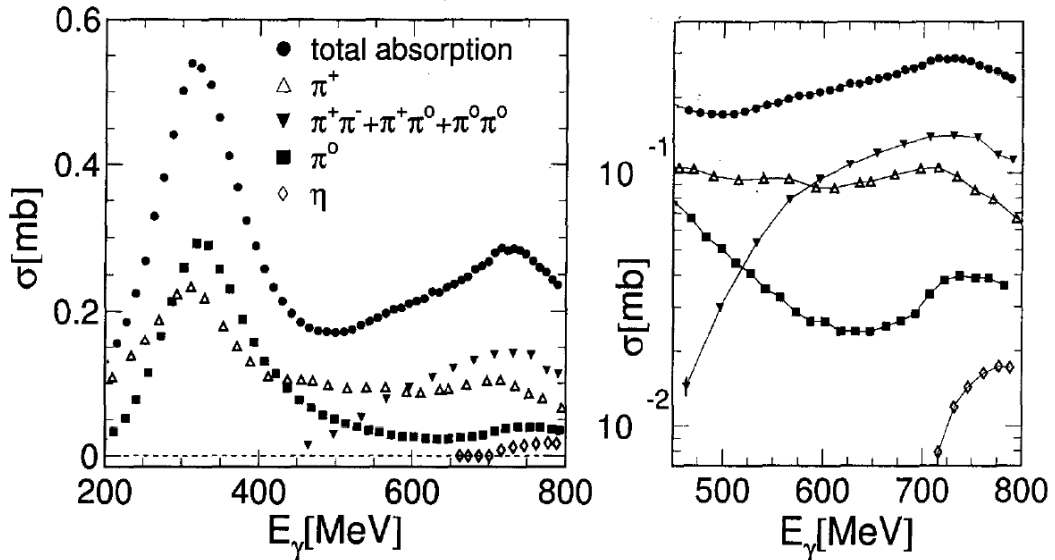


Figure 1.2: Total and partial photoabsorption cross-sections for photoproduction on the proton, reproduced from [13]. Data are from [4, 14–18].

is critical to the study of the $S_{11}(1535)$. Figure 1.3 shows predicted contributions of excited states around the second resonance region to π^0 and η photoproduction. These are calculated from the masses, widths, photon couplings and decay branching ratios of the relevant Δ and N^* resonances [13]. The $S_{11}(1535)$ evidently dominates η photoproduction, with a small contribution from the $S_{11}(1650)$. This suggests that other resonances are negligible in this process.

Many properties of the $S_{11}(1535)$ have been well studied [7]. In addition to those summarised in table 1.2, it has isospin (I), spin (J) and parity (P):

$$I(J^P) = \frac{1}{2} \left(\frac{1^-}{2} \right).$$

as suggested by the spectroscopic notation. However, the structure of the $S_{11}(1535)$ is a contentious topic. As noted in section 1.1, its coupling to the $N\eta$ channel is anomalously high and a number of models have been formulated in an effort to explain this. These models are discussed in section 1.3.

The differential cross-section is one of 16 physical observables which can be measured in a complete experiment in photoproduction of pseudoscalar mesons [19]. The other 15, termed polarisation observables, require polarisation of beam, target or recoil particle. Differential cross-sections with respect to solid angle, $\frac{d\sigma}{d\Omega}$, quan-

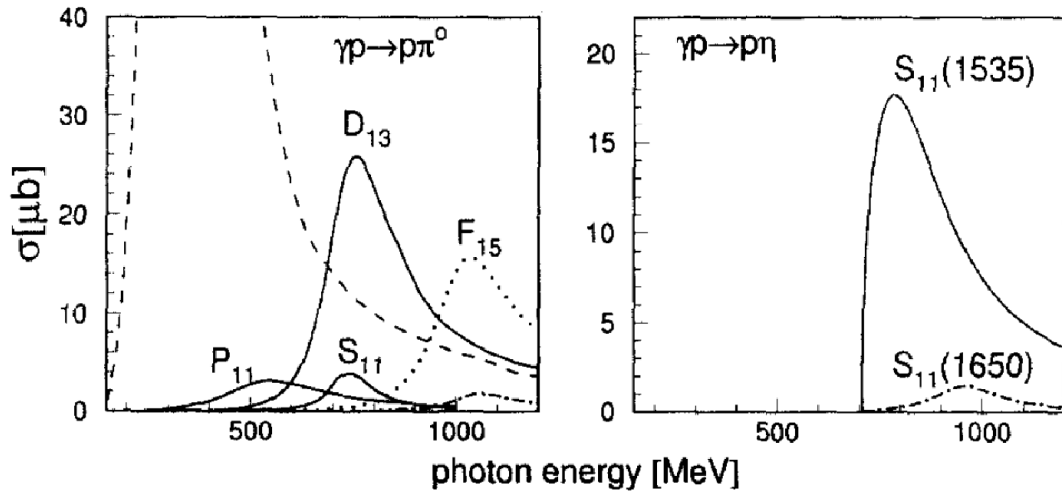


Figure 1.3: Contributions of resonances to π^0 and η photoproduction [13].

tify the probability of occurrence of the given reaction over a certain range in $\cos \theta^*$ for a chosen invariant mass range. Here θ^* is the meson polar production angle in the centre-of-mass frame. Angular distributions of differential cross-sections provide information on the reaction mechanism and can be integrated to give total cross-sections. These data, along with other observables, can be used in partial wave analyses to study the partial waves contributing to the reaction of interest and the excitation properties.

1.3 Reaction Models

Manifold phenomenological models covering η photoproduction have been developed [13]. A selection of these is reviewed in this section including constituent quark models [10,20–24], effective Lagrangian approach models [4,25,26], isobar models [27, 28], Reggeized models [3,29–31] and chiral effective Lagrangian models [11,32,33].

1.3.1 Constituent Quark Models

Constituent quark models (CQMs) start from the basis of nucleons containing three constituent quarks in a collective potential. While the nucleon mass is ~ 1 GeV, the physical u and d quark masses are a few MeV, indicating that most nucleon

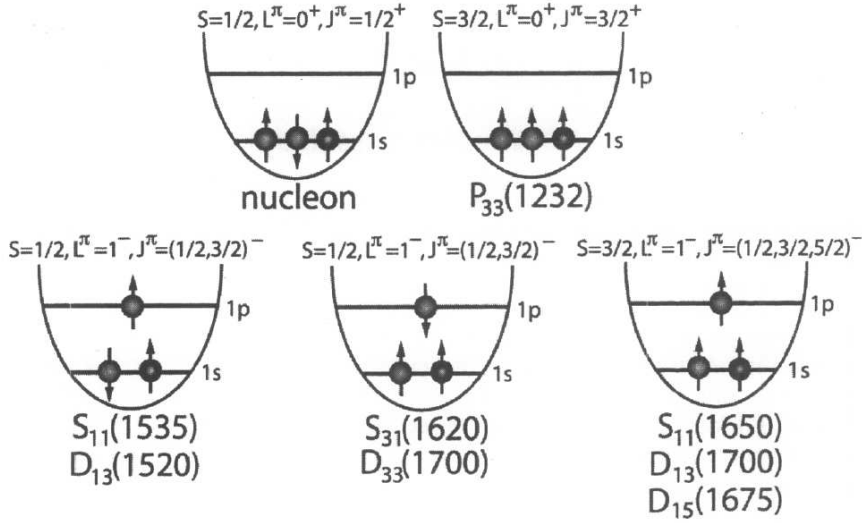


Figure 1.4: Schematic of nucleon excitations [13].

mass results from quark dynamics and colour interactions. CQMs absorb these effects into unphysically large, model-dependent quark masses, with values starting from ~ 220 MeV in relativistic models, increasing to ~ 330 MeV in non-relativistic pictures [13]. Constituent quarks are not point-like, but have electric and strong form factors. The collective potential stems from a confining interaction, with quark–quark forces governed by a residual short range interaction, termed the fine-structure interaction. The form of each of these interactions varies between models. In the simplest models, the constituent quarks are treated non-relativistically and interact with a mean field (due to the other quarks) described by an harmonic oscillator potential, as depicted in figure 1.4.

The number of excited states in a quark model is determined by the effective degrees of freedom. Their masses and decay couplings depend upon the fine-structure interaction [7]. Many more nucleon resonances have been predicted by quark models than observed experimentally, a situation dubbed the “missing resonance” problem.

Work by Saghai *et al.* [20] used a chiral constituent quark model to examine baryon resonances via η photoproduction. The quark model with exact $SU(6) \otimes O(3)$ symmetry provided a basis to which symmetry breaking coefficients were added, in order to quantify the deviation of experimental data from this simplified model. Total and differential η photoproduction cross-section data were fitted, along with

beam and target asymmetries for photon beam energies up to $E_\gamma = 1.2 \text{ GeV}$ with a χ^2/N_{DoF} of 2.37. Resonances included in the fit were $P_{11}(1440)$, $D_{13}(1520)$, $S_{11}(1535)$, $S_{11}(1650)$, $D_{15}(1675)$, $F_{15}(1680)$, $D_{13}(1700)$, $P_{11}(1710)$, $P_{13}(1720)$, $P_{13}(1900)$ and $F_{15}(2000)$. Born terms were also included, but ρ and ω vector meson exchange in the t -channel was omitted to avoid double counting. The previously predicted significant contributions of the $S_{11}(1535)$ and $D_{13}(1520)$ were confirmed using cross-section data. The beam asymmetry revealed smaller contributions from the $P_{13}(1900)$ and $F_{15}(2000)$, while the target asymmetry indicated the influence of the $P_{13}(1720)$ and $F_{15}(1680)$. Other contributions were found to be small. Values for total width Γ_{tot} , electromagnetic helicity amplitude $A_{\frac{1}{2}}^p$ and electrostrong coupling, ξ , were extracted for the $S_{11}(1535)$. Resonance properties are defined in section A.2.

Further investigation [21] saw the addition to the model of configuration mixing angles, θ_S and θ_D , respectively for the two established S_{11} states — $S_{11}(1535)$ with spin $s = \frac{1}{2}$ and $S_{11}(1650)$ with $s = \frac{3}{2}$ — and for the aforementioned D_{13} states, plus the inclusion of a third S_{11} in the second resonance region to improve the fit, giving $\chi^2/N_{DoF} = 1.6$. Resonances up to $F_{15}(2000)$, as listed above, were individually included in the fit, with those up to $G_{17}(2190)$ treated as degenerate. Interdependent partial $N\eta$ widths and photo-excitation helicity amplitudes were obtained for eight resonances. The $F_{15}(1680)$ was calculated to have a stronger influence on η photoproduction than previously predicted. θ_S was found to be $-32.2^\circ \pm 1.8^\circ$ for the model excluding the third S_{11} — in good agreement with an earlier quark model prediction [34] and calculation based on spin-spin hyperfine interactions [35] — and $-26.6^\circ \pm 0.8^\circ$ including this state. For such a θ_S the $S_{11}(1535)$ should couple strongly to $N\eta$ while the $S_{11}(1650)$ decouples from these decays, explaining the observed selectivity of the $N\eta$ decay. The new S_{11} with mass 1729 MeV and width 183 MeV hugely improved the fit to total cross-section data, in spite of this information not being included in the fit. The constituent quark model cannot accommodate this resonance, supporting the argument against the $S_{11}(1535)$ being a standard three-quark state, as detailed in section 1.3.4.

New data up to $E_\gamma \approx 2 \text{ GeV}$ [22], fitted using all known 3 and 4 star resonances, reconfirmed the need for a third S_{11} , but predicted quite different properties

of $W = 1780$ MeV and $\Gamma = 280$ MeV. Extension to fit data up to $E_\gamma = 3$ GeV — including 1588 differential cross-section points — used all PDG 1 to 4 star resonances and t -channel contributions [23], showing that 9 of the 27 resonances investigated significantly influenced the reaction, including the third S_{11} , this time with $W = 1730$ MeV and $\Gamma = 100$ MeV.

A separate study by Glozman *et al.* [10] explained the anomalously high branching ratio of $S_{11}(1535) \rightarrow N\eta$ relative to that of the $S_{11}(1650)$ by modelling the baryon states in a quark-diquark configuration. Here gluons make no contribution to nucleon structure and decay properties are governed by selection rules arising from the quark-diquark clustering. A unified model of light and strange baryons and excitations thereof was also produced by Glozman and collaborators [24] which achieved the correct ordering of positive and negative parity states.

1.3.2 Effective Lagrangian Approaches

Effective Lagrangian approaches (ELAs) model the tree-level structure of the η photoproduction amplitude [25]. Tree diagrams include only acyclic connected Feynman diagrams wherein the momentum of each internal line can be determined by that of the external lines and conservation of momentum. Such Feynman diagrams of the contributing processes taken into account are shown in figure 1.5: with (a) and (b) being the leading s - and u -channel Born terms; (c) the leading t -channel ρ and ω vector meson exchanges; (d) and (e) the s - and u -channel nucleon resonance excitations.

Each particle in the modelled reaction is regarded as an effective field having properties including mass, strong decay width and photocoupling amplitude [36]. Channel coupling and final state interactions are not included in this approach, greatly reducing the number of free parameters having to be calculated while still giving a good first order assessment of resonance parameters. Including background terms at the tree level violates unitarity (unitarity requires the sum of probabilities of all possible outcomes of any event to be one), but this is thought to have only a small effect [26], since η to nucleon coupling is weak and non-resonant background terms contribute little to the η photoproduction cross-section.

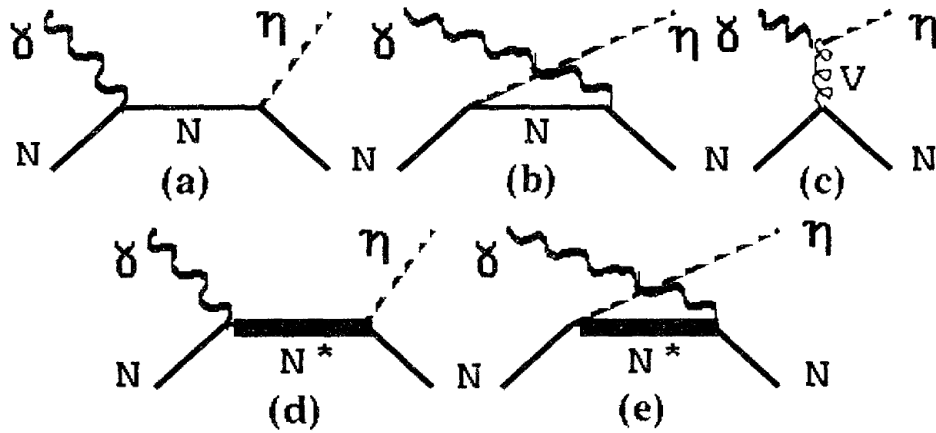


Figure 1.5: Tree-level contributions to η photoproduction [25]: (a) and (b) Born terms; (c) t -channel vector meson exchange; (d) and (e) s - and u -channel resonance excitations.

One such ELA was developed by Benmerrouche and Mukhopadhyay [25] to study η photoproduction near threshold. Vector and scalar meson exchange were investigated. In vector meson exchange, ρ and ω were found to be important, while ϕ was not. Coupling for the ηNN vertex was calculated to be $\frac{g_\eta^2}{4\pi} \sim 1.4$. Fits were made to the sparse experimental data then available for differential cross-section and recoil nucleon polarisation. The former showed that the $S_{11}(1535)$ dominated the process close to threshold, allowing extraction of the helicity amplitude $A_{\frac{1}{2}}^p = (95 \pm 11) \times 10^{-3} \text{ GeV}^{-\frac{1}{2}}$ for the baryonic transition $\gamma p \rightarrow S_{11}(1535)$.

Further data obtained using TAPS at MAMI [4] were fitted with a Breit-Wigner (BW) approximation, giving the first evidence for the contribution of the $D_{13}(1520)$ resonance to the η photoproduction cross-section. Further work by Mukhopadhyay *et al.* [26] using their ELA and the BW approach confirmed that a $D_{13}(1520)$ contribution was indicated, but deemed the previous analysis to be over-simplified, asserting that a quantitative measurement required unavailable polarisation data. This publication also concluded that $A_{\frac{1}{2}}^p$ was model dependent and introduced a new model-independent parameter, $\xi = (2.20 \pm 0.15) \times 10^{-4} \text{ MeV}^{-1}$, characteristic of the electrostrong property of the $S_{11}(1535)$.

1.3.3 Isobar and Reggeized Models

Isobar analyses break photoproduction amplitudes down into resonant and background contributions [13]. The latter comprise Born terms, in addition to ρ and ω exchange [37]. Resonance contributions are assessed through electric and magnetic multipole amplitudes (see section A.4), gleaned from angular distributions and polarisation observables. The interference (mixing) of resonances with one another and with background processes is not taken into account in some isobar models, rendering these inaccurate, and background terms are often over-simplified. Furthermore, the high number of fitting parameters in isobar analyses is disadvantageous. However, the recent adoption of ELA (see section 1.3.2) parameterisations of non-resonant — and in some cases also resonant — terms, has improved treatment of the background.

Nonetheless, isobar analysis modelling of background terms fails at high energy — above $E_\gamma \simeq 2 \text{ GeV}$ for η photoproduction. In this regime, Regge models have proven more successful. These are an efficient means by which to include the exchange of high-spin particles in the t - or u -channel, which becomes more pertinent here [29]. Particles sharing the same internal quantum numbers, but having different spins are grouped together in “Regge trajectories” [36]. These, shown in figure 1.6 for the ρ and ω mesons, are of the form:

$$\alpha(t) = \alpha_0 + \alpha' t \tag{1.4}$$

where t is the Mandelstam variable equal to M^2 , the square of the momentum transfer, as described in section A.3. Numerical values of the coefficients α_0 and α' were taken from [38]. Photoproduction at high energy, where distinguishing between individual resonances ceases to be possible, is described by the exchange of entire Regge trajectories as opposed to individual particles.

The η -MAID isobar model [28] was designed to fit η photo- and electroproduction (see section A.5) data. It included contributions from the N^* resonances $D_{13}(1520)$, $S_{11}(1535)$, $S_{11}(1650)$, $D_{15}(1675)$, $F_{15}(1680)$, $D_{33}(1700)$, $P_{11}(1710)$ and $P_{13}(1720)$, wherein the relevant electric and magnetic multipoles were assigned Breit-Wigner energy dependence. To describe the cross-section data, both S_{11} resonances at 1535 and 1650 MeV were needed. However, no evidence was found for a third S_{11} state

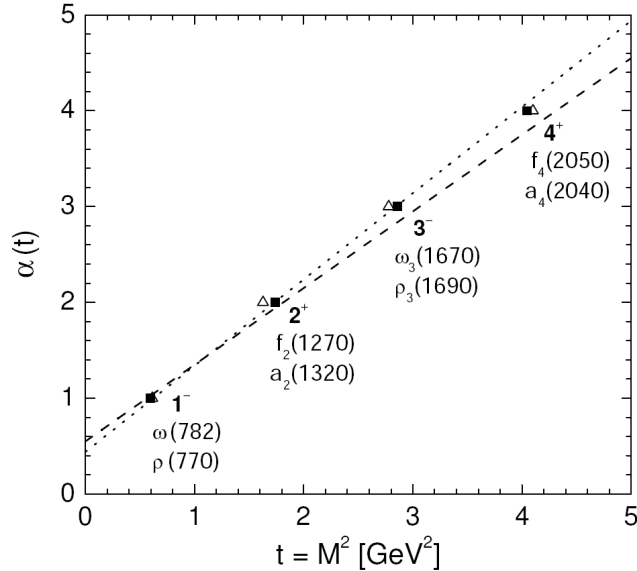


Figure 1.6: Regge trajectories of ω and ρ mesons, represented by dashed and dotted lines respectively. Mesons on the ω trajectories are shown by squares, ρ trajectory mesons by triangles [29].

at $W \simeq 1720$ MeV. Polarisation observables — which are vital for disentangling relatively weakly contributing excitations in close proximity to more dominant resonances — gave access to smaller contributions from resonances at higher L [27]. Calculation was also made of the non-resonant background due to vector meson (ρ and ω) exchanges in the t -channel and to Born terms. This was obtained by evaluating the Feynman diagrams derived from effective Lagrangians. Coupling of η mesons to nucleons is extremely small in η production, with the η -MAID fit giving an ηNN coupling constant of $\frac{g_{\eta NN}^2}{4\pi} = 0.10$. Hence Born terms have very little effect and vector meson amplitudes, especially ρ^0 exchange, dominate the background. For incident photon energies $\lesssim 2$ GeV, η -MAID described experimental data well, with χ^2/N_{DoF} of 2.0. For data taken at $E_\gamma = 4$ and 6 GeV, η -MAID was no longer valid.

An updated version of the η -MAID model used Reggeized vector meson exchanges [29, 30] instead of the standard ρ and ω exchanges used in η -MAID. The contributory resonances and their forms remained the same. For η photoproduction, only the $D_{13}(1520)$, $S_{11}(1535)$ and $S_{11}(1650)$ were definitively identified, with contributions from higher W resonances sufficiently entangled to render individual

distinction difficult or impossible. Born terms were not included in the new model since insufficient high energy data was available at backward angles to allow the necessary treatment of Reggeized nucleon exchange in the u -channel. At low energies the effect of Born terms was taken as negligible. For energies $E_\gamma \lesssim 2 \text{ GeV}$, Reggeized MAID described experimental data well, with χ^2/N_{DoF} of 3.9. Although η -MAID was better in this energy regime, for data taken at 4 and 6 GeV η -MAID was no longer valid whereas the Reggeized model held, with only small discrepancies due to the aforementioned omitted u -channel.

A further isobar model was used by Anisovich, Sarantev *et al.* [3] to perform a coupled-channel analysis of $\gamma p \rightarrow \pi N$, ηN data with $K\Lambda$ and $K\Sigma$ data. Coupled-channel analyses include multi-step sequences, *ie.* effects of intermediate states and final state interactions are taken into account. The Anisovich fit included 14 N^* resonances coupling to $N\eta$, with the non-resonant background comprising Reggeized t -channel π , $\rho(\omega)$, K and K^* exchanges and baryon exchanges in the s - and u -channels. For η photoproduction, the differential cross-section was dominated by the $S_{11}(1535)$ from threshold up to 1650 MeV. The next largest contributions came from the $P_{13}(1720)$ below 2 GeV then the $D_{13}(2070)$ along with $\rho(\omega)$ exchanges above 2 GeV. The total cross-section peaked strongly in the threshold region due to the $S_{11}(1535)$, with indication of one further resonance below 1800 MeV. Evidence was found for possible new resonances, most significantly for a $D_{15}(2070)$ with $J^P = \frac{5}{2}^-$. No evidence was found for a third S_{11} in either this model or an extension to include further K , Σ and Λ data [31]. The ratio of helicity amplitudes $A_{\frac{1}{2}}^p/A_{\frac{3}{2}}^p$ was also gleaned from photon beam asymmetry measurements.

1.3.4 Chiral Effective Lagrangians

Chiral effective Lagrangian models have been developed using the symmetries of the QCD Lagrangian and those of parity and charge conjugation. In these models, no three-quark resonances are explicitly included.

The S -wave meson-baryon interaction around the $N\eta$ threshold was investigated by Kaiser *et al.* [11] using the $SU(3)$ chiral effective Lagrangian at next-to-leading order — *ie.* evaluating Feynman diagrams involving two loops [39] — which is a

low-energy effective field theory respecting QCD symmetries. This approach models the $S_{11}(1535)$ as a quasi-bound $K\Sigma$ state and reproduces several experimentally measured properties, including a mass of 1557 MeV, a total decay width of 179 MeV and an $N\eta$ decay branching ratio of 31 %. Furtherance of this work [32] extended the model to a coupled-channel approach simultaneously describing 16 strong and electromagnetic meson-baryon interactions, using only 9 free parameters. This supported the argument for the S_{11} not being a qqq resonance, but a $K\Sigma$ “molecule”.

The $K\Sigma$ bound state was again examined by Li *et al.* [33] using electro- and photoproduction data. It was concluded that the Q^2 dependence of the helicity amplitude $A_{\frac{1}{2}}^p$ implied that such a state must mix strongly with three-quark states, requiring a third S_{11} in the second resonance region with mass ~ 1710 MeV.

1.3.5 Summary

The various models reviewed agree that, in the threshold region, the main mechanism by which η mesons are photoproduced on the proton is via excitation and subsequent decay of the $S_{11}(1535)$ resonance. There is also general consensus that the $D_{13}(1520)$ and $S_{11}(1650)$ have the next greatest influence on the process. However, the relative contributions of higher mass resonances, being much smaller, are harder to assess and therefore accordingly factious. For example, below 2 GeV the $P_{13}(1720)$ is crucial to reference [3], but merits no such distinction in any other model. The $D_{15}(1675)$ and $F_{15}(1680)$ were found in the η -MAID isobar model [27, 28] to have significant $N\eta$ branching ratios, whereas the later Reggeized model replaced the contribution of the latter by t -channel meson exchange [29].

In addition to the established resonances listed in table 1.2, new excited states have been postulated to improve model fits to empirical data, including a $D_{15}(2070)$ [3]. A third S_{11} resonance is a controversial possibility. The quark models reviewed herein predict such a state [23], isobar and Regge models [31] do not, while the chiral effective Lagrangian models [32, 33] disagree on the matter.

The non-resonant background is deemed to be small in the η production threshold region. At high energy, the contribution of Born terms remains limited due to the small η -nucleon coupling while ρ and ω exchange in the t -channel becomes

significant.

Although the $S_{11}(1535)$ dominance at threshold is undisputed, explanation of the anomalously large $N\eta$ coupling relative to that of the $S_{11}(1650)$ is far more contentious, bringing into dispute the very nature of the $S_{11}(1535)$. The quark models reviewed herein represent this as a standard 3-quark state [22] or as a quark-diquark pair [24]. The chiral effective Lagrangian model gives evidence for a quasi-bound $qq - qq\bar{q} K\Sigma$ state [32], with mixing between this and conventional N^* resonances [33].

Further data on η photoproduction on the proton will help to explain the anomalously strong $N\eta$ coupling of the $S_{11}(1535)$ and its dominance of the process. Tighter constraints can be put on competing theoretical and phenomenological models, improving these and facilitating differentiation between them. Ultimately, this should settle the argument over the composition of the $S_{11}(1535)$. As lesser contributions made by other resonances are also more firmly established, the results of the present work — combined with measurements of polarisation observables — will contribute to understanding of their properties and to that of the baryon excitation spectrum as a whole.

Chapter 2

Previous Work

2.1 SAID Database

The “Scattering Analysis Interactive Dial-in” (SAID) database [40] includes previous experimental measurements of η photoproduction differential cross-sections, covering the $(\theta_\eta^*, E_\gamma)$ range shown in figure 2.1.

The earliest three of these were made by C. Bacci *et al.* at the 1100 MeV Frascati electron synchrotron in 1963. Values for differential cross-sections were obtained using the $\eta \rightarrow 2\gamma$ channel for photon beam energies of $E_\gamma = 939$ and 978 MeV and η polar angles in the centre of mass frame, θ_η^* , of 103° and 106° ($\cos \theta_\eta^* = -0.22$ and -0.28), over a range of proton kinetic energies [41]. Further work in 1966 [42] measured the differential cross-section of η photoproduction using the 2γ channel with incident photon energies of $800 \leq E_\gamma \leq 1000$ MeV over the angular range $100^\circ \leq \theta_\eta^* \leq 120^\circ$ ($-0.17 \leq \cos \theta_\eta^* \leq -0.5$). This gave strong evidence of the S_{11} resonance hypothesised in 1965 [54]. 1968 saw measurements at $E_\gamma = 775, 800$ and 850 MeV in the range $0 \leq \cos \theta_\eta^* \leq 0.9$ for the lower energies, extending down to $\cos \theta_\eta^* = -0.8$ for 850 MeV [43]. The influence of partial waves above the dominant S_{11} was sought, but no evidence was then found for contributions from P_{11} , D_{11} or P_{13} partial waves. This conclusion was supported by results from the Orsay electron linear accelerator in 1969 [44]. Here, measurements were made at 6 photon energies between 725 and 875 MeV, across an angular range of $-0.93 \leq \cos \theta_\eta^* \leq 0.95$.

1971 saw measurements of the differential cross-section of η photoproduction

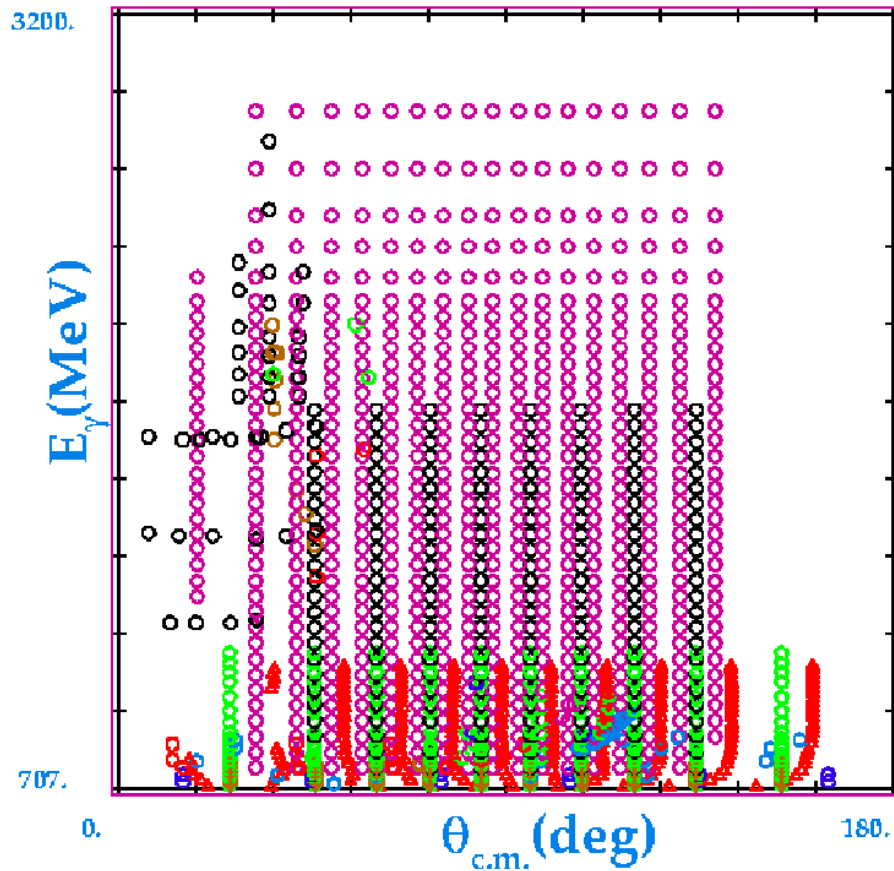


Figure 2.1: $(\theta_\eta^*, E_\gamma)$ range covered by measurements of η photoproduction differential cross-sections, as listed in the SAID database [40]. Markers represent: magenta pentagons [41], light blue circles [42], red circles [43], light blue hexagons [44], dark blue hexagons [45], black octagons [46], green circles [47], ochre diamonds [4], dark blue pentagons [48], black circles [49], red triangles [50], ochre circles [51], magenta circles [52], green pentagons [53]. The present work covers the range $0^\circ \leq \theta_\eta^* \leq 180^\circ$ for $707 \leq E_\gamma \leq 1403$ MeV

and of recoil proton polarisation, at 890 MeV [45]. The energy range was increased greatly to include $1.5 \leq E_\gamma \leq 2.2$ GeV in 1973 by an experiment carried out at the Bonn synchrotron [55]. In 1973, an experiment at the Daresbury Laboratory electron synchrotron [46] added data at $\theta_\eta^* = 28^\circ, 35^\circ$ and 42° ($\cos \theta_\eta^* = 0.88, 0.82$ and 0.74) over 8 E_γ steps in the range $1.97 \leq E_\gamma \leq 2.80$ GeV. This covered the region where the dominant contribution to the cross-section was considered to change from resonances to Reggeized ρ , ω and B -meson exchanges. The results were in keeping with this hypothesis. An indication of a G_{17} contribution at ~ 2.1 GeV was also found. Previously published results [56] were reanalysed, adding measurements to the database in the angular range $8^\circ \leq \theta_\eta^* \leq 46^\circ$ ($0.69 \leq \cos \theta_\eta^* \leq 0.99$) for photon energies of $1.24 \leq E_\gamma \leq 1.54$ GeV.

Investigations of η photoproduction continued in the 1980s. The cross-section asymmetry was measured using linearly polarised photons at 1.39, 1.53 and 1.8 GeV for $\theta_\eta^* = 28^\circ, 46^\circ, 57^\circ$ and 73° ($\cos \theta_\eta^* = 0.29, 0.54, 0.69$ and 0.88) at the 4.7 GeV electron beam of the Yerevan synchrotron in 1980 [57]. From these results, differential cross-sections were calculated for unpolarised photons, along with the energy dependence of the total cross-section, suggesting the contribution of more resonances with masses exceeding 1.6 GeV than previously predicted theoretically.

Prior to 1988, all contributions to the SAID database of η photoproduction differential cross-sections were obtained through analysis of the $\eta \rightarrow 2\gamma$ decay mode. In 1988, the 1.3 GeV electron synchrotron at the University of Tokyo's Institute for Nuclear Study was used for measurements in the energy range $808 \leq E_\gamma \leq 1008$ MeV at $\theta_\eta^* = 45^\circ, 80^\circ, 100^\circ$ and 110° ($\cos \theta_\eta^* = -0.34, -0.17, 0.17$ and 0.71) [47]. In this analysis, η mesons were reconstructed from the proton momentum, so all decay modes were included. These data were combined with previous results to determine photon-couplings of sub-1700 MeV mass resonances by partial wave analysis. This showed significant contributions from the $S_{11}(1535)$, $S_{11}(1650)$ and $P_{11}(1440)$, with a non-negligible contribution from the $D_{13}(1525)$.

Two additions to the SAID database were made in 1995. The Glasgow Photon Tagging Spectrometer and TAPS detector (see chapter 3 and section 4.5) at the 855 MeV MAMI microtron were used to measure differential and total cross-sections

at $707 \leq E_\gamma \leq 790$ MeV for $0^\circ \leq \theta_\eta^* \leq 180^\circ$ ($-1 \leq \cos \theta_\eta^* \leq 1$) [4]. The $\eta \rightarrow 2\gamma$ decay mode was used for the differential cross-section, with the addition of the $\eta \rightarrow 3\pi^0 \rightarrow 6\gamma$ mode in the total cross-section determination. Resonance parameters of the $S_{11}(1535)$ were extracted along with the electromagnetic coupling of $\gamma p \rightarrow S_{11}$. This analysis also identified a contribution from the $D_{13}(1520)$ resonance. The next 1995 publication came from the real photon line at the MIT-Bates Linear Accelerator [48]. Here, average incident photon energies of 729 and 753 MeV were used to assess differential and total cross-sections across the full 180° range in θ_η^* , utilising the 2γ decay mode. Isobar fitting analysis of these results showed only very small non- S_{11} features.

In 2002, the CLAS collaboration used the 2.49 GeV electron beam at the Thomas Jefferson National Laboratory (JLab) to measure η photoproduction in the energy range $0.75 \leq E_\gamma \leq 1.95$ GeV over the angular range $-0.8 \leq \cos \theta_\eta^* \leq 0.8$ [49]. η mesons were reconstructed from missing mass using recoil proton information. Extrapolation to the total cross-section was compared with the η -MAID isobar and chiral constituent quark models (see section 1.3), suggesting the existence of a third S_{11} resonance of mass ~ 1.8 GeV, coupling to the $N\eta$ channel.

The GRAAL facility at the European Synchrotron Radiation Facility (ESRF) hosted measurements at photon energies $707 \leq E_\gamma \leq 1100$ MeV over the full $\cos \theta_\eta^*$ range, in 2002 [50]. The two dominant neutral η decay modes ($\eta \rightarrow 2\gamma$ and $\eta \rightarrow 3\pi^0 \rightarrow 6\gamma$) were detected, with differential cross-sections assessed for both. Comparison was made to three theoretical models. Two of these implied that a third S_{11} resonance was needed, but η -MAID (see section 1.3.3) refuted this. Mass, width and photon coupling amplitude of the $S_{11}(1535)$ were evaluated. The width turned out to be very sensitive to contributions other than S_{11} , with values varying by a factor 2.25 depending on the model used.

2003 saw the publication of further η photoproduction data from MAMI [51]. Comparing unpolarised data to that taken using a polarised photon beam and frozen-spin butanol target, the first ever helicity-dependent differential cross-sections, $\frac{d\sigma}{d\omega}_{\frac{1}{2}}$ and $\frac{d\sigma}{d\omega}_{\frac{3}{2}}$, were measured at 783 and 798 MeV for $\theta_\eta^* = 70^\circ$ ($\cos \theta_\eta^* = 0.34$). The result agreed with the MAID (see section 1.3.3) prediction, indicating significant

contributions from the $S_{11}(1535)$ and $S_{11}(1650)$ resonances, but not providing a definitive indication of the $D_{13}(1520)$.

Further work at GRAAL was published in 2005 [52]. Differential and total cross-sections were published for the range $0.75 \leq E_\gamma \leq 3 \text{ GeV}$ over all polar angles. Both dominant η decay modes were detected, with the ratio of these determined. Partial wave analysis using 11 N^* resonances gave evidence for a new resonance, the $D_{15}(2070)$, and an indication of a possible $P_{13}(2200)$. The most prominent contributions were found to be from $S_{11}(1535)$, $P_{13}(1720)$ and $D_{15}(2070)$, with smaller contributions from $S_{11}(1650)$ and $P_{13}(2200)$.

The Laboratory of Nuclear Science (LNS) at Tohoku University contributed to the SAID database in 2006 [53]. The main focus of this experiment was the channel $\gamma p \rightarrow \pi^0 \eta N$, but measurements were also made of the differential and total cross-sections of $\gamma p \rightarrow \eta p$ with the 2γ decay mode. These were mostly in good agreement with previous results from JLab, GRAAL and Bonn, as well as with the η -MAID model (see section 1.3.3), though no indication was found of the suggested third S_{11} state.

Since then, two further significant publications have contributed to the world data set of η photoproduction differential cross-sections. Work by the CB-ELSA collaboration in 2007 [58] influenced the analysis of the present work (see chapter 5). The results of the GRAAL collaboration, published in 2008 [59], were compared to the those of this thesis (see section 6.1.2). These experiments are therefore described in detail in sections 2.2 and 2.3.

2.2 ELSA 2007

Data published in 2007 by the Crystal Barrel Collaboration at the Elektronen-Stretcher-Anlage (CB-ELSA) in Bonn, Germany [58], were gathered from 2000 to 2001. Differential cross-sections were measured using photons of energy 0.75 to 3 GeV over the full θ_η^* range.

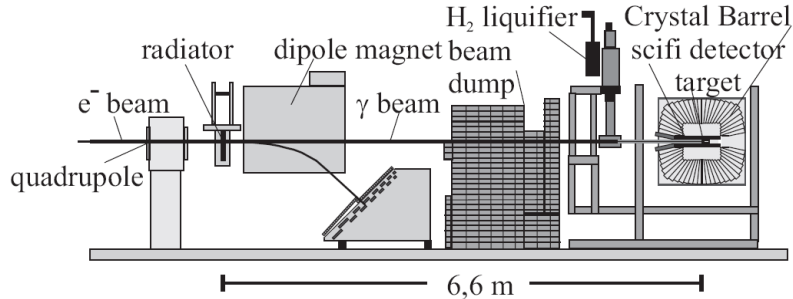


Figure 2.2: Experimental set-up at ELSA [58].

2.2.1 Experimental Set-up

The experimental set-up is shown in figure 2.2. Electron beam energies of 1.4, 2.6 and 3.2 GeV impinged on a radiator before entering the photon tagger. This gave photon energy resolution varying from 0.1 (0.5) MeV to 10 (30) MeV from high to low E_γ , for 1.4 (3.2) GeV beams respectively. For the principles of tagging, see section 3.1.

Liquid hydrogen provided the proton target. This was surrounded by a scintillating fibre detector (sci-fi), giving charged particle position information. Outside this was the Crystal Barrel, a calorimeter with high photon detection efficiency and granularity, covering the full ϕ range and $12^\circ \leq \theta \leq 168^\circ$, corresponding to 98 % of 4π .

2.2.2 Analysis

η photoproduction differential cross-sections were determined for the two main neutral decay channels (see section 1.1), for incident photon energies up to $E_\gamma = 3$ GeV, giving $\sim 150,000$ η events.

For the 2.6 GeV data, η mesons were selected by cutting around the 547 MeV peak in the 2γ and $3\pi^0$ invariant mass spectra, for the 2γ and 6γ decays respectively. Background was subtracted using the average of the bin contents on either side of the η -mass peak in these invariant mass spectra.

For the 1.4 and 3.2 GeV runs, proton missing momentum was reconstructed for 2 or 6 photon events in a kinematic fit. Further kinematic fitting was used in

conjunction with invariant mass cuts to select η events. Again, background was subtracted using side-bin counts. Correction was also made for background events using empty target data.

Detector acceptance was determined using simulations run in GEANT3. The experimental set-up was modelled, including Barrel, sci-fi and target geometry. Acceptance, as a function of $\cos\theta_\eta^*$ and E_γ , was defined as the ratio of generated to reconstructed Monte Carlo events. This was a maximum of $\sim 70\%$, falling to zero at forward and backward angles.

2.2.3 Results

Differential cross-sections were calculated using equation 5.1, as follows:

$$\frac{d\sigma}{d\Omega} = \frac{N_{\eta \rightarrow n\gamma\gamma}}{A_{\eta \rightarrow n\gamma\gamma} \cdot N_\gamma \rho_t \cdot \Delta\Omega \cdot \frac{\Gamma_{\eta \rightarrow n\gamma\gamma}}{\Gamma_{total}}}$$

with symbols defined in section 5.3. Differential cross-section results were published from 750 to 3000 MeV, with comparison to the SAID and MAID models.

The ratio of partial widths of the 2γ and 6γ η decays were also determined. Total cross-sections and a partial wave analysis were reported, indicating contributions to η photoproduction from three resonances: $S_{11}(1535)$, $P_{13}(1720)$ and $D_{15}(2070)$.

2.3 GRAAL 2007

The 2007 publication of the GRAAL collaboration reported on differential and total cross-sections and beam asymmetry, Σ , of η photoproduction for incident photons of energy $707 \leq E_\gamma \leq 1500$ MeV across the angular range $30^\circ \leq \theta_\eta^* \leq 160^\circ$ ($-0.94 \leq \cos \theta_\eta^* \leq 0.87$) [59].

2.3.1 Experimental Set-up

The ESRF storage ring provided 6.03 GeV electrons from which laser photons were Compton scattered, producing a tagged, linearly polarised γ -ray beam. Maximum photon energies of 1.1 and 1.5 GeV were obtained, respectively using the green line at 514 nm and a set of UV lines around 351 nm from an Ar laser.

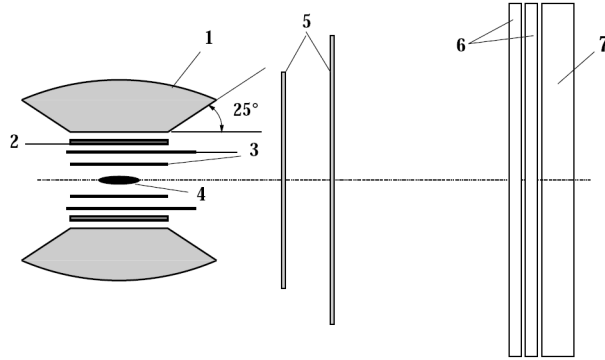


Figure 2.3: Experimental set-up at GRAAL [59].

The beam was tagged using a silicon microstrip detector and a plastic scintillator array. Beam polarisation varied from nearly 100 % at maximum E_γ down to ~ 60 % for the green line and ~ 30 % for the UV lines at 707 MeV, the η production threshold.

A liquid hydrogen target was used inside the LA γ RANGE detector, a 4π system with charged and neutral particle detection capabilities. Surrounding the target were cylindrical MWPCs (number 3 in figure 2.3), a plastic scintillator barrel (2), and a Bismuth-Germanium-Oxide (BGO) calorimeter (1). Forward angles were covered by two planar MWPCs (number 5 in figure 2.3), a double plastic scintillator hodoscope (6) and a lead-scintillator shower detector (7).

2.3.2 Analysis

Both dominant neutral η decays were analysed. Cuts were made on η energy, proton polar and azimuthal angles and proton time-of-flight, as well as on 2γ and 6γ invariant mass. A GEANT3-based Monte Carlo simulation of all apparatus was used with an event generator to optimise cuts, calculate acceptance and estimate background. Acceptance was found to be ~ 33 % for the 2γ decay and ~ 6 % for 6γ . Approximately 1 million ηp events were found. Differential cross-sections were calculated using equation 5.1 (see sections 2.2 and 5.3).

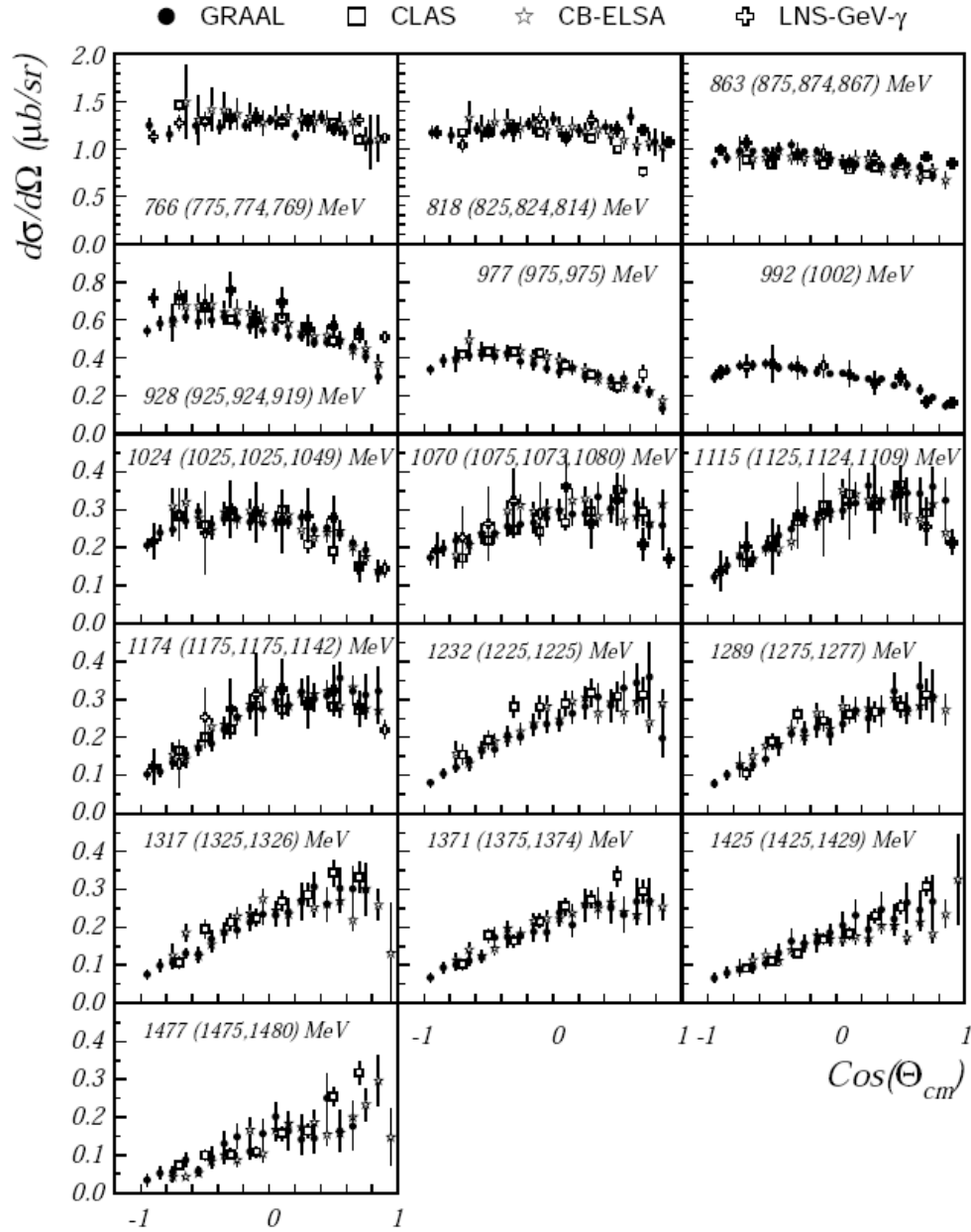


Figure 2.4: Comparison of differential cross-section measurements [59] from GRAAL (closed circles), CLAS (open squares), CB-ELSA (open stars) and LNS-GeV- γ (open crosses). Energy bins in parentheses are for CLAS, CB-ELSA and LNS respectively.

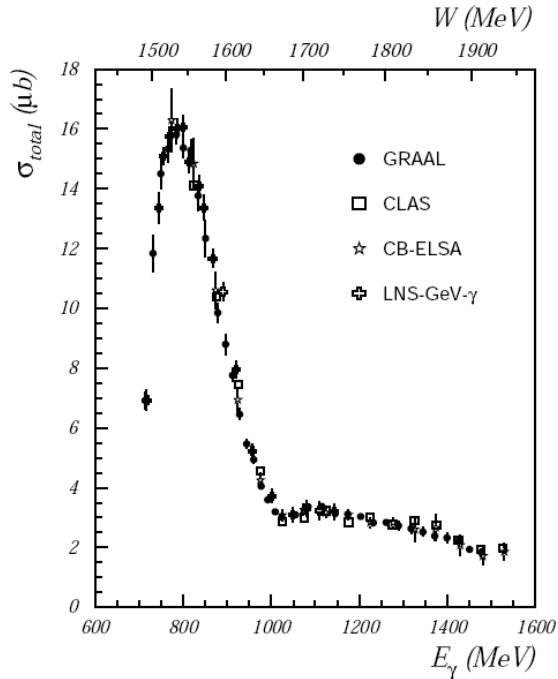


Figure 2.5: Comparison of total cross-section estimates [59] from GRAAL, CLAS, CB-ELSA and LNS-GeV- γ , with symbols as defined in figure 2.4.

2.3.3 Results

Differential cross-sections and beam asymmetries were measured for $30^\circ \leq \theta_\eta^* \leq 160^\circ$ and $707 \leq E_\gamma \leq 1500$ MeV. Good agreement was found between the 2γ and 6γ decay modes. The total cross-section was also extracted. These results were compared to previous GRAAL measurements [50] as well as to CLAS [49], CB-ELSA [52] and LNS-GeV- γ [53] results, as shown in figures 2.4 and 2.5, with good agreement found in most angle and energy bins.

Three models were also compared to the experimental data. Two of these were found to fit well, in spite of differences in resonance couplings. However, a third model required the introduction of a third S_{11} resonance, along with new resonances $D_{13}(1875)$ and $D_{15}(2070)$. A preliminary search for a narrow $N(1670)$ state — suggested in [60] — was made, but no evidence was found.

2.4 A2 2007

This thesis work was carried out at the Mainzer Microtron (MAMI) electron accelerator, within the A2 collaboration. The upgrade of the accelerator from a maximum electron energy of 885 MeV to 1.5 GeV, completed in 2006, necessitated the upgrade of the Glasgow-Mainz Photon Tagging Spectrometer. This comprised a large part of this thesis work and is described in chapter 3.

Measurement was made of η photoproduction on the proton in July 2007. This provided a complex test of the upgraded system while enlarging the world data set. The tagged photon beam, covering the energy range $614 \leq E_\gamma \leq 1403$ MeV, was incident on a liquid hydrogen target. This was surrounded by a cylindrical Particle Identification Detector, which differentiated between charged and neutral particles, and the spherical Crystal Ball $NaI(Tl)$ detector, which provided calorimetry and angular information for all reaction products. These covered 96% of 4π , with the forward angular region being covered by the BaF_2 detector, TAPS, which gave calorimetry, angle and particle charge. Thus the angular ranges $0^\circ \leq \theta_\gamma^{lab} \leq 160^\circ$ and $0^\circ \leq \theta_\eta^* \leq 180^\circ$ were covered, where θ_γ^{lab} is the polar production angle of a decay photon in the laboratory frame. The experimental set-up is described in chapter 4.

Differential cross-sections, $\frac{d\sigma}{d\Omega}$, of η photoproduction on the proton:

$$\gamma p \rightarrow \eta p$$

have been determined using the two principal neutral decays of the η -meson: $\eta \rightarrow 2\gamma$ and $\eta \rightarrow 3\pi^0 \rightarrow 6\gamma$. η decay photons were detected, with the proton reconstructed from missing momentum. Analysis and results are reported in chapters 5 and 6 respectively. These results have been compared to the most recent experiment carried out at GRAAL [59] and to the SAID fit [40], as shown in section 6.1.2.

Chapter 3

Bremsstrahlung and the Glasgow-Mainz Photon Tagging Spectrometer

3.1 Tagging

In the A2 hall, a variety of thin metal foils or crystals (“radiators”) can be used to produce Bremsstrahlung photons [61]. The electron beam from MAMI is incident on such a radiator, within which some of the electrons are decelerated in the Coulomb field of atomic nuclei (N), losing energy while radiating photons:

$$N + e^- \rightarrow N + e'^- + \gamma$$

The Glasgow-Mainz Photon-Tagging Spectrometer (the “tagger”) has the dual purpose of steering non-radiating electrons into the beam dump (“dumping” the beam) and momentum analysing the radiating electrons in a process known as “tagging”. The energy of the resulting photons can be deduced via the formula:

$$E_\gamma = E_0 - E_{e^-} \tag{3.1}$$

where E_γ is photon energy, E_0 is beam energy and E_{e^-} is degraded electron energy, measured by the tagger. The energy of the recoiling nucleus in the radiator is of the order of a few keV and therefore negligible.

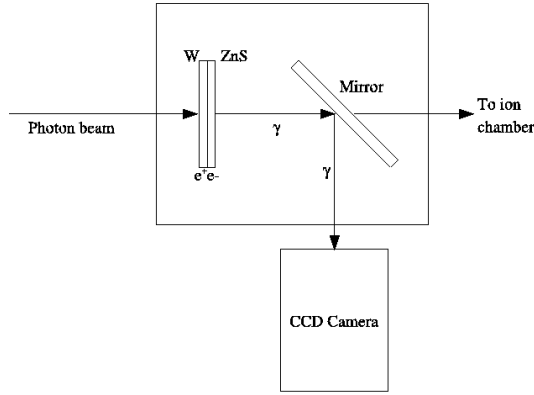


Figure 3.1: Schematic of the photon camera system (not to scale).

The Bremsstrahlung photon energy spectrum has an $\sim \frac{1}{E_\gamma}$ dependence [62]. Photon production is forward peaked, approximately within a cone half-angle of $\frac{m_{e^-}}{E_0}$ where m_{e^-} and E_0 are the electron mass and beam energy respectively.

3.2 Goniometer and Photon Television

Amorphous radiators, such as copper, produce unpolarised photons; an aligned crystal — diamond, for example — can produce linearly polarised photons over a certain energy range, by coherent processes; and Vacoflux, a magnetised alloy of 48% *Fe*, 48% *Co* and 2% *V*, allows Møller electron beam polarimetry. These are selectively moved in the beam line using a goniometer, which allows fine control of the radiator’s position and angle. It can move in the horizontal and vertical planes as well as rotating around axes perpendicular to these planes and to the beam axis. This allows precise diamond alignment, so that the energy of the coherent peak can be selected for polarised photon production. For this work, a 10 μm -thick amorphous copper radiator was used.

The photon beam passes from the radiator, through a series of collimators (detailed in section 3.6) to the Crystal Ball detector, within which it hits the target, described in chapter 4. The beam position is observed by a sensitive photon beam monitor, as depicted in figure 3.1. This comprises an ~ 1 mm-thick tungsten foil, to enhance e^+e^- pair production, in front of a zinc sulphide scintillator. Light from

this is incident on an angled mirror, reflecting down to a Photonic Science Darkstar 800 camera. This is a CCD camera, which is useful down to $1\ \mu\text{lux}$. The beam monitor is used to assess beam steering and shape.

3.3 Tagger History

The Glasgow tagger in Mainz was originally a quadrupole-dipole-dipole (QDD) set-up used with MAMI-A's 180 MeV beam [63]. A new QD tagger was developed for use with the 855 MeV electron beam of MAMI-B in 1990 [64, 65]. The quadrupole was later removed to make space for the current goniometer, leaving the tagger in its present geometry.

In 2005, the planned construction of the new 1.5 GeV MAMI-C, see section 4.2.2, necessitated a corresponding upgrade of the tagger [5], detailed herein. The tagger's main constituents are a dipole electromagnet and the focal plane detector (FPD) array. Dumping MAMI-B's 855 MeV beam required a field strength of 1.02 T, with the tagger dipole capable of reaching 1.4 T. However, to dump 1.5 GeV required an increase in the maximum field strength to ~ 1.8 T. In addition, the FPD array scintillators — which had become radiation damaged over time — were replaced, along with their read-out electronics.

In October 2006 the tagger upgrade was completed, enabling tagging of photons with energies of $80 \lesssim E_\gamma \lesssim 1400$ MeV, for an electron beam of 1.5 GeV. A maximum magnetic field strength in excess of 2 T was achieved in the dipole while the new scintillators and read-out electronics were installed, tested and used successfully for experiments [66].

3.4 Dipole

Downstream of the radiator, the electron beam enters the tagger dipole, shown pictorially and in schematic cross-section in figures 3.2 and 3.4 respectively. This is a normal-conducting electromagnet composed of low carbon steel, with a maximum field strength of ~ 2 T exceeding the 1.8 T needed to steer the 1.5 GeV non-radiating

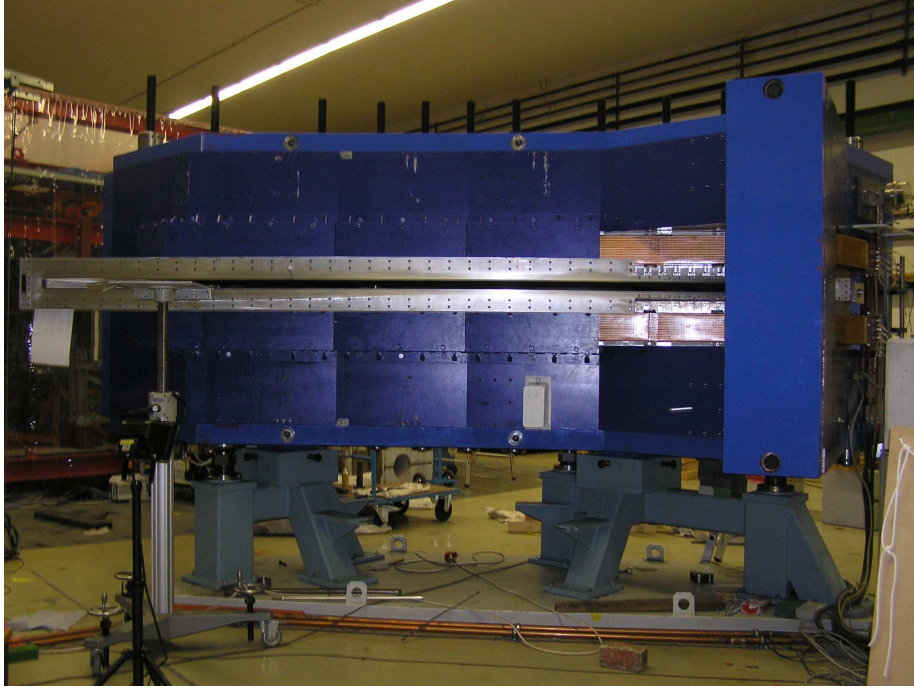


Figure 3.2: Upgraded tagger magnet.

electrons through 79° to the beam dump. Dipole field strength is measured by a Nuclear Magnetic Resonance (NMR) probe, located at the upstream end, as shown in figure 3.4. Electrons degraded in the radiator are momentum analysed by the same dipole magnet and focused onto the FPD array, described in section 3.5.

The beam dump is a shielded Faraday Cup which measures electron beam current. This is surrounded by shielding to absorb radiation, in the form of photons and neutrons, produced by interactions of the energetic electrons. This would otherwise interfere with the experiment, since the calorimeters (see chapter 4) are sensitive to such radiation. Radiation can also affect the read-out electronics of the detectors. The dump contains a scintillating CROMOX screen, viewed by an external CCD camera, for monitoring the electron beam position.

The original dipole was constructed from low carbon steel, with a pole gap of 50 mm and a maximum current of 440 A. Keeping the pre-existing power supply and cooling system for the magnet coils, halving the pole gap — in addition to adding 110 mm of iron to the return yoke to prevent saturation, as shown in figure 3.3 — was calculated to be sufficient to increase the field to 1.8 T [5]. The energy dependence of the half-cone distribution angle, $\theta_{e^-} = \frac{E_\gamma}{E_{e^-}} \frac{m_{e^-}}{E_0}$, of Bremsstrahlung

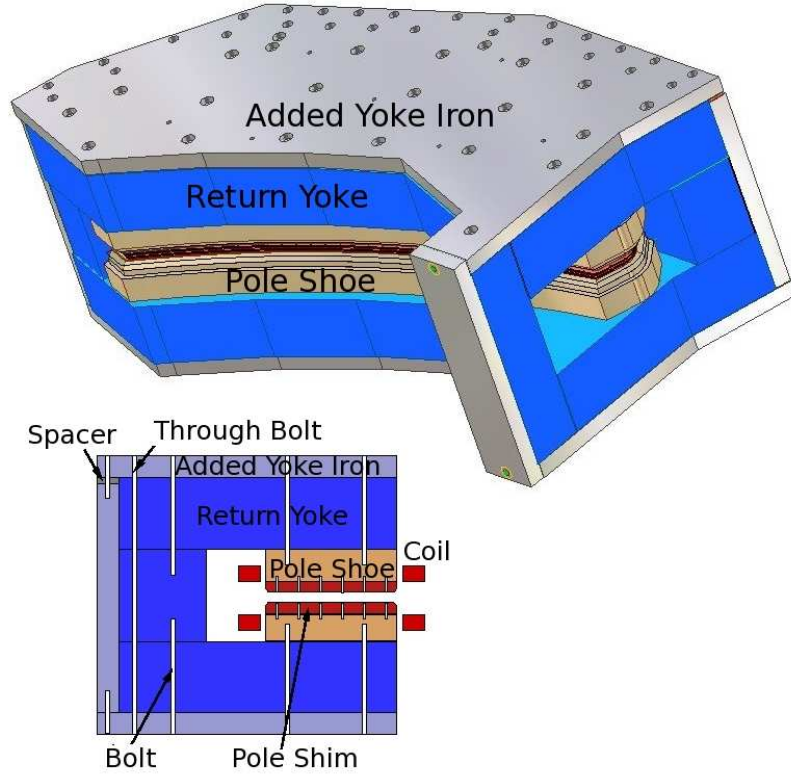


Figure 3.3: 3D model and cross-section of the upgraded tagger magnet [5].

electrons [62], allowed for this reduced gap without increasing the loss of electrons in collision with the pole faces. Accordingly, 12.5 mm-thick low carbon steel pole shims were affixed to the pole shoes using 129 M8 screws, as depicted in figure 3.4. The extra mechanical stresses added by the increased field were handled by replacing the main load carrying bolts with through-rods. The vacuum box was modified to accommodate the two new NMR probes needed to cover the extended field range.

Construction of the upgraded magnet was completed prior to this thesis work commencing. The following tests and modifications were a part of the present work.

3.4.1 Vacuum Window

The dipole vacuum was sealed by affixing a Kapton window using two-part epoxy. This plastic is strong enough to withstand the pressure from outside of the vacuum, with a small enough density and thickness to minimise disruption to electron trajectories.

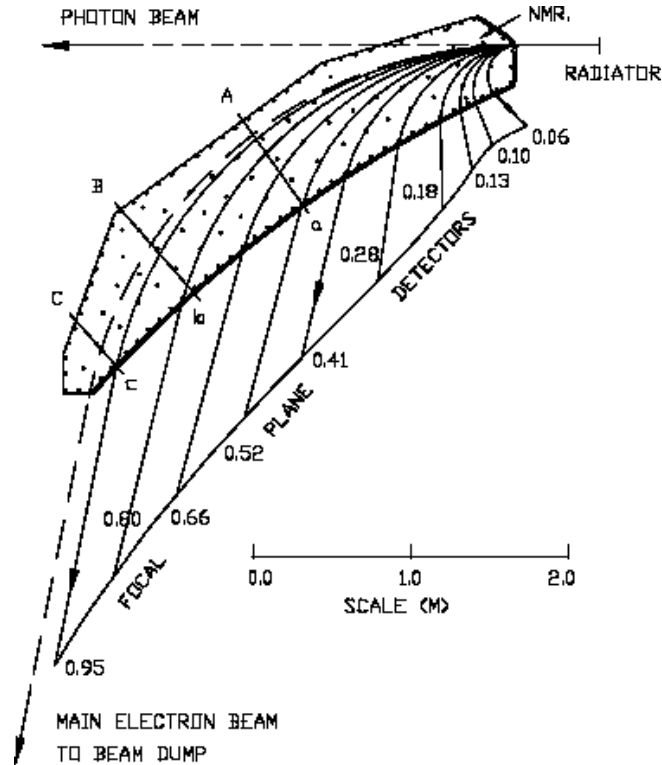


Figure 3.4: Schematic of the lower pole and FPD array. Dots represent the M8 screws, solid lines the tagging electron trajectories, long-dashed line the main electron beam and short-dashed line the photon beam. Electron and photon energies are indicated as fractions of the main beam energy.

3.4.2 Field Inhomogeneities

The new pole shims contained holes for positional adjustment pins and M8 fixing screws. These were countersunk and of a different material from the shims, causing potential inhomogeneities in the magnetic field. Measurements were made to test for this. A Hall probe was used to measure the field every few centimetres along three lines: Aa , Bb and Cc , shown in figure 3.4, for different magnet currents. The results along line Bb , at 435 A, can be seen in figure 3.5. The solid line shows the field modelled using the finite element code TOSCA [67]. The small dips at ~ 25 and 40 cm correspond to the locations of two M8 fixing screws. The field reduction was found to be a maximum of $\sim 3.0\%$, with a full width at half maximum (FWHM) of ~ 17.5 mm. The effect on the tagger's energy resolution is thought to be small, but there can be an effect on the energy calibration, as described in section 3.7.

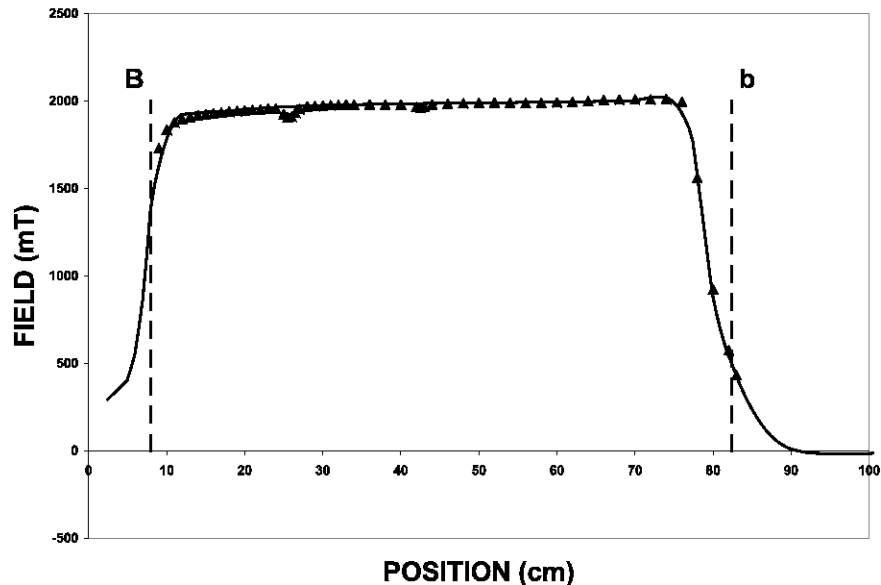


Figure 3.5: Measurement (triangles) and TOSCA prediction (solid line) of the tagger field along line Bb (see figure 3.4), with a dipole current of 435 A.

The field was found to exceed the necessary 1.8 T comfortably and, aside from these inhomogeneities, to be in good agreement with the TOSCA prediction both at the electrons' exit edge and in the central region of the dipole, as shown in figure 3.5.

3.4.3 Nuclear Magnetic Resonance Probe

In order to cover the extended field range of the upgraded magnet, the pre-upgrade NMR system was replaced by a dual probe Caylar Drusch Products Nuclear Magnetic Resonance (NMR) 20 Gaussmeter [68]. The new probes were set up and tested before their position was optimised. A maximum field of 2.004 T was recorded, showing that the magnet upgrade was successful and the probe fit for purpose.

3.4.4 Field Settling Time

The settling time of the magnetic field after changes in current was determined. Readings were taken at various magnet currents, over different time periods. Hysteresis effects were minimised by increasing the current to maximum then reducing

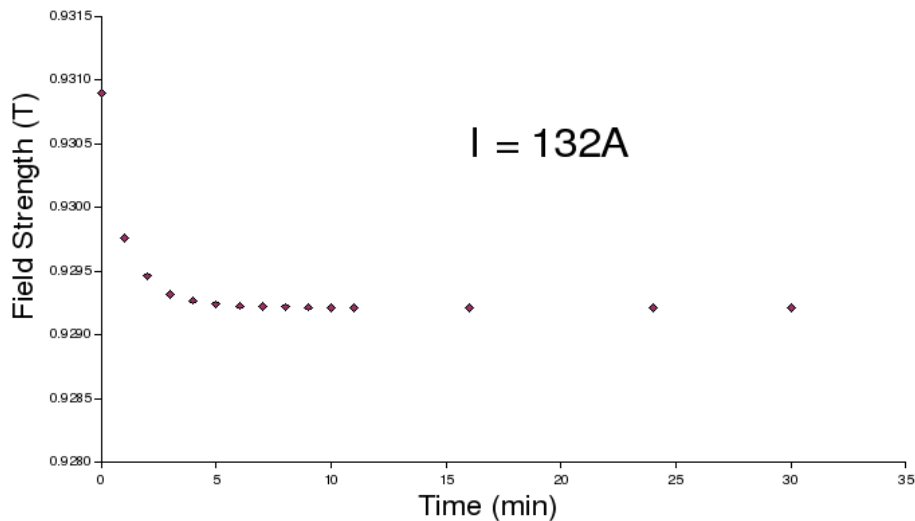


Figure 3.6: Settling time of the tagger dipole field, with a dipole current of 132 A.

to the desired value for each current. The field was found to vary most within the first 5 minutes after a change in the current. At 132 A, the field was steady to four decimal places after 6 minutes, as shown in figure 3.6.

3.4.5 Stray Magnetic Field

Tests were made to assess the stray magnetic field beyond the edge of the dipole. If stronger than 100 mT, this would affect the gain of the photomultiplier tubes (PMTs) — see section 3.5.

Using a Hall probe, such a field was found near the radiator end of the FPD. A more thorough test was then carried out using a scintillator connected to a PMT and an oscilloscope, with a beta-emitting source. The scintillator was placed in the fringe field, first unshielded then with different thicknesses of mild steel screening. It was found that 0.7 mm mild steel provided sufficient screening for the PMT signal to be unaffected by the stray field.

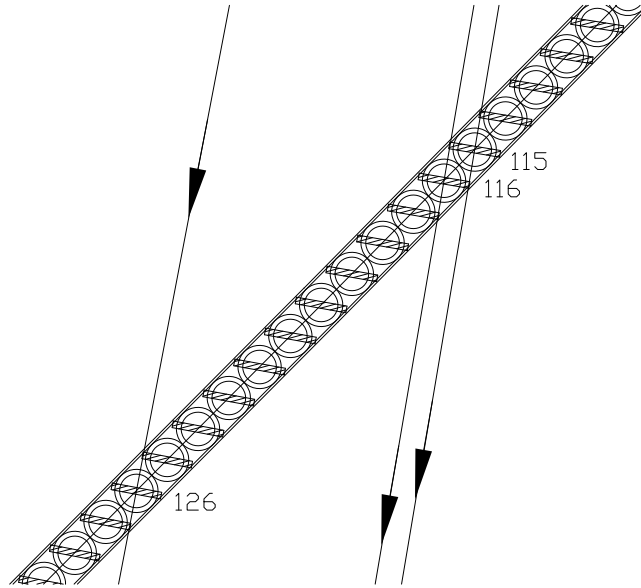


Figure 3.7: Schematic of a focal plain detector section from above [69]. Scintillators: shaded rectangles, PMTs: inner circles, μ -metal shields: outer circles, mild steel screening: long rectangles, selected electron trajectories: arrows. Sample channels are numbered.

3.5 Focal Plane Detector and Tagger Electronics

The focal plane detector is an array of 353 EJ200 plastic scintillators, oriented at $\sim 90^\circ$ to the trajectories of electrons exiting the dipole, depicted in figure 3.7. The scintillators are of length 80 mm and thickness 2 mm, with widths varying from 9 to 32 mm to keep the energy coverage of each element approximately constant. Scintillator centres are 13 mm apart. Adjacent scintillators overlap such that any electron from the radiator should pass through two neighbouring scintillators. Such an overlapping section is known as a channel. These are numbered 1 to 352, from low to high electron momentum along the FPD. An event must be in a channel — *ie.* in coincidence between two neighbouring scintillators — to be recorded, reducing background. Each scintillator is attached to an acrylic light guide, using ultra-violet curable epoxy. The scintillators and light guides are covered in double-sided aluminised mylar wrapping for light-proofing, see figure 3.8. The light guide connects to an Hamamatsu R1635 PMT. This is enclosed in a μ -metal tube with additional 0.7 mm-thick mild steel plates around the PMTs to provide screening



Figure 3.8: Various widths of scintillator through the stages of wrapping: unwrapped (far left), in mylar (second from left), in black tape and below a μ -metal tube (second from right) and with μ -metal tube attached (far right).

from stray magnetic field from the dipole, as described in section 3.4.5.

The NE 111 scintillators of the original 885 MeV tagger had suffered radiation damage over their 15 years' service, resulting in low light output, giving small signals in spite of increasing PMT voltages. Hence it was decided to replace these during the upgrade. EJ200 was chosen as the new material since, in spite of being slightly slower than NE 111, it is less susceptible to radiation damage and its scintillation spectrum is closer to the PMTs' optimum response range.

The original PMTs were re-used, since tests showed that the majority of these still functioned well [70]. They were sorted by gain and fitted in ascending order from the low to high electron-momentum ends of the FPD in order to compensate partially for the lesser efficiency of light collection of the broader scintillators at the low-momentum end.

Each PMT is linked to a custom made amplifier / discriminator (A/D) card, the circuit diagram for which is shown in figure 3.9. The PMTs are powered by high voltage (HV) supplies with variable output capability of 900 to 1500 V. Typically $HV \simeq 1100$ V is used, drawing a current of ~ 0.3 mA. The A/D cards run on low

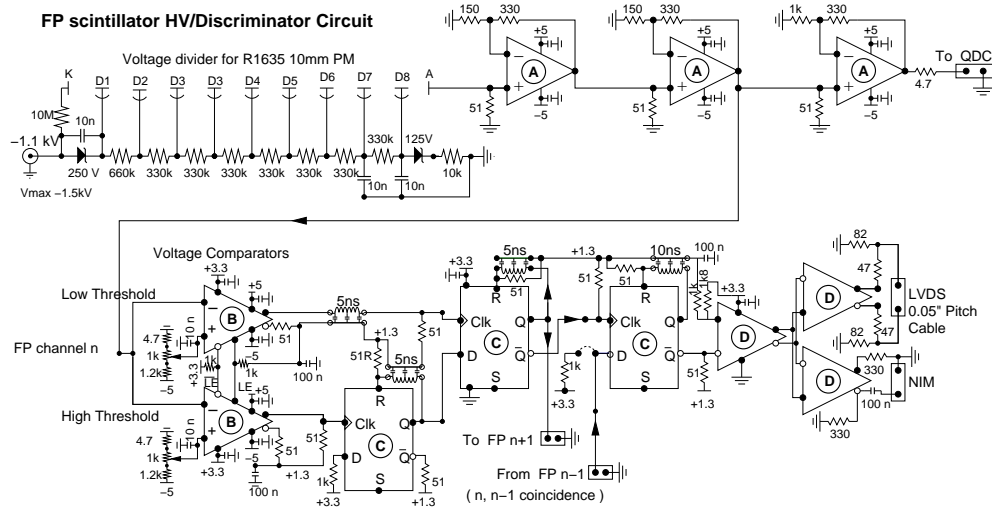


Figure 3.9: Circuit diagram of the amplifier-discriminator cards [5]. Labels show integrated circuits: AD-8009 1 GHz current-feedback op-amps (A), MAX-9601 dual ultrafast comparator (B), MC100LEVL30 triple D-type flip flop with S/R (C) and MC100LVEL11 buffer, fan out (D).

voltage, $LV = \pm 5V$, drawing currents of $\sim 250\text{ mA}$ and $\sim 370\text{ mA}$ each from the negative and positive lines respectively. Fans, powered by $+12V$ D.C. cool the A/D cards.

Anode signals from the PMTs pass through a $\times 10$ amplifier which feeds into a dual adjustable-threshold discriminator. The low threshold records all pulses with almost no walk — *ie.* almost instantaneously — including some degree of noise. The higher threshold records only the useful pulses but with some walk. From here, an AND gate records signals with good time resolution from the low threshold and noise suppression from the high threshold. This supplies a logic low-voltage differential signal (LVDS) to an active fanout card. This feeds sampling multi-hit time-to-digital converters (TDCs) and scalars. The scalars were operated using Compass Accumulation, Transfer and Control Hardware (CATCH) modules until June 2007 when, due to technical issues, these were replaced with FASTBUS Struck-200 units.

The op-amps are also connected to a LeCroy 1885F FASTBUS charge-to-digital converter (QDC), used for detector diagnostic testing and monitoring HV adjustment. Nuclear Instrumentation Module (NIM) discriminator output is available for diagnostics. Logic signals were also sent from each A/D card to its next highest

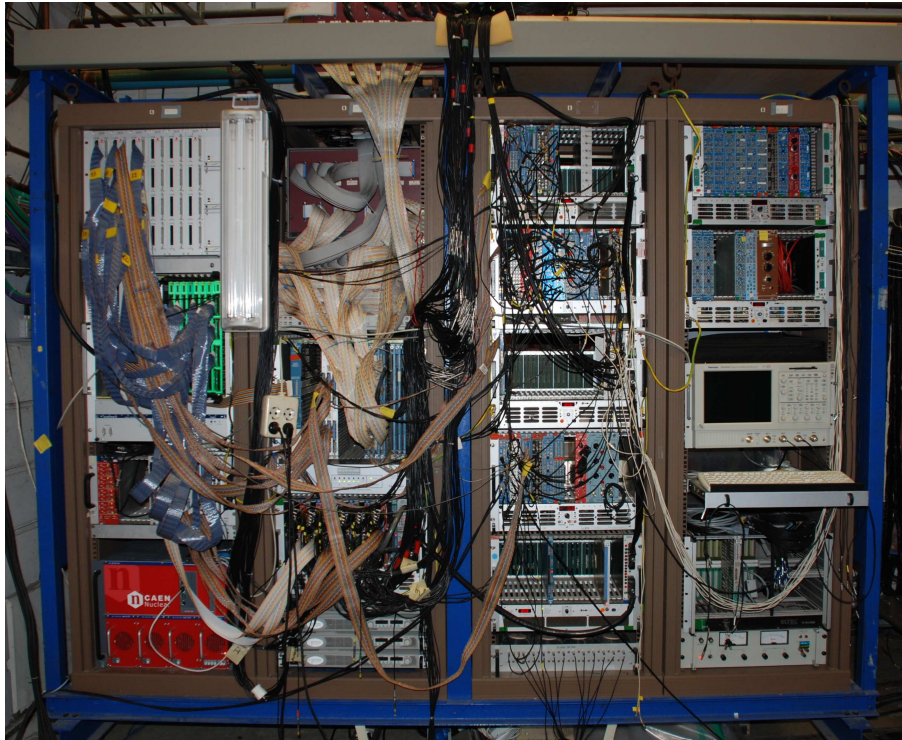


Figure 3.10: Tagger electronics rack.

energy neighbour to measure hits coincident between the two, *ie.* to define the aforesaid channels.

The CATCH TDCs are continuous sampling, multi-hit units with no start / stop. These have an ~ 10 GHz oscillator which acts as a free-running clock, giving a time conversion of 117 ps per channel. Double hit resolution is ~ 20 ns. Each TDC records a hit in terms of an oscillation count. A reference TDC is connected to the CB/TAPS trigger (see section 4.6.4) so that the timing of a TDC event is deduced from the difference between its oscillation count and that of the reference TDC, multiplied by the time conversion factor.

The tagger QDCs, Scalers and TDCs connect to a VERSAmodule Eurocard bus (VMEbus) interface which both controls and reads out signals from these components [71]. The electronics rack is shown in figures 3.10 and 3.11.

Thus the TDCs record the incident channel number of each electron on the FPD array and its time of incidence. Within the fixed magnetic field of the dipole, radius of electron trajectory is proportional to electron energy, so that lower energy electrons fire scintillators at the upstream end of the FPD array and vice versa. The

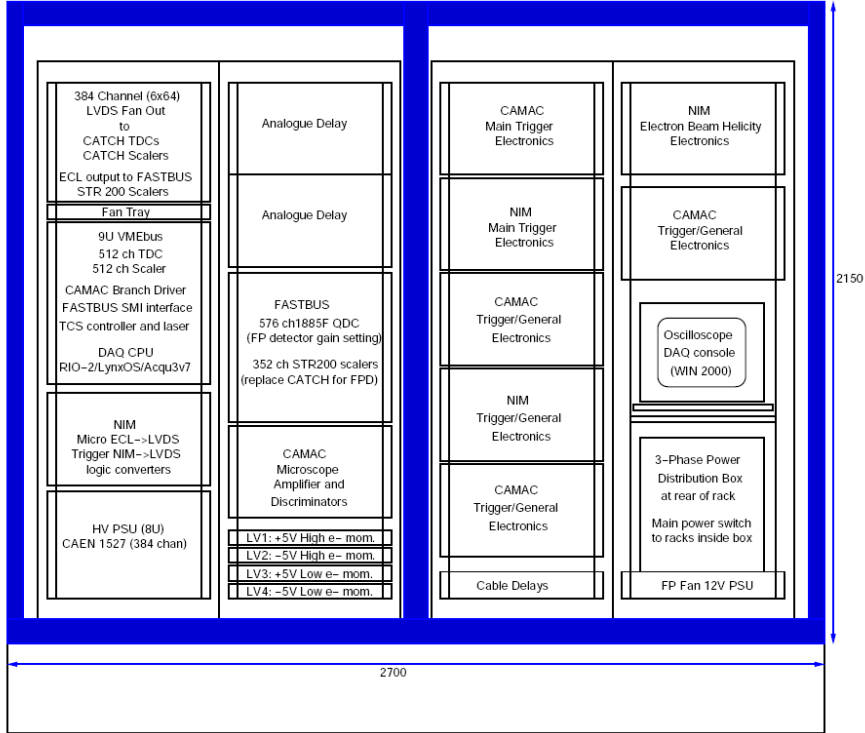


Figure 3.11: Schematic of the tagger electronics rack [71].

tagger energy calibration is described in section 3.7.

Electrons with energies ~ 4.6 to 93% of E_0 can be tagged, corresponding to $105 \leq E_{e^-} \leq 1435$ MeV from the 1508 MeV electron beam, with energy resolution, determined by the channel widths, of ~ 4 MeV. This gives tagged photons in the range $73 \leq E_\gamma \leq 1403$ MeV. A maximum tagged photon flux of $\sim 2.5 \times 10^5$ (MeV·s) $^{-1}$ can be measured [5]. This is limited by the width of pulses in the PCBs and dead time in the electronics. Tagging the full photon energy range would give a maximum variation in rate along the FPD of $\sim \frac{1400}{80}$, almost a factor of 20. In the present work, the high electron energy end of the tagger with the highest count rate was switched off to avoid burning out the PMTs there. Hence the E_γ range 614 to 1403 MeV was tagged. The tagger has a single-counter time resolution varying from 0.37 to 0.53 ns FWHM across the range of scintillator widths [5].

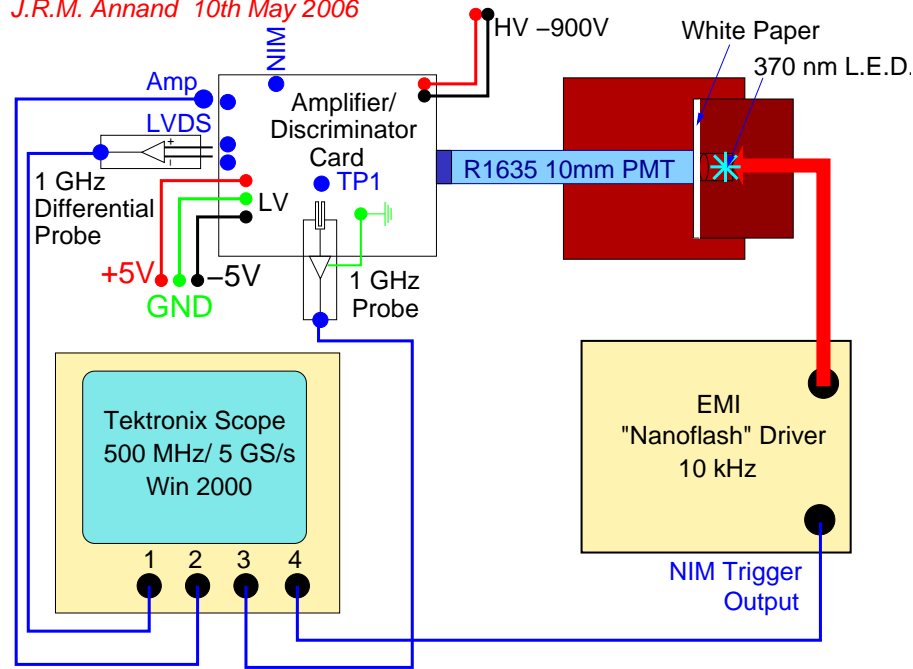
Test setup for Tagger Amp/Discr cards*J.R.M. Annand 10th May 2006*

Figure 3.12: Schematic of the A/D card test setup [72].

3.5.1 Scintillator Tests

A selection of the new scintillators were tested to ensure that no faults were present in the scintillating material itself or in the joins between scintillators and light guides. This was done using a β -emitting strontium-90 source to simulate the electron beam incident on the scintillators. Spectra of number of electrons against electron energy were produced. A linear decrease in signal amplitude was found with increasing scintillator width. Some old NE 111 scintillators were also tested and found to give a light output one to two orders of magnitude lower than the new EJ200 pieces, due to the aforementioned radiation damage.

3.5.2 A/D Card Tests

The amplifier / discriminator cards for the FPD read-out were constructed by external supplier ZOT Electronics and finished in Glasgow. These were tested before installation to the FPD array.

A light pulser was used to simulate the signal from a scintillator, as shown in figure 3.12. The current drawn from the LV supply was noted. If this exceeded

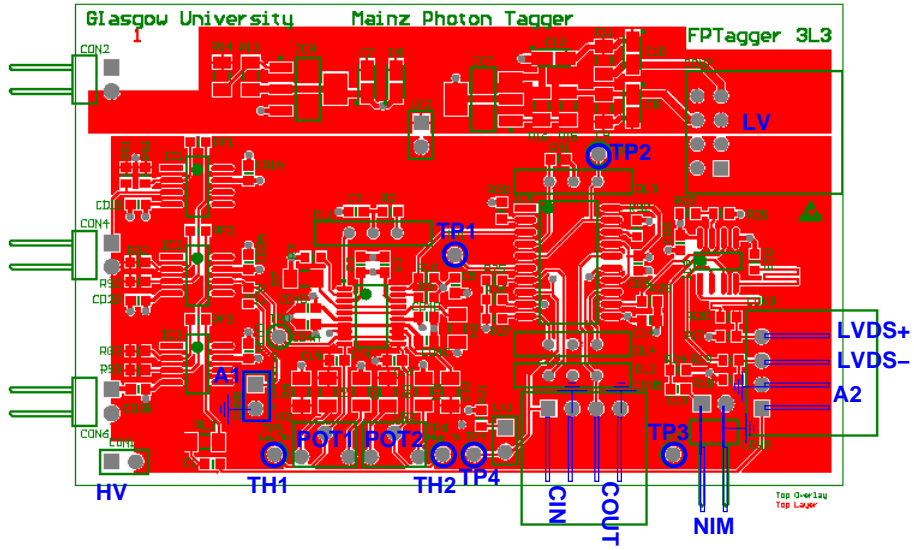


Figure 3.13: Diagram of a tagger A/D card, with test points highlighted in blue [72].

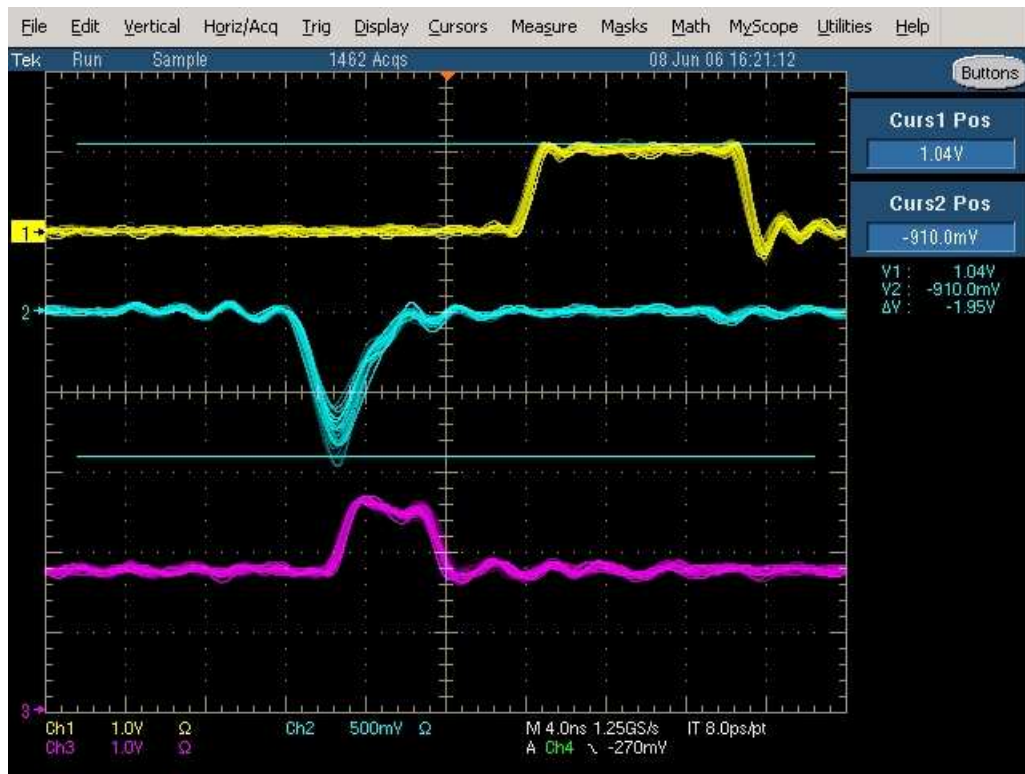


Figure 3.14: Specimen scope display for $LVDS_+ - LVDS_-$ (yellow), A2 (cyan) and TP1 (magenta) signals [72].



Figure 3.15: Left: The focal plane detector frame. Right: Scintillators mounted therein.

~ 400 mA, the card was deemed to be faulty. Using the Tektronix Scope, the DC offset on the A1 (analogue) signal, V_{A1DC} — in mV — was noted. Test points are shown in figure 3.13. Potentiometers POT1 and POT2 were then adjusted to set the low (V_{low}) and high (V_{high}) comparator thresholds, also in mV, as follows:

$$V_{low} = V_{A1DC} - 40 \quad (3.2)$$

$$V_{high} = V_{A1DC} - 400 \quad (3.3)$$

Signals from output pins TP1-4, NIM, A2 and LVDS (see figure 3.13) were viewed using a digital oscilloscope. A specimen plot showing the A2, TP1 and differential LVDS signals is displayed in figure 3.14.

The majority of cards were found to draw the correct current and show output similar to that in figure 3.14. Some cards gave no signals while others showed faults such as ringing or A1 D.C. offset close to zero. These were repaired prior to installation to the focal plane detector.

3.5.3 Refurbishing the Focal Plane Detector

The FPD frame (see the left hand side of figure 3.15) from the 885 MeV tagger [65] was re-used with some alterations. New cable runners were attached, along with distribution boards for the high voltage. The new scintillators with their light guides

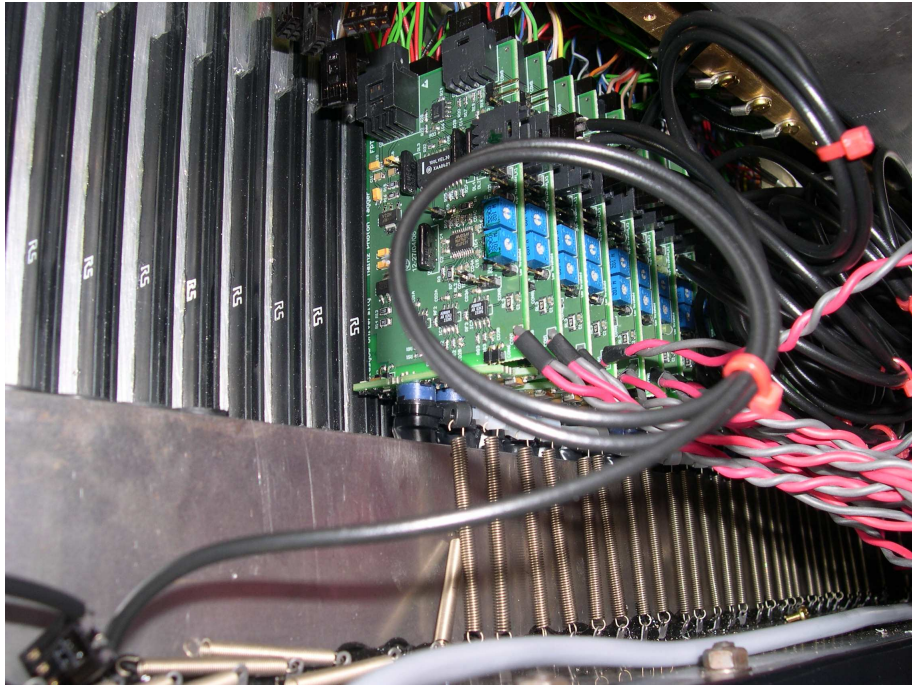


Figure 3.16: A/D Cards mounted in the FPD frame with red and black HV cables (right), black coincidence cables (centre) and red and green LV cables (top).

were installed as shown on the right hand side of figure 3.15. These were shielded by light-proof black Tedlar (PVF).

The FPD frame was replaced in the experimental hall and attached to the dipole before the A/D cards and PMTs were installed as shown in figure 3.16. Surveying found the frame to be within ~ 1 mm of its original position with respect to the magnet [5]. The frame and magnet must be electrically isolated. A short circuit was found and removed by putting rubber around the screws connecting the frame and magnet and by placing plastic spacers between the two.

3.5.4 Cabling: HV Supply, LV Supply and Signal Read-Out

New cables were constructed and tested for the LV supply and the coincidence, analogue and LVDS signals. These are shown in figures 3.16 and 3.17.

Channels	Current (A)	Voltage (V)	Current Lim (A)	Voltage Lim (V)
LV ₁ : 193–352	57.7	+5	61.0	+4.5 to +5.5
LV ₂ : 193–352	38.1	-5	41.0	-4.5 to -5.5
LV ₃ : 0–192	71.7	+5	77.5	+4.5 to +5.5
LV ₄ : 0–192	47.9	-5	55.0	-4.5 to -5.5

Table 3.1: LV PSU voltages, currents and limits thereof [71].

Low Voltage

Low Voltage (LV) was provided by 4 180 A Agilent power supply units (PSUs), shown in figures 3.10 and 3.11. 200 A cabling connected these to three bus bars (+5 V, 0 V, -5 V) inside the frame, from which wiring harnesses distributed power to the A/D cards. The current drawn was proportional to the frequency at which logic components on the cards switch states, so was used to assess noise in the FPD system.

Instability in the PSUs was found to cause false triggering on comparator chips. The LV supplies rippled at a frequency of tens of kHz as their output current increased [73]. Several measures were employed to tackle this. Capacitors and diodes were attached between the bus bars and the ground on the tagger electronics rack. The bus bars were split to use 2 PSUs apiece. The PSU’s feedback sensors were employed to ensure that ± 5 V was delivered. Thus the LV is now stable and reliable. The operational currents and voltages are shown in table 3.1.

High Voltage

PMT high voltage (HV) was supplied by a CAEN 1527 mainframe (see figures 3.10 and 3.11) powered by 3 A1532 48 V, 750 W PSUs [73]. The upper PMT voltage limit was set to 1500 V. Individual PMT supply voltages were set separately, using QDC spectra.

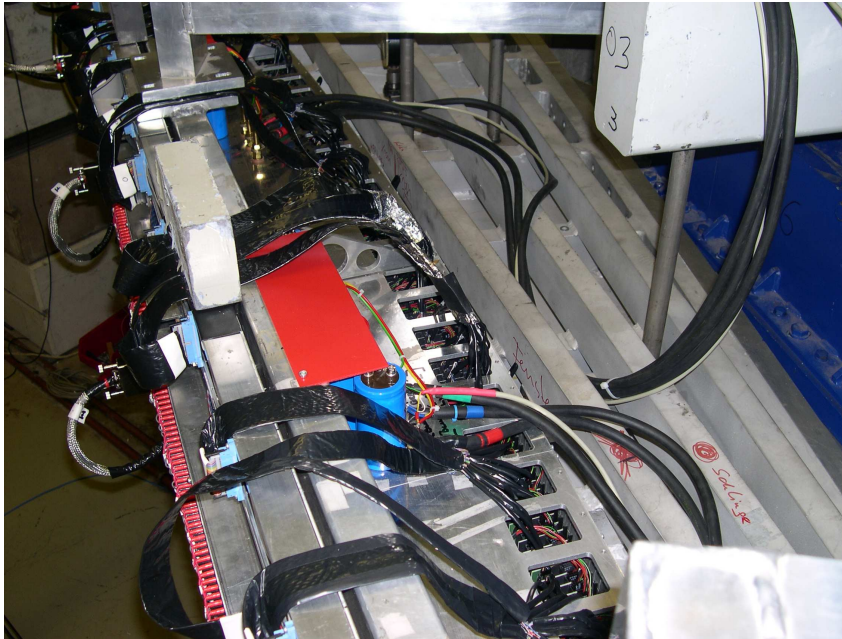


Figure 3.17: The tagger from above, with flat black signal cables, round black LV cables, silver HV cables and blue capacitors.

LVDS, Analogue and Coincidence Cables

LVDS logic signals were carried by SCSI cables; analogue signals by ribbon cable. These were plugged into a delay box, wherein delay was provided by ~ 30 m long twist and flat cables. In order to make hardware coincidences between adjacent cards, a logic signal from each card was supplied to its higher electron momentum neighbour by co-axial cable.

Assessment of signal quality was carried out during the commissioning of the tagger. Many channels showed a lot of noise initially. Signal cables were therefore wrapped in aluminium foil for shielding, then covered with black tape to protect this, as shown in figure 3.17. Lead bricks placed on top of these along the focal plane detector prevented noise from movement in the cables.

Further problems were discovered in the TDCs and Scalers. Two or three neighbouring channels would record counts when only one detector fired. The cause of this was identified as miss-connection due to SCSI cables being incompatible with the CATCH modules. Printed-circuit-board (PCB) converters were inserted between the cables and fanout.



Figure 3.18: The completed Glasgow-Mainz Photon Tagging Spectrometer.

3.6 Beam Collimation and Tagging Efficiency

In order to make an accurate cross-section measurement, photon flux on the target must be known (see section 5.5). Hence the photon beam was collimated in order to keep the photon beam diameter within that of the target. This also minimised uncertainty in the reaction vertex position and avoided interactions occurring between the beam and material other than the target, which would constitute background. For this experiment, 4 cylindrical lead collimators, of length 40 mm and bore 4 mm, were aligned to the beam axis, defining beam circumference. Further downstream, a 30 mm-wide collimator, in conjunction with a permanent magnet, acted as a scrubber, removing from the photon beam line electrons produced by photon interactions in the first collimator.

This means that not every electron detected in the tagger will have its corresponding photon hit the target. The proportion which do is known as "tagging efficiency", defined thus for each tagger channel:

$$\varepsilon_{tagg} = \frac{N_{\gamma}}{N_{e^{-}}} \quad (3.4)$$

where N_{γ} is the number of photons after collimation and $N_{e^{-}}$ is the number of

electrons detected by the tagger.

Tagging efficiency was not measured in parallel with normal production running, but in separate runs interspersed throughout each data taking period. This was done using the tagger and a 25 cm³ lead-glass Cerenkov detector in coincidence. The latter was placed directly in the photon beam, downstream of the Crystal Ball and TAPS, in front of the photon beam camera. Subject to threshold effects, this detected the full Bremsstrahlung spectrum, requiring a very low intensity beam so as to avoid saturation. For the present work, a rate of 5 kHz in the *Pb*-glass detector — corresponding to a beam current of ~ 0.1 pA — was used, giving a tagger hit rate at the Hz level. One advantage of this very low rate was that the probability of random coincidences (described in section 5.2.1) was negligible.

3.7 Energy Calibration

The tagger must be calibrated in order to measure the incident electron energy for each tagger channel. Ideally, this would be done using the MAMI beam at every available 15 MeV step in electron energy, see section 4.2.1. However, time constraints render this impracticable. Instead, a selection of data was taken for 7 different energies. This was used in combination with simulation code to produce calibrations.

For the pre-upgrade tagger, a program called *TagCal* [74] was written to create calibration files for given beam energies and corresponding dipole fields. This was used as a basis for the upgrade calculation.

3.7.1 MAMI Data

For the initial calibration measurements, five MAMI electron beam energies were used as follows: 195.2, 405.3, 570.3, 705.3 and 855.3 MeV. Later measurements were made with beam energies of 1002.3 and 1307.8 MeV. No radiator was utilised. For each energy, the field required to dump the beam in the normal way was determined. The dipole current was then increased incrementally, moving the beam along the focal plane detector array in a series of steps, to simulate different tagging electron

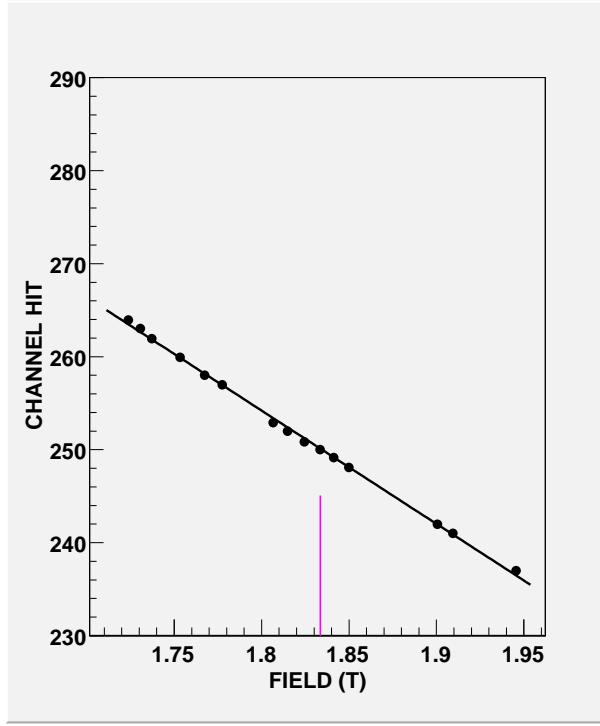


Figure 3.19: Channel hit against tagger dipole field for the 1002 MeV electron beam. Black circles represent data, the black line is a straight line fit to these, with the pink line marking the dumping field of 1.834 T for the 1508 MeV electron beam.

energies. Fields were used in the range $\pm 5\%$ of the dumping fields for beams of 883 MeV and 1508 MeV: 1.057 T and 1.834 T respectively. Initially, broad-ranging scans were carried out. Later, more detailed scans were made over smaller ranges to search for overlap boundaries of FPD channels. These points gave more precise calibration measurements.

The NMR reading and tagger hit position were recorded for each measurement, with the latter determined from TDC spectra. This was used to plot hit channel against magnetic field strength for each beam energy, as shown in figure 3.19.

The magnetic field used is related to an equivalent electron energy by the following linear approximation:

$$E' = \frac{EB}{B'} \tag{3.5}$$

where E' is equivalent electron energy, E is beam energy, B is the dumping field in the main experiment and B' is the magnetic field used for the calibration point. Figure 3.20 shows the plot of equivalent energy against focal plane detector hit

position. It includes data from the original five electron beam energies: 195 MeV in pink, 405 in light blue, 570 in dark blue, 705 in green and 855 in red. Smaller errors were assigned to those hits made on or close to scintillator edges.

The output of the *TagCal* calculation was plotted along with the measured points, as shown by the black line in figure 3.20. The simulated points were then interpolated between to allow a comparison of measurement and simulation. This energy difference was calculated as follows:

$$E_{diff} = E_{TC} - E_{meas} \quad (3.6)$$

where E_{diff} is the difference between simulated and measured energies, E_{TC} is interpolated *TagCal* energy and E_{meas} is equivalent electron energy. This was plotted against tagger channel, as shown in the lower portion of figure 3.20. These plots were produced for both beam energies of 1508 and 883 MeV.

However, discrepancies between these overlapping energy scans revealed that field shape is dependent on field magnitude, rendering the error too large for all measured points to be used in the calibration. The required correction is a smooth function of $B - B'$, but is of unknown shape. The assumption that it is linear may be adequate for small $B - B'$ [75], but is not thought to be sufficiently accurate over the range encountered here. Instead, the calibration used only the five or seven data points measured at the correct dumping fields of 1.057 and 1.834 T, as displayed in figure 3.23. These points were obtained by plotting the hit position against field for measurements within $\pm 5\%$ of the field values and interpolating to the correct field using linear fits [5].

3.7.2 Calculation

The increase in dipole field provided by the upgrade meant that the position of the field boundary changed, rendering the old field map — and hence the original *TagCal* program — no longer sufficiently accurate. No complete field map exists for the upgraded magnet. However, it has been calculated using TOSCA and limited measurements were made, as described in section 3.4.2. A comparison of these measurements with the TOSCA results (see figure 3.5) suggests that the latter is

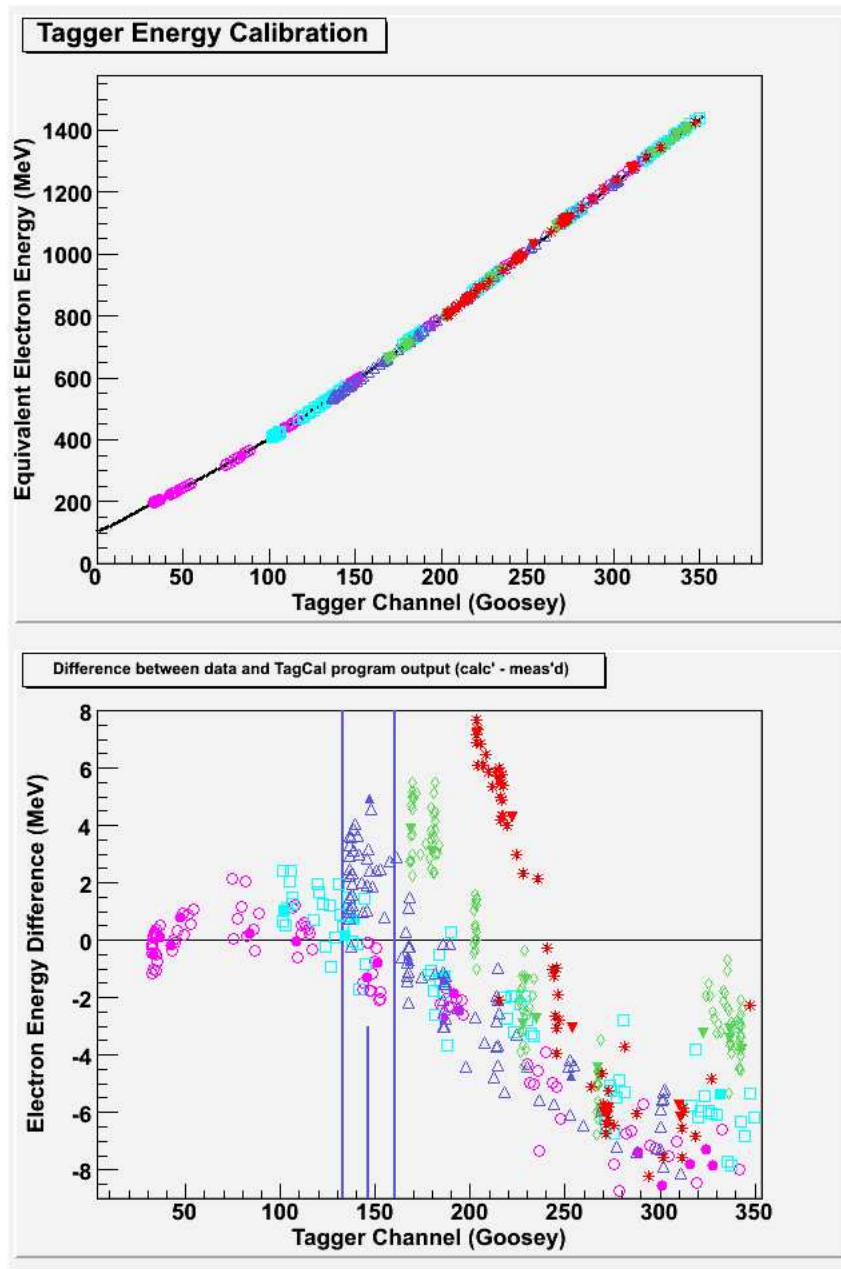


Figure 3.20: Top: Initial tagger calibration measurements and calculation. Data are represented by pink circles (195 MeV electron beam), light blue squares (405 MeV), dark blue triangles (570 MeV), green diamonds (705 MeV) and red stars (855 MeV). The black line shows the output of the *TagCal* calculation. Bottom: the difference between measured values and the calculation. Vertical blue lines enclose the measurements made within $\pm 5\%$ of the dumping field for the 570 MeV electron beam.

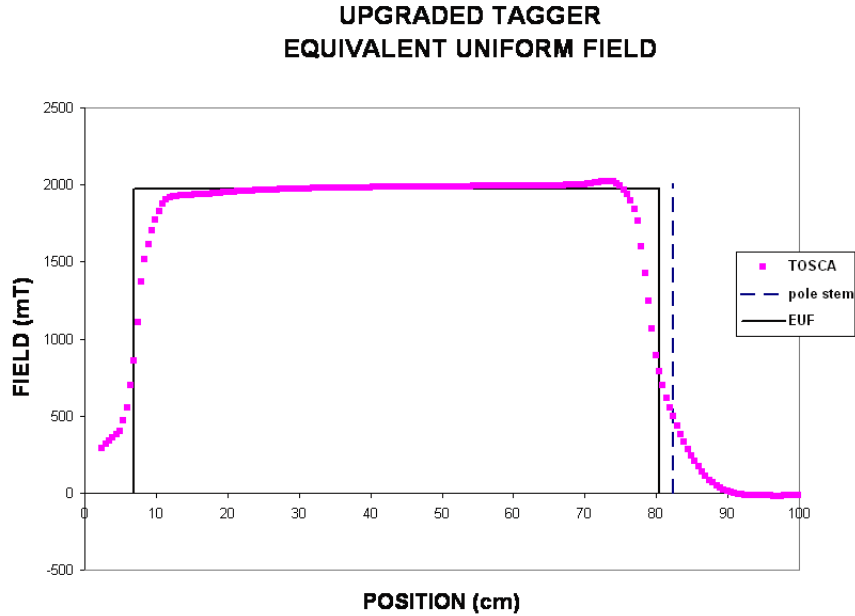


Figure 3.21: TOSCA calculation of the tagger field along line Bb and the modelled effective uniform field used in the tagger calibration.

reliable. Therefore, this was used to model an equivalent uniform field (EUF), shown in figure 3.21. The effective field boundary was calculated by equating the integrals of $B \cdot dl$ in the EUF to that in the TOSCA field, as shown in figure 3.22.

The position of the focal plane detector frame was surveyed after its post-upgrade re-installation. The relative positions and angles of scintillators within this are known from its design [65]. Electron trajectories are made up of circular arcs within the EUF region of the dipole and straight lines outwith, so can be calculated geometrically. The NMR probe measured the field strength near the radiator. The strength of the EUF was taken as the NMR reading multiplied by a factor, f . This was adjusted to fit the calculation to the measured points, resulting in $f = 1.0098$ for 885 MeV and $f = 1.0003$ for 1508 MeV.

These changes to *TagCal* were implemented as a new program, *ugcal* [76]. The output of this is shown in figure 3.23. For 1508 MeV most measurements differ from the *ugcal* calculated values by 1.5 MeV or less, except at the lowest photon energies, where the discrepancy is ~ 4 MeV. This effect is thought to be due to the incorrect assumption of field uniformity. It varies smoothly over the tagged energy range, so

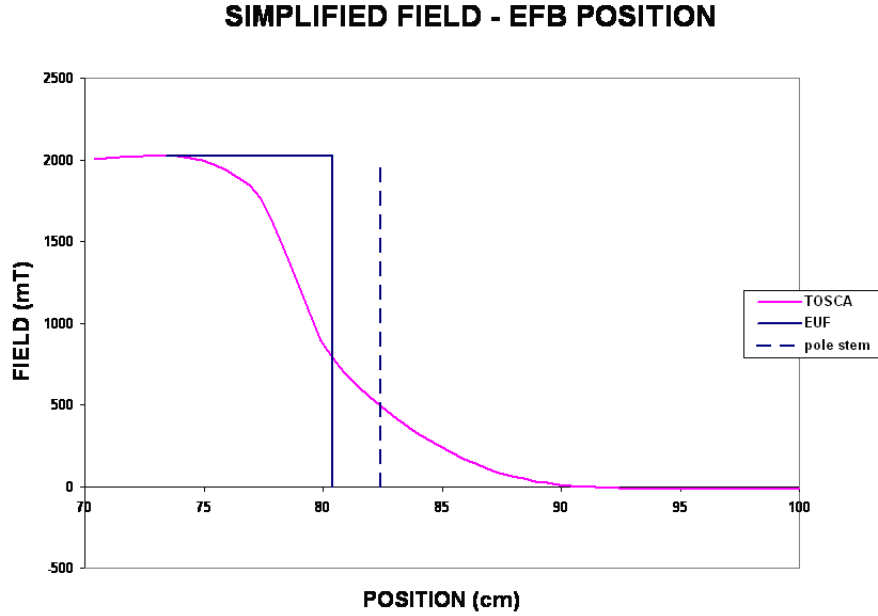


Figure 3.22: Position of the effective field boundary relative to the pole stem and TOSCA calculated field.

a correction can be obtained using a fit to the calibration points, shown in the lower part of figure 3.23.

Uncertainties in electron trajectories due to the field dips described in section 3.4.2 cause a variation from the assumed smooth calibration. Figure 3.24 shows the estimated deviations, calculated by assuming a uniform field in the dipole, except at the dips, and a zero field elsewhere. Dips within 30 mm of each tagging electron trajectory are considered, with their combined effect on exit position and bend angle calculated. The fractional effect on bend angle is assumed to be equal to the fractional difference between the field integral for a uniform field with no dips and the integrated field when the dips are present. The size of deviation depends upon the number of screws lying near a given trajectory. This explains the peaks of different sizes in figure 3.24. For example, the $\frac{E}{E_0} = 0.18$ trajectory crosses one screw, while the $\frac{E}{E_0} = 0.41$ trajectory crosses three. The solid line results from smoothing these deviations. The peaks differ from the smoothed line by up to ± 0.6 mm. This results in an uncertainty of $\sim \pm 0.2$ MeV for the 1.5 GeV beam.

At this energy, the uncertainty in the measured calibration points, including the

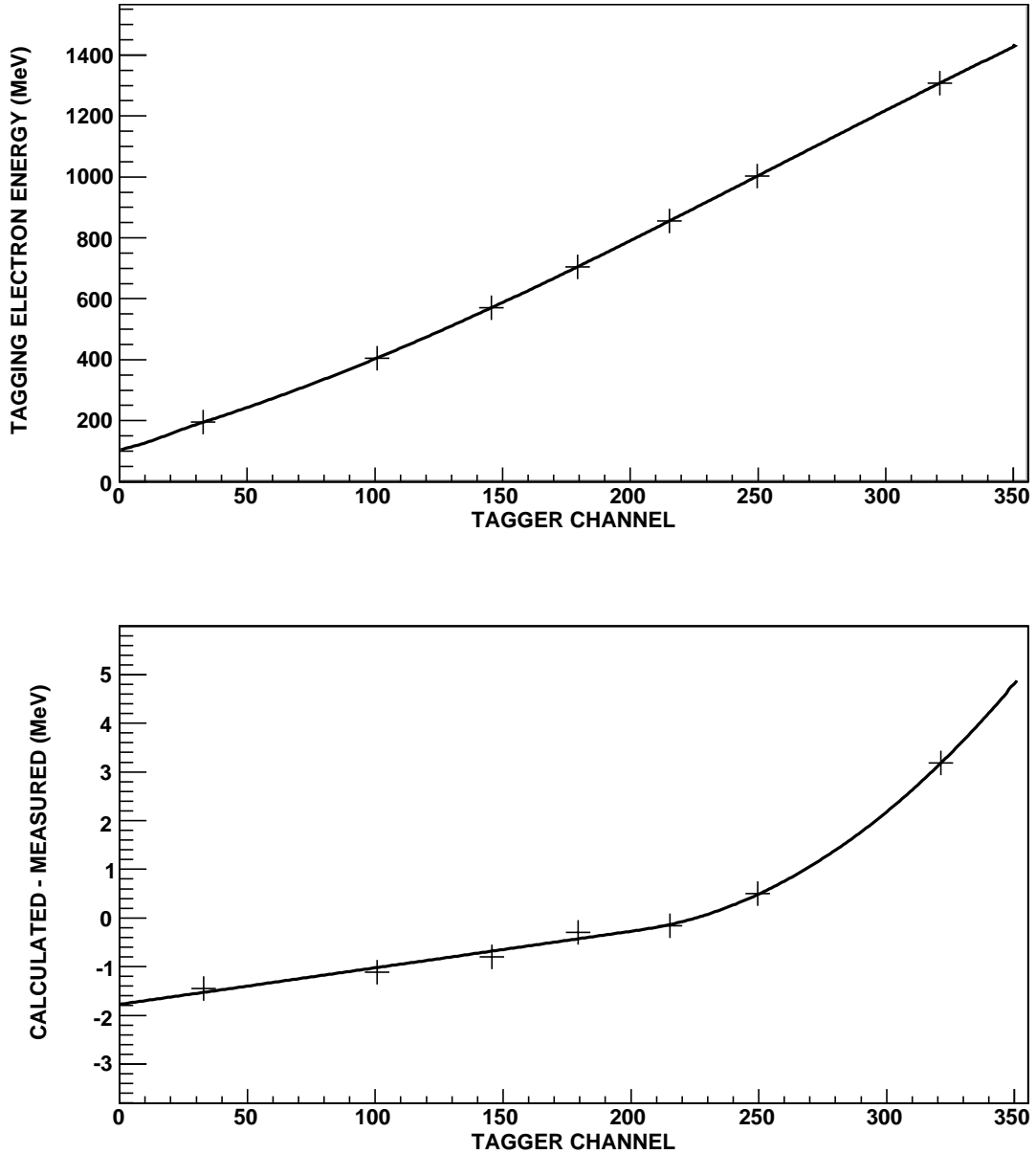


Figure 3.23: Top: Final tagger energy calibration for a main beam energy of 1508 MeV (1.834 T field) measured using MAMI energies of 195.2, 405.3, 570.3, 705.3, 855.3, 1002.3 and 1307.8 MeV (crosses) and the calibration calculated assuming a uniform field (line). Bottom: Difference between the calculated and measured calibrations (crosses) and a smooth fit to the seven measured points (line), indicating the small correction to the calculated calibration required because of large-scale field non-uniformity [5].

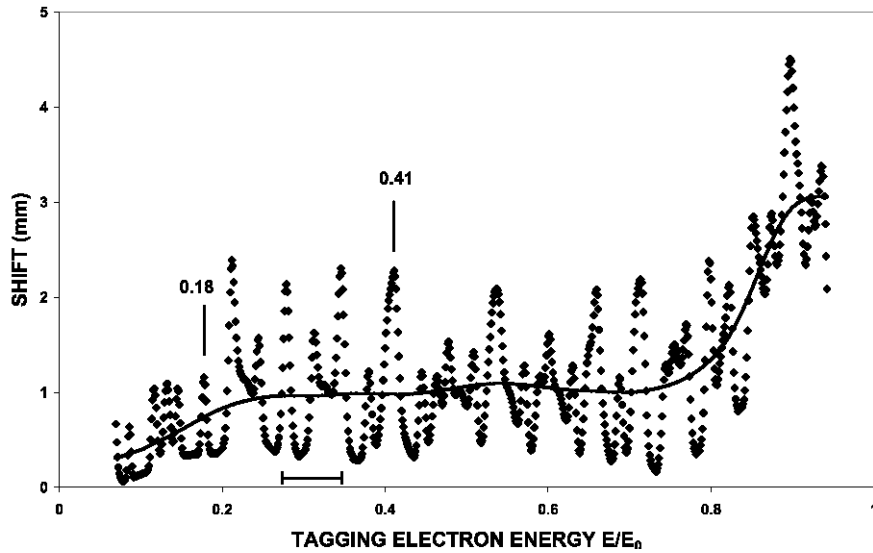


Figure 3.24: Deviation in electron trajectories caused by dips in the magnetic field due to M8 screws [5]. The line results from smoothing the points.

uncertainty in MAMI beam energy is $\sim\pm 0.3$ MeV. The possibility of slight variations in the pole gap has been suggested by measurements of the pole shim thicknesses. This could also cause deviation from the smooth calibration between the measured points. Combining this with the uncertainty due to the fit correction in figure 3.23 gives an uncertainty of $\sim\pm 0.5$ MeV for channels up to ~ 270 . For lower photon energies, this could be considerably larger, but only channels 1 to 224 were used for this work.

Chapter 4

Experimental Set-Up

4.1 Overview

The Mainzer Microtron (MAMI) — located within the Institut für Kernphysik, Mainz — provides a mono-energetic electron beam, with available energies ranging from 180 to 1604 MeV. This beam is used in four experimental halls, as shown in figure 4.1: for electron scattering experiments in the A1 hall, for tagged photon experiments in A2, for parity violation experiments in A4 and for X-ray experiments in X1. The present work was carried out in the A2 hall, where the incoming electron beam from MAMI is incident on a radiator producing — by the Bremsstrahlung process — the photons necessary to trigger reactions including η photoproduction. The Glasgow-Mainz Photon-Tagging Spectrometer momentum analyses the post-Bremsstrahlung electrons, thus determining the energy composition of the photon beam. The tagger, and upgrade thereof, are described in detail in chapter 3.

The η -decay channels of interest both have single proton, multiple photon final states. The detection of multiple photons requires a high-efficiency detector system with good timing resolution. The proton was reconstructed by missing mass techniques (as described in section 5.6), requiring high energy resolution. A photon calorimeter with such properties was provided by the CB, PID and TAPS set-up in the A2 Hall. The Crystal Ball (CB) gave energy and position information for all reaction products, while the Particle Identification Detector (PID) differentiated between charged and neutral particles. These encompassed much of 4π , with a

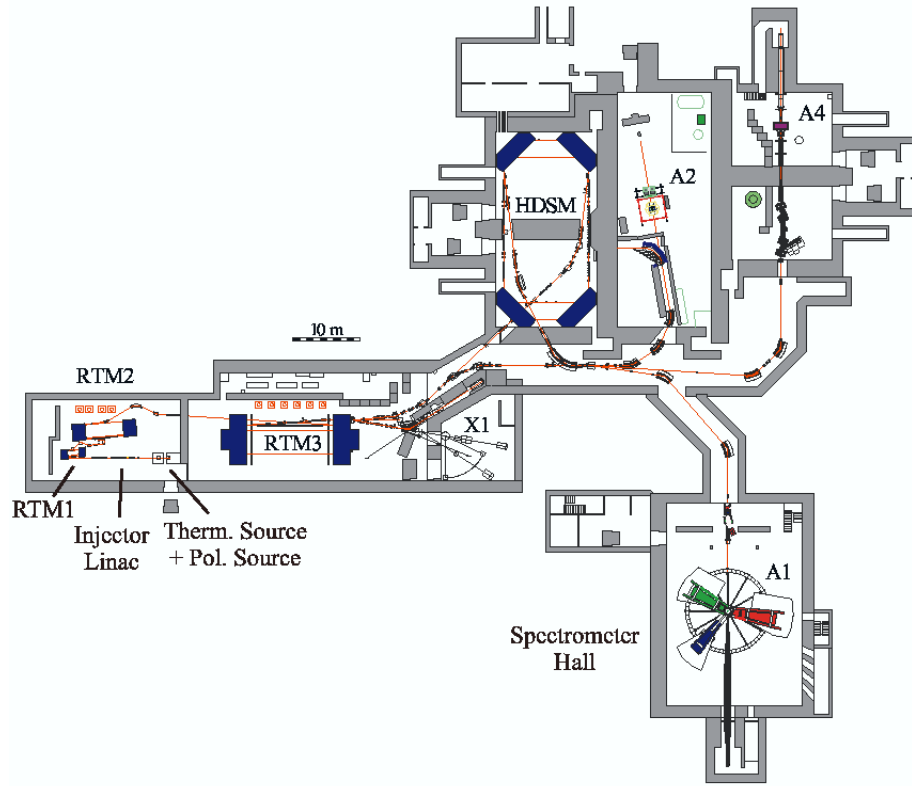


Figure 4.1: Schematic of MAMI and the experimental halls [78].

gap of $\pm 20^\circ$ in the forward angular region. This was covered by TAPS, which gave calorimetry, tracking and particle charges. These components are described in detail in this chapter.

4.2 MAMI

MAMI provides a 100% duty factor, continuous wave (cw) electron beam of energy up to 1604 MeV and maximum current of $100 \mu\text{A}$ [77]. The beam is of very high quality in terms of emittance, stability and reliability. MAMI consists of an initial injector linear accelerator (linac) feeding to three cascaded race track microtrons (RTMs), which in turn feed an harmonic double sided microtron (HDSM). The accelerator system is depicted in figure 4.1.

MAMI-A, completed in 1979, originally comprised a Van-de-Graff injector plus RTMs 1 and 2 [78]. This produced a maximum of 187 MeV electron beam energy at $65 \mu\text{A}$ current, exceeding the pion production threshold. 1990 saw the realisation of

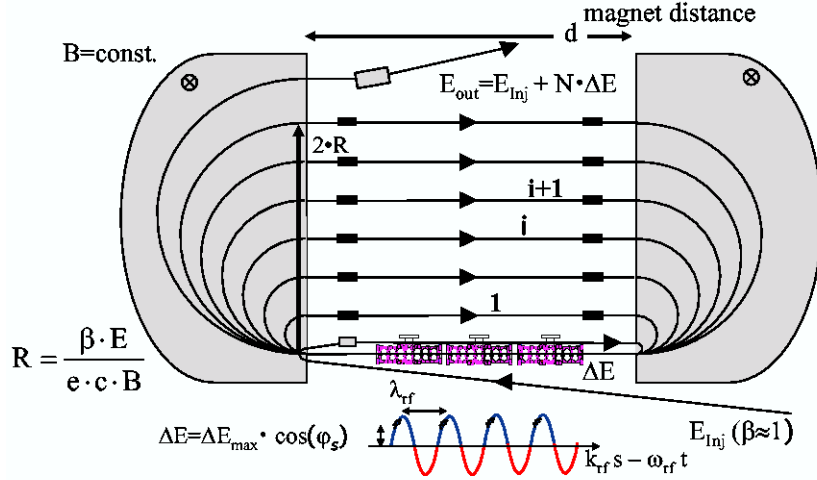


Figure 4.2: Schematic of a race track microtron [78].

MAMI-B, increasing the energy and current production capabilities to 883 MeV and $100 \mu\text{A}$, thus facilitating the production of η mesons. This involved the replacement of the Van-de-Graff with an 100 keV electron source and a 3.5 MeV linac, combined with the construction of a third RTM. The latest development was the construction of MAMI-C, increasing the maximum beam energy to 1508 MeV, surpassing the strangeness production threshold. This entailed the addition of the HDSM and was first operational in December 2006, compelling the upgrade of the tagger, as detailed in chapter 3. Further work in 2008 saw the maximum electron energy rise to 1557 MeV, then again to 1604 MeV in 2009.

4.2.1 MAMI Race Track Microtron Cascade

The principle of an RTM is to accelerate a beam of charged particles — electrons in the case of MAMI — by multiple recirculations of the beam through a single linac [79]. An RTM, illustrated in figure 4.2, therefore consists of said linac flanked by two 180° bending dipole magnets. The electrons' energies increase by ΔE with each subsequent passage through the linac, while the radii of their paths through the magnetic fields increase correspondingly. The magnets have uniform fields, returning the electrons to the linac entrance after each recirculation.

The linac consists of multiple standing wave cavity sections, powered by radio

RTM	1	2	3
Injection Energy (MeV)	3.97	14.86	180
Number of Turns	18	51	90
Extraction Energy (MeV)	14.86	180	883

Table 4.1: Parameters of MAMI RTMs [78].

frequency (rf) klystrons. At MAMI, these are normal conducting and operate at room temperature. The race track set-up allows a relatively small acceleration gradient, since it is reapplied many times. In turn, limiting the gradient allows a continuous wave beam to be produced. When the desired beam energy has been reached, a “kicker” magnet ejects the beam from the RTM.

An RTM has excellent energy resolution and phase stability intrinsically. The time taken for each recirculation must be an integer multiple of the period of the rf supply, ensuring that the same phase of the alternating voltage always acts on a given particle bunch in each pass through the linac. If any bunch has greater or less than the desired energy, it will be out of phase and so under- or over-accelerated accordingly, thereby returning to the optimum phase with respect to the rf supply. Therefore the small spread in energies produced by an RTM is mainly due to synchrotron radiation.

At MAMI, electrons are produced by an electron gun, in which they are boiled off the cathode via thermionic emission, then accelerated to the anode by an 100 kV potential. The 3-stage injector linac then accelerates these up to 3.97 MeV. The injection and maximum extraction energies along with the number of turns of each MAMI RTM are summarised in table 4.1. Extraction is possible at 15 MeV intervals from 195 to 883 MeV. At 883 MeV, the energy spread is a mere 60 keV full width at half maximum (FWHM), with a maximum current of 100 μ A.

4.2.2 Harmonic Double-Sided Microtron

The HDSM [78] consists of two linacs and four dipole magnets which recirculate the electrons, as depicted in figure 4.3. This follows the same general principle as an

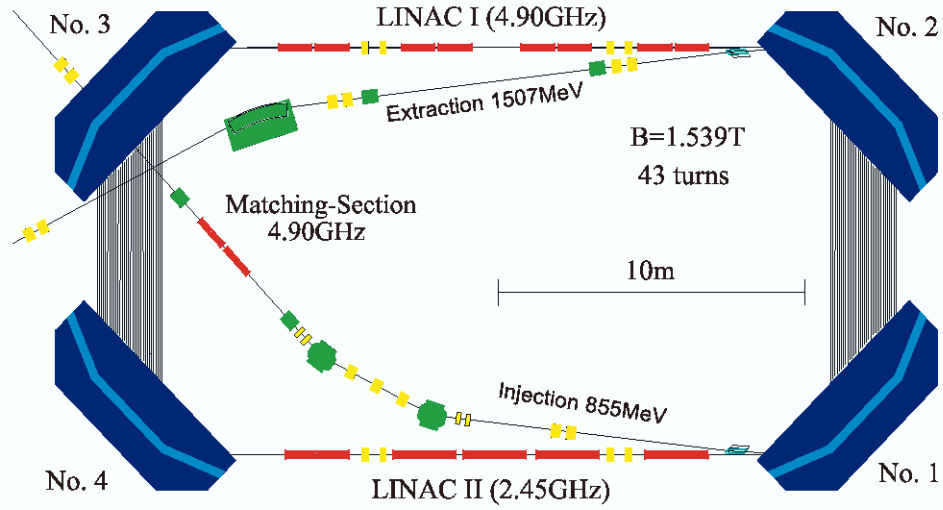


Figure 4.3: Schematic of the harmonic double sided microtron [78].

RTM and is also known as a “bicyclotron”. Again, normal conducting rf-accelerator structures and normal conducting iron core magnets were selected, with electron path radii increasing in proportion to electron energy. 90° -bending dipoles, with magnetic flux density varying from 0.95 to 1.53 T, are employed to recirculate the beam.

The necessary accelerator properties, coupled with the physical and spatial constraints of the pre-existing buildings and parameters of RTM3 ($\Delta E = 41.1 \text{ MeV}\cdot\text{turn}^{-1}$ and rf-gradient = $1 \text{ MV}\cdot\text{m}^{-1}$) determined that the rf frequency of linac 1 should be 4.90 GHz with every second cavity populated, allowing for 10m-long linacs. Linac 2’s frequency of 2.45 GHz, with every cavity populated, simplifies maintenance of phase stability.

During this work, the HDSM had an input energy of 855 (from RTM3) and maximum output energy of 1508 MeV, with 43 recirculations. Extraction was possible at 15 MeV intervals from 872 to 1308 MeV. At 1508 MeV, the energy spread was 110 keV (1σ), *ie.* 259 keV FWHM. Recent work has led to an increase in maximum energy to 1604 GeV, whilst retaining the same acceleration optics. Extraction is now available at 15 MeV intervals from 872 to 1557 MeV.



Figure 4.4: Liquid hydrogen target cell [80].

4.3 Target

Liquid hydrogen was used as a proton target [80]. This was contained within a cylindrical 125 μm -thick Kapton cell, shown in figure 4.4, surrounded by 8 layers of superisolation foil — 8 μm of mylar and 2 μm of aluminium — in addition to a 1 mm-thick CFK vacuum tube. The Kapton cell has length 4.76 cm and diameter 4.0 cm, giving a volume of $\sim 60 \text{ cm}^3$ when cold, see figure 4.5. Using the 4 mm collimators described in section 3.6, the photon beam is $\sim 15 \text{ mm}$ across when incident on the target, well within the diameter of the cell window. Pressure in the target cell was 1080 mBar during operation at a temperature of 20.5 K.

The target system consisted of an hydrogen gas storage tank, a compressor, a liquefier with a reservoir of liquid H_2 and a supply line connecting this to the target. The effective target thickness was:

$$\rho_t = 2.013 \times 10^{-7} \mu\text{b}^{-1},$$

as described in section 5.4.2.

The shape of the exit window was measured, so that the main uncertainty in target length came from deformation of the entrance window. This was extrapolated from measurements made before installation to the vacuum system. The cell length in the beam axis at 20.5 K was $(47.6 \pm 0.3) \text{ mm}$, an uncertainty of 0.63%. Another contribution to the uncertainty in effective target thickness came from potential boiling of the liquid hydrogen [81]. Two resistive heaters were used to prevent the hydrogen from freezing. The operation of these caused a variation in pressure

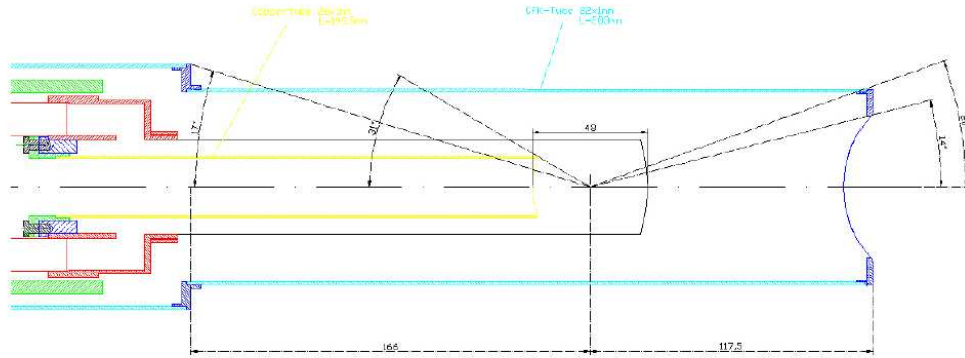


Figure 4.5: Schematic of the target cell [80].

of ± 0.5 mBar, equivalent to $\pm 0.046\%$. Pressure and temperature have a linear relationship, so this percentage uncertainty translates directly to the temperature. The target was heated for $\sim 20\%$ of beam running time, so the overall uncertainty in effective target thickness due to bubble formation is a negligible $\sim 0.01\%$.

Empty target measurements were made under normal running conditions, but with the target cell evacuated. This allowed assessment of reactions induced in the Kapton and other material surrounding the hydrogen.

4.4 Crystal Ball System

The Crystal Ball is a highly segmented photon detector, providing energy and position information for neutral and charged particles. Within this is situated the Particle Identification Detector, surrounding the target cell, as shown in figure 4.6. The PID provides energy loss and azimuthal angular information on charged particles, adding charged-particle identification capabilities. The Multi-Wire Proportional Chambers (MWPCs) depicted were not in place for the present work. These are used for charged particle tracking, so were not needed when only photon detection was required.

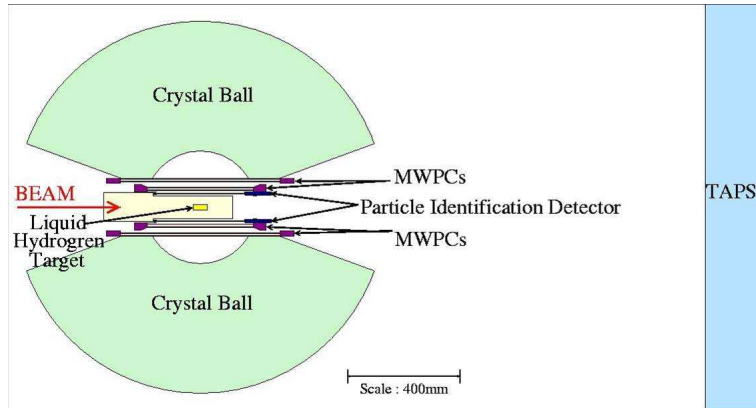


Figure 4.6: Schematic of the detector system including the lH_2 target, PID, CB and TAPS [82]. The MWPCs shown were not in place for this experiment.

4.4.1 Crystal Ball

The Crystal Ball (CB), depicted in figure 4.7, was originally envisaged to detect photons of energies 1 to 1000 MeV produced in high energy e^+e^- collisions at the Stanford Linear Accelerator Center (SLAC) in the USA [83]. It was first installed in the Stanford Positron Electron Accelerator Ring (SPEAR) in 1978 where the states $J/\psi(3100)$ and $\psi'(3700)$ were studied along with the $\psi''(3770)$. In 1982 the CB moved to the Deutsches Elektronen Synchrotron (DESY), Germany, where it was used in the DORIS experiment to take data on the Υ until 1987. It then returned to Stanford for storage, until being transported to Brookhaven National Laboratory in 1995 for use at the Alternating Gradient Synchrotron (AGS) [84]. There, hadron spectroscopy was carried out using pion and kaon beams. 2002 saw the CB cross back over the Atlantic to Mainz for experiments with tagged photon beams. Here, the CB readout electronics were entirely replaced (see section 4.6.1) before data collection began with MAMI-B. This focused mainly on pion photoproduction studies [82, 85] along with work on η production at threshold [86, 87]. The completion of MAMI-C in 2006 crossed the strangeness production threshold [88] and allowed for more complete η investigations encompassing the entire $S_{11}(1535)$ region and higher [66].

The Crystal Ball is a hollow sphere of 672 thallium-doped sodium iodide ($NaI(Tl)$) crystals, which give high detection efficiency down to low energy and good energy resolution due to their high light output, as well as excellent angular resolution re-

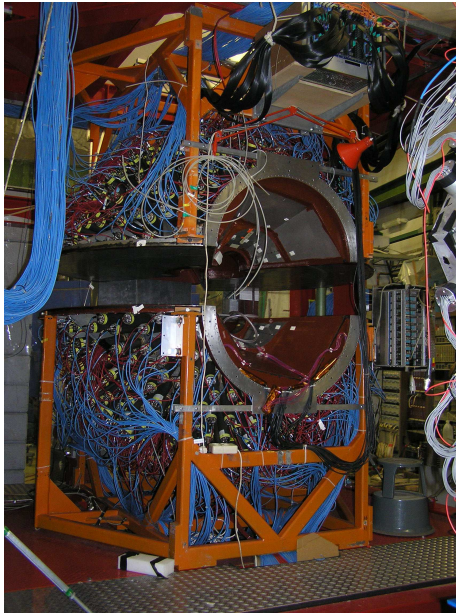


Figure 4.7: The Crystal Ball. Here the top and bottom hemispheres are separated to allow access to the target and PID region.

sulting from the high segmentation of the ball. The CB is modelled on a polyhedron with 20 triangular faces (“major” triangles), an icosahedron, as shown in figure 4.8. Each face is divided into 4 “minor” triangles, which are subdivided into 9 further triangles. Each of these is the base of a truncated pyramidal *NaI* crystal, see figure 4.9. These are 40.6 cm (15.7 radiation lengths, X_0) long, 5.1 cm wide at the inner edge and 12.7 cm at the outside. The result is a near-spherical geometry, with entrance and exit holes for the photon beam radially opposite to one another. It has external and internal radii of 66.04 and 25.40 cm respectively.

Each crystal is optically isolated — using white paper and aluminium foil — and connected, through a glass window and 5 cm air gap, to its own ZXRC L50 B01 PMT. *NaI(Tl)* is extremely hygroscopic, so the ball is divided into two hemispheres, hermetically sealed in a vacuum by 1.5 mm-thick ($0.09 X_0$) stainless steel with glass windows for the PMTs. The hemispheres are partitioned by two 1.6 mm stainless steel rings sandwiching a 0.8 cm air gap, at which the halves can be separated to access the target and PID region.

High energy muons, being minimum ionising, deposit ~ 200 MeV over at most 3 crystals in the CB [83]. Electrons and photons with energies in excess of ~ 20 MeV

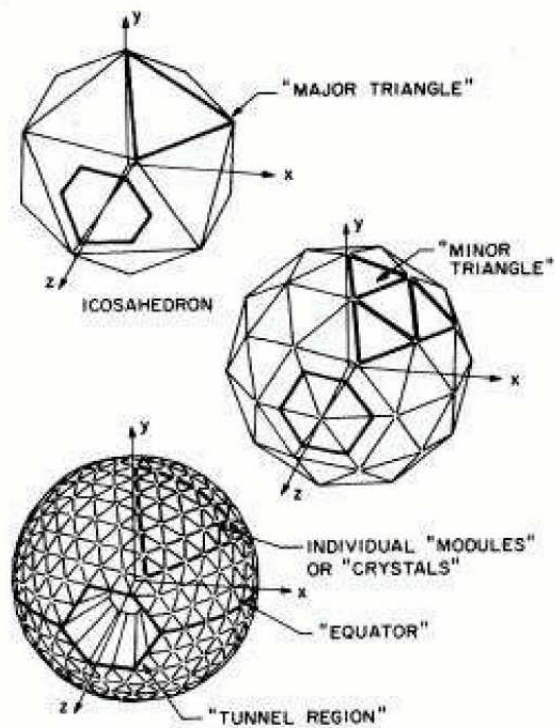


Figure 4.8: Geometry of the Crystal Ball [85]. Top: the CB is modelled on a polyhedron with 20 triangular faces (“major” triangles), an icosahedron. Middle: each face is divided into 4 “minor” triangles. Bottom: these are subdivided into 9 further triangles.

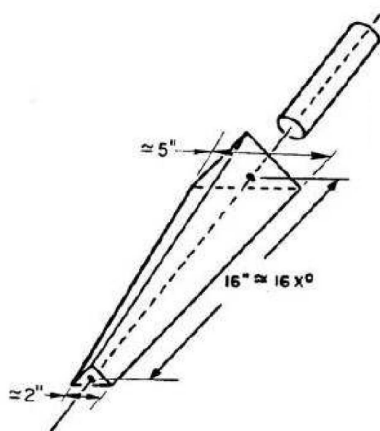


Figure 4.9: A truncated pyramidal $NaI(Tl)$ crystal from the Crystal Ball with its PMT [84].

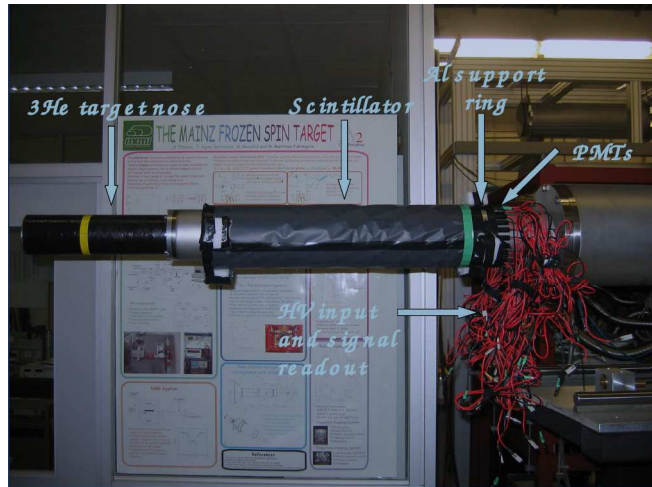


Figure 4.10: Particle Identification Detector [89].

produce electromagnetic showers, depositing $\sim 98\%$ of their energy in a characteristic pattern covering 13 crystals. Protons typically deposit energy in only one or two crystals. For hadrons, the ball is sufficiently thick to stop 425 MeV protons and 245 MeV pions [85]. The patterns of deposited energy, known as “clusters”, were analysed to reconstruct particle energies and production angles, as described in section 5.2.2.

The CB covers a solid angle $\sim 94\%$ of 4π sr with azimuthal, ϕ , angular coverage perpendicular to the beam line of 0° to 360° and polar, θ , coverage of 20° to 160° . Angular resolution is $2^\circ \leq \sigma \leq 3^\circ$ for photons of energies $50 \leq E_\gamma \leq 500$ MeV for θ ; $\frac{2^\circ}{\sin \theta}$ for ϕ . Energy resolution is $\frac{\sigma}{E} = \frac{2.7\%}{E_\gamma(\text{GeV})^{\frac{1}{4}}}$ [84].

4.4.2 Particle Identification Detector

The PID provides ΔE , precise timing and crude azimuthal (ϕ) angle information for any charged particles. The original PID was constructed in Glasgow in 2004 when the CB moved to Mainz, with a new version, PID 2, being designed, built and installed by the Edinburgh group for the MAMI-C upgrade. This is displayed in figures 4.10 and 4.11.

The PID is a cylinder of inner diameter 108.4 mm, comprising 24 EJ204 plastic scintillators of dimensions $(500 \times 15 \times 4)$ mm [89]. The cross-section of each is a right-angled trapezium, with one edge angled at 15° , minimising gaps between elements

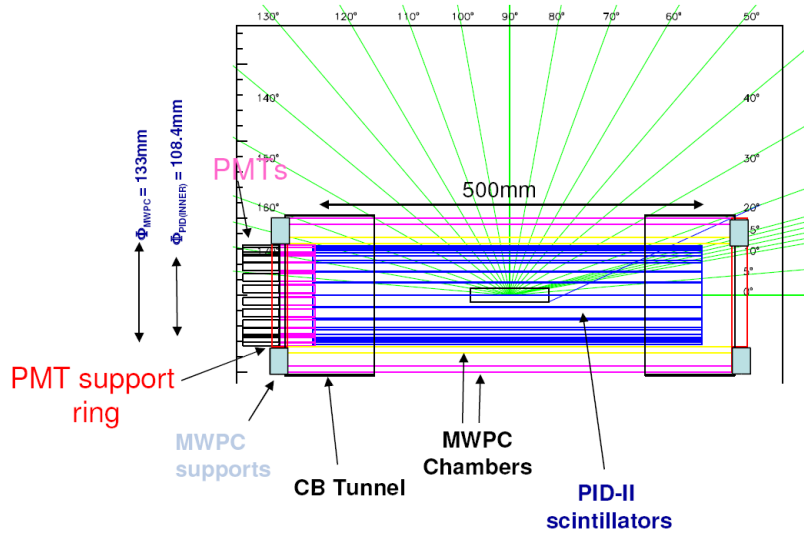


Figure 4.11: Schematic of the Particle Identification Detector [89].

[90]. The optical isolation of each scintillator is effected by wrapping in foil. The barrel as a whole is surrounded in black Tedlar (PVF) for light-proofing. Perspex light guides connect each scintillator to an individual 10 mm diameter Hamamatsu R1635 PMT, located upstream of the target.

Each scintillator covers 15° azimuthally, providing angular coverage of 360° in ϕ . Polar coverage of 15° to 165° in θ encompasses that of the CB. Energy deposited in the PID is compared to that in the CB in $\Delta E - E$ analysis. This, described in section 5.1.3, is used to differentiate between particles of differing ionisation densities such as protons, electrons and charged pions.

4.5 TAPS

The forward-angle aperture of the CB, $0^\circ < \theta < 20^\circ$, is covered by TAPS, historically the Two / Three Armed Photon Spectrometer [91], shown in figure 4.12. Complications with the analysis software led to the omission of TAPS data from the present analysis, although the detector was in place and operational during this experiment.

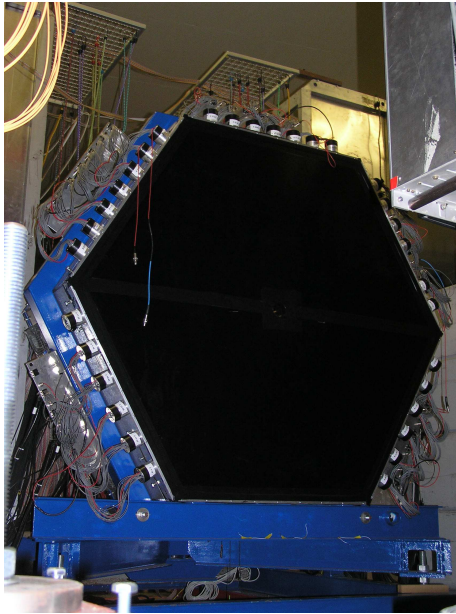


Figure 4.12: TAPS.

4.5.1 BaF₂ Crystals

In its original configuration, TAPS was built in 1990 as a photon and neutral meson detector for use with MAMI-B, at GANIL and in the SIS-facility experiments at GSI, Darmstadt. Its geometrical versatility as an end-plane hodoscope has allowed it also to be used at CERN and with the Crystal Barrel in Bonn.

For this experiment, it was reconfigured as an hexagonal wall comprising 384 BaF_2 crystals, placed 1.5 m downstream of the CB [66]. These crystals are hexagonal bars of length 250 mm ($12 X_0$) with a cylindrical end-part of radius 29.5 mm, as depicted in figure 4.13. The optical isolation of each is ensured by wrapping in eight layers of $30 \mu\text{m}$ PTFE and one layer of $15 \mu\text{m}$ -thick aluminium foil. They are connected, via silicon grease, each to an individual Hamamatsu R2059-001 PMT. Further light-proofing and mechanical stability is provided by containing the crystal and PMT base in shrinking tube. Cylindrical magnetic shields surround the PMT and cylindrical section of each crystal, to give protection from stray fields of up to ~ 0.02 T.

TAPS has angular resolutions of $< 1^\circ$ in θ and $< \frac{1}{R}$ rad in ϕ , where R is the distance in cm from the centre of TAPS to the point on the surface of TAPS corresponding to θ [66]. Its energy resolution is $\frac{\sigma}{E} = \frac{3.7\%}{E_\gamma(\text{GeV})^{\frac{1}{4}}}$ [91].

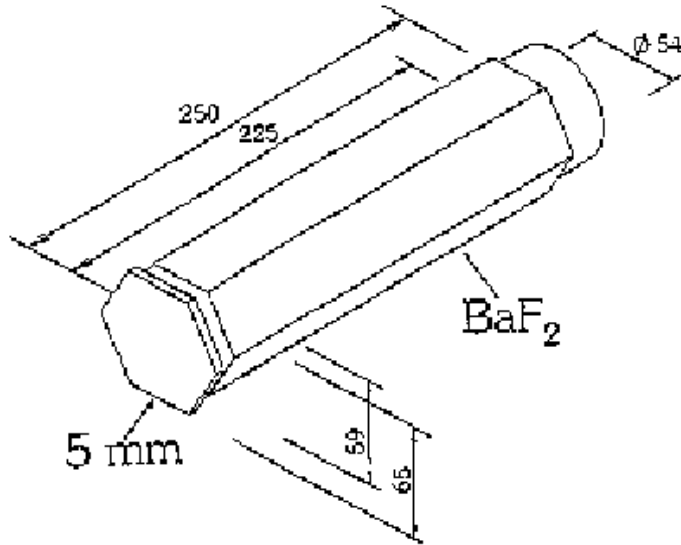


Figure 4.13: An hexagonal BaF_2 crystal from TAPS, adjoined by a 5 mm-thick veto counter [85].

BaF_2 has a high detection efficiency in spite of its low luminescent yield relative to $NaI(Tl)$ [85]. It has fast scintillation light components at $\lambda = 195$ nm and 220 nm with a decay time of ~ 0.6 ns and a slow component at 310 nm with decay time ~ 620 ns [92].

Time-of-flight (ToF) measurements and pulse-shape analysis (PSA) can be used in particle identification. Very precise timing ($\sigma \simeq 200$ ps) is obtained from the fast scintillation component, facilitating discrimination between relativistic photons, electrons and pions and slower protons and neutrons via ToF. PSA uses the ratio of scintillation intensities deposited in the fast components to that in the total light output, since this decreases with increasing ionisation density (decreasing velocity) of the particles [92].

4.5.2 Veto Counters

Charged particle discrimination can also be achieved using the TAPS veto detectors, shown in figure 4.13. These are 5 mm-thick hexagonal plastic scintillators, placed one in front of each crystal for the identification of charged particles via the $\Delta E - E$ method, analogous to that used for the PID. The vetos are composed of

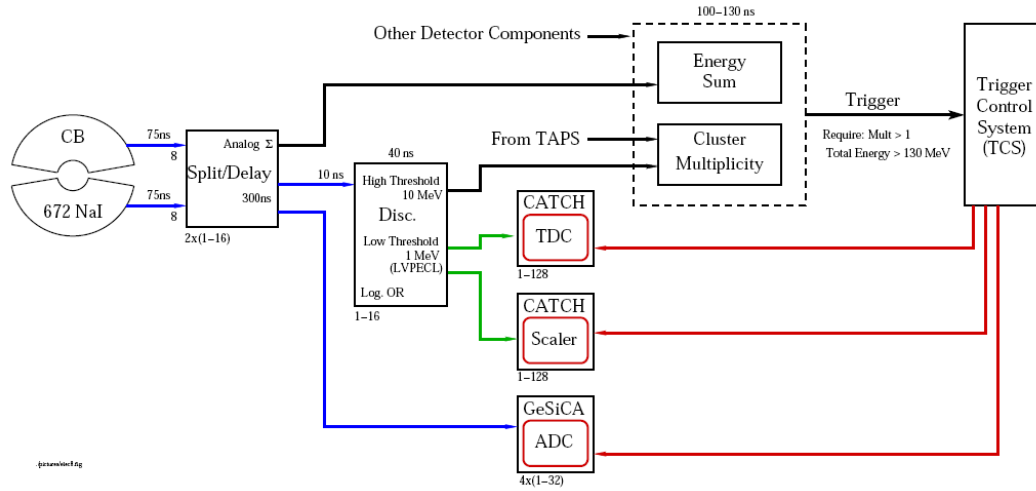


Figure 4.14: Schematic of the Crystal Ball read-out electronics [90].

EJ204 plastic, read out via WLS-fibre BCF-92 [93]. Approximately 30 cm of fibre is embedded, in two turns, into a 3 mm deep groove in each scintillator using silicon rubber. These fibres are connected, via coaxial contacts, to 4×4 -anode Hamamatsu 6568 photomultipliers. Each counter is light-proofed by wrapping in teflon and aluminium reflector foil surrounded by black tape. Thin plastic tubing contains each 90 cm-long fibre. Pulse height and timing information is obtained.

4.6 Data Acquisition

4.6.1 Crystal Ball Electronics

The CB PMTs are attached to a split-delay module. These signals are sent to ADCs and, via a discriminator, to TDCs and the trigger. GeSiCA and CATCH electronics read these, then connect via VMEbus to 2 powerPCs [90]. A simplified schematic of the CB front-end electronics is given in figure 4.14.

ADCs

The ADCs (i-SADC 108032) sample pulse wave forms at 40 MHz (with a maximum rate of 80 MHz). The full digitised pulse shape can be read into the data stream, but this volume of data would overload the DAQ system. Therefore samples are

integrated over three consecutive time intervals with respect to the experimental trigger. These are the pedestal, signal and tail region of the pulse. The pedestal is mainly DC offset in the SADC — which allows overshoots to be recorded — with contributions also from “afterglow” in the *NaI* and from electronic noise. This is dynamically subtracted from the signals, improving energy resolution. The tail region allows checking for pile-up effects.

TDCs

A PM98 dual threshold discriminator provides a time pick-off from the *NaI* signal [82]. Individual channel thresholds, programmed to 5 mV (~ 2 MeV), feed logic signals to multi-hit TDCs. An OR signal from the 16 channels of the discriminator module feed the trigger system. The TDCs are identical to those used on the tagger — see section 3.5.

4.6.2 PID Electronics

The PID PMTs are connected to a $10\times$ amplifier from which they fan out to a Fast Integrating ADC (FIADC-64) [94] and to a LeCroy 4413 discriminator module. The discriminator outputs are passed to CATCH TDCs and to the trigger system, the latter via a LeCroy CAMAC logic unit which combines the signals into a logical OR.

4.6.3 TAPS Electronics

TAPS PMTs connect to two leading edge discriminators (LEDs), a constant fraction discriminator (CFD), a time-to-amplitude converter (TAC) and four charge-to-amplitude converters (QACs) [95]. These are integrated onto a single board. Four boards are contained in a single-width VMEbus module. The LEDs facilitate triggering. The CFDs provide walk-corrected time pick-off pulses, used to provide TDC start signals. The fast and slow scintillation components are measured separately, with both high and low gain, by the QACs. The CFD pulse gates the QACs for the fast scintillation components, which are integrated for only ~ 40 ns. The slow components are integrated for ~ 200 ns. This enables PSA.

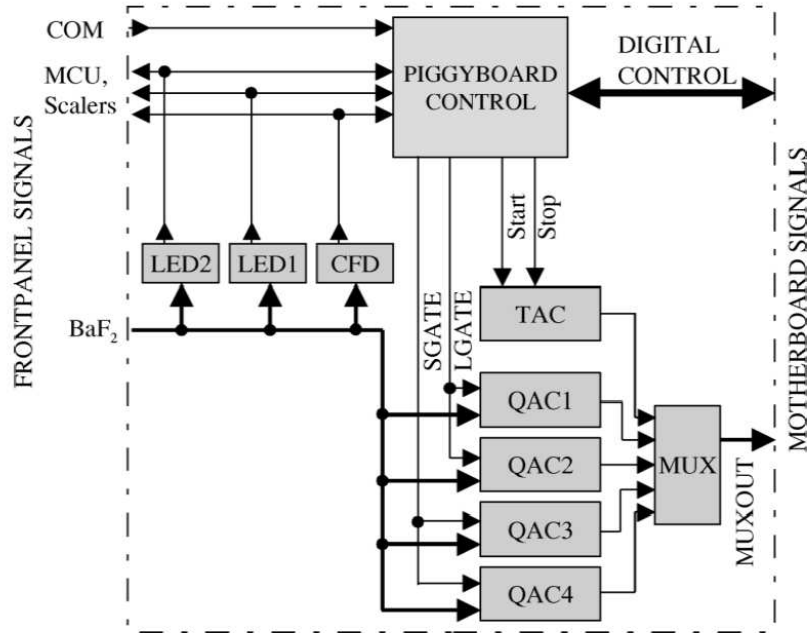


Figure 4.15: Schematic of TAPS read-out electronics [95].

4.6.4 Triggers

To limit dead time in the DAQ electronics, on-line triggers ensure that only relevant events are recorded. Trigger circuit diagrams are shown in figures 4.16 and 4.17. For this experiment, there were two main requirements [66]. Firstly, that the sum of all ADC amplitudes from the CB exceeded a voltage threshold corresponding to 320 MeV of deposited energy. Secondly, that the number of CB clusters detected simultaneously exceeded one, referred to as a “multiplicity two” (M2+) trigger. Such a cluster was defined as comprising an OR of 16 adjacent crystals, with >30 MeV registered in at least one crystal.

4.6.5 DAQ Control

The CB and Tagger are each read out by a VME powerPC CPU. TAPS has a DAQ system based on 8 i386 processors [97]. These three streams are sent to a multi-processor PC which combines them, stores this combined stream on disk and provides on-line analysis and display of data, allowing monitoring of data quality and synchronisation. The separate streams can also be stored for diagnostic purposes.

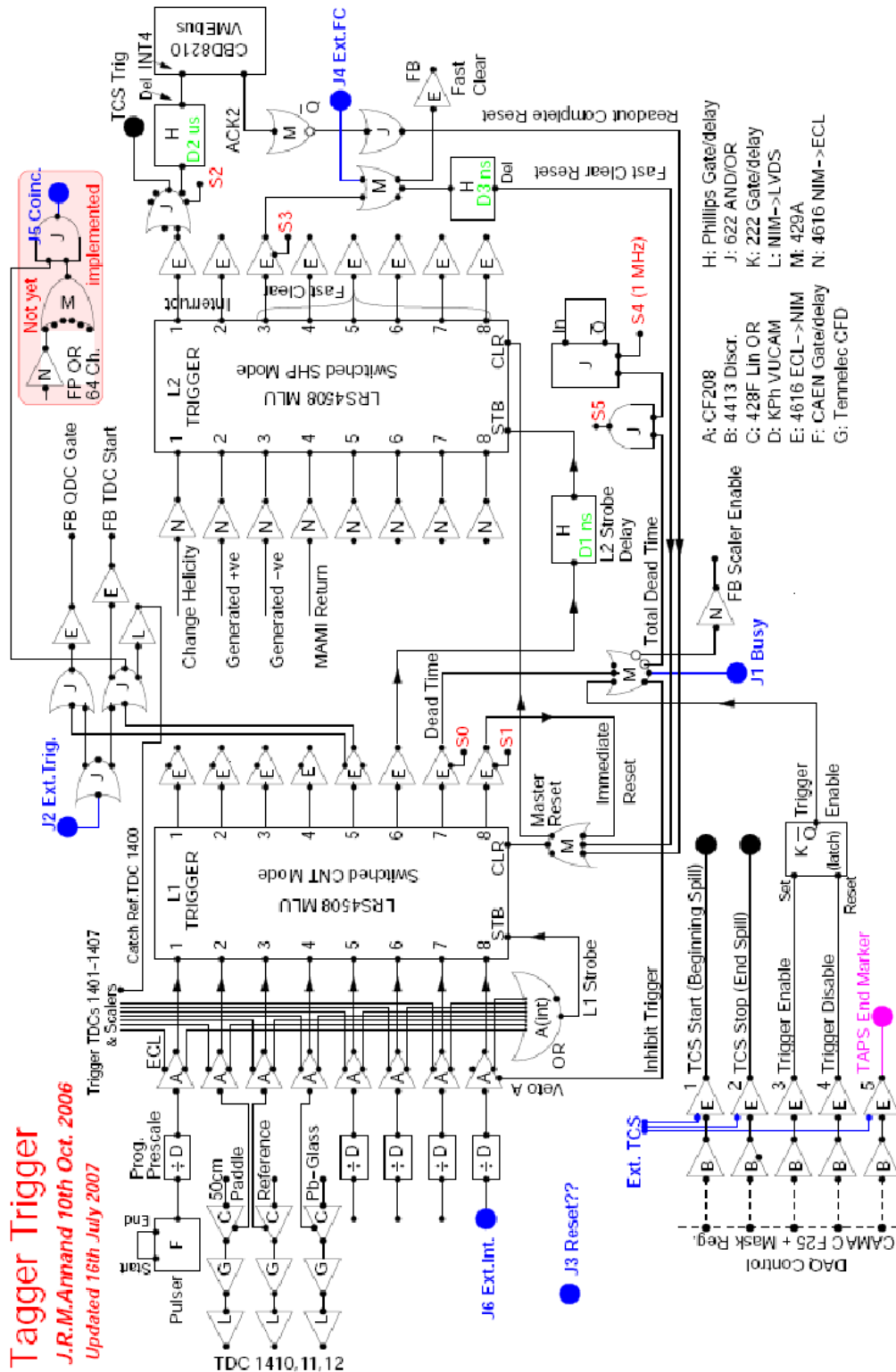


Figure 4.16: Tagger triggering diagram [71].

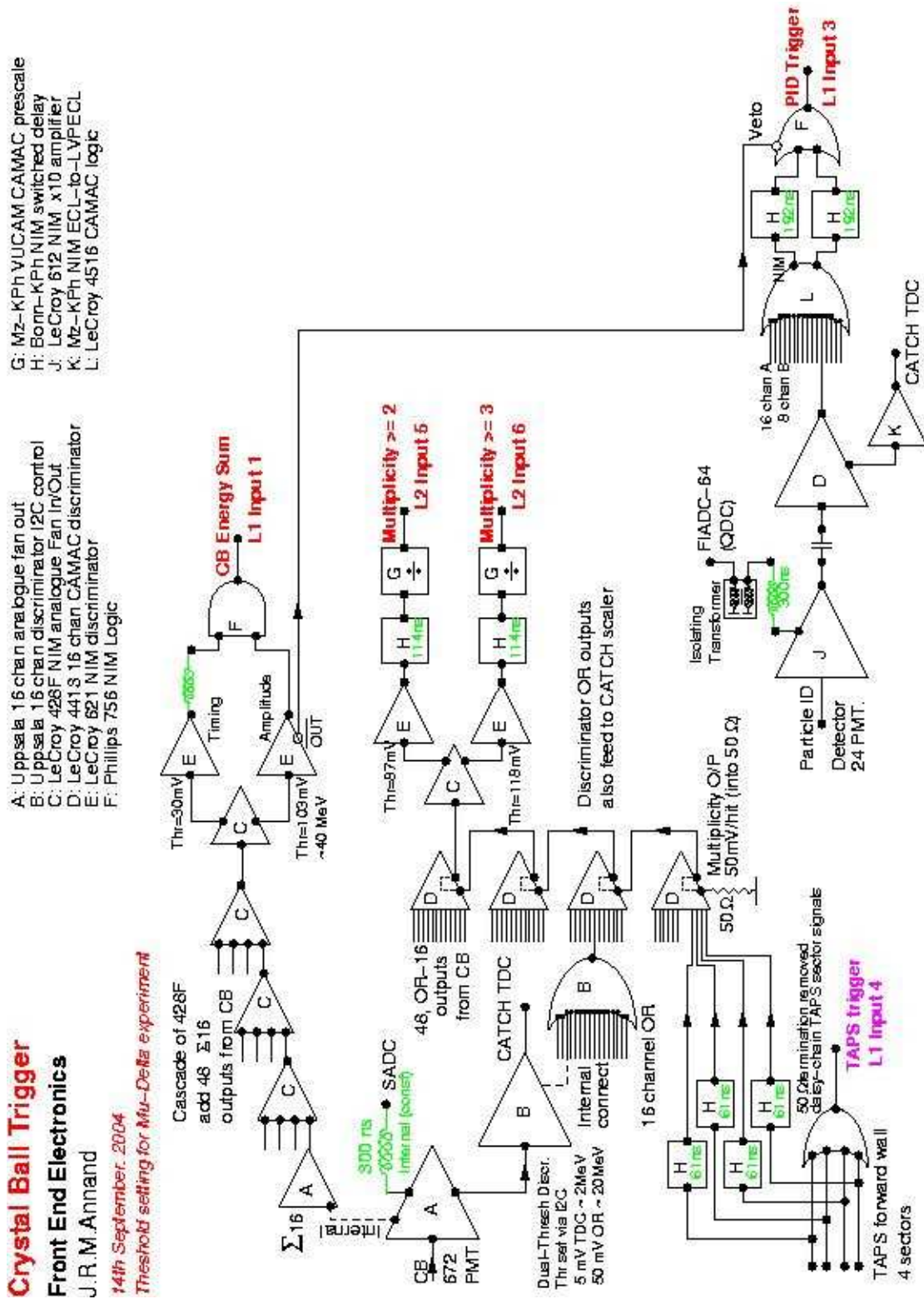


Figure 4.17: Crystal Ball triggering diagram [96].

Chapter 5

Data Analysis

For each event occurring, the detector system gave time in units of TDC channel, energy in units of QDC channel, position in terms of crystal number and charge information. This data was converted to time in nanoseconds, energy in MeV, and azimuthal (ϕ) and polar (θ) angles in radians. These calibrated values, in combination with a clustering pattern recognition algorithm, were used in the analysis package *AcquRoot* [98] to determine the 4-momentum and Particle Data Group (PDG) ID number of each particle in every event. η mesons were then selected by cutting on the η mass within 2γ and 6γ invariant spectra, before $\gamma p \rightarrow \eta p$ events were isolated by a further cut on the proton missing mass. Analogous cuts were applied to simulated data in order to determine the acceptance of the detectors and analysis, before the observed η yield was corrected to produce differential cross-sections. TAPS data were omitted from this analysis due to difficulties with the calibration of this device, which were not completely resolved within the time scale of this work.

5.1 Detector Calibration

5.1.1 Tagger

The energy calibration of the tagger is described in section 3.7.

5.1.2 Crystal Ball

The Crystal Ball energy calibration for 2007 data [99] followed the method previously employed in 2004, as detailed in [100]. PMT gain alignment for individual CB crystals was performed using the 4.4 MeV γ -decay of an *AmBe* source. This facilitated the setting of experimental hardware thresholds.

A calibration for higher energy photons, in the range typical of meson decay, was performed using the kinematically over-determined reaction $\gamma p \rightarrow \pi^0 p$. The energy of the π^0 was obtained using two methods: by direct measurement of energy deposited by the decay photons in the CB and by reconstruction using the incident photon energy and π^0 emission angle, θ_{π^0} . Photon energy is typically deposited over a cluster of neighbouring crystals, as described in section 4.4.1. Only events in which $\geq 70\%$ of E_γ was deposited in the central crystal of a cluster were considered. The gain of each crystal, in MeV-per-channel, was then adjusted by iterative comparison between the two methods until convergence was reached.

5.1.3 PID

The energy calibration method developed for the pre-upgrade PID detector [82, 101] was adapted for the new PID [102]. Plots of energy deposited in the CB, E , versus energy deposited in the PID, ΔE , as shown on the left hand side of figure 5.1, were produced for both experimental data and a Geant4 Monte Carlo simulation, described in section 5.7.2. These plots display separate mass-dependent curves for protons and charged pions.

For the simulated data, projections of the PID ΔE were taken over 50 intervals in CB E . Each of these displayed two separate peaks corresponding to the proton and pion ridges. Gaussians were fitted to these, as shown on the right hand side of figure 5.1. The position of the MC proton peak, in MeV, was plotted against that of the uncalibrated experimental data, in units of QDC channel, for each E bin. A straight line was fitted to these to give the high energy calibration. Low energy data points were obtained using the minimum ionising pion peak in the ΔE projections. This process was repeated for each of the 24 PID scintillators.

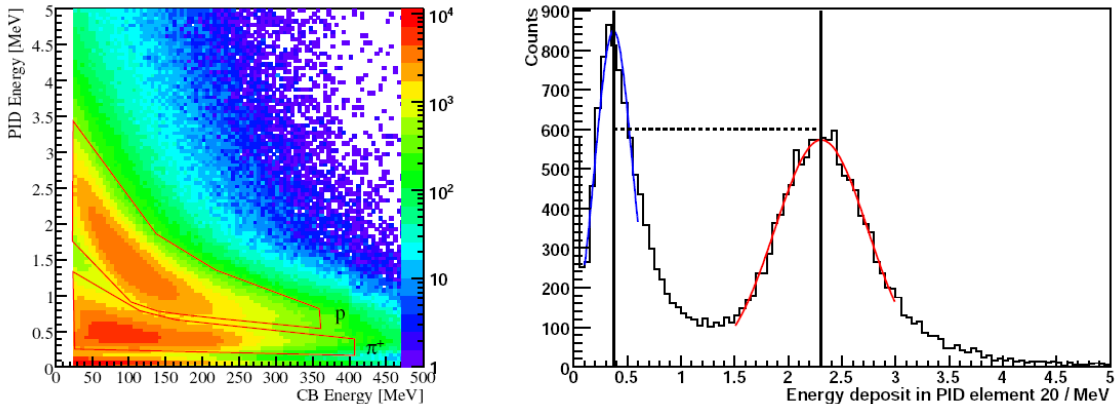


Figure 5.1: PID calibration plots. Left: simulated $E - \Delta E$ curves for the proton and charged pion. Right: projection of this between 38 and 42 MeV and Gaussian fits to this [85].

5.2 Event Reconstruction and Identification

5.2.1 Random Subtraction

In addition to the recoiling Bremsstrahlung electron whose photon triggered a given event — the “prompt” count — the tagger detected random-coincidence background electrons in the same time region — the “random” counts. These came from electrons for which the Bremsstrahlung photon was either stopped by the collimator or passed through the collimator but failed to interact with the target.

This background was subtracted using timing relative to the experimental trigger. For prompt events, this time was equal to that taken by the photon to travel from the radiator to the target plus that for the reaction products to make the trigger — the sum of flight time from target to detector, cable delays, walk and jitter in the electronics [103] — so was almost constant. These events were seen as a peak on the timing spectrum, as shown in figure 5.2. This is an OR of all tagger channels, the prompt peak of each channel having been aligned to a common point. The peak width is due to jitter and the small variations in flight time. Random events, having no such structured timing, produced an approximately flat background. To account for the random background beneath the prompt peak, one sample was taken from the prompt region and two from the random regions either side of the peak, before

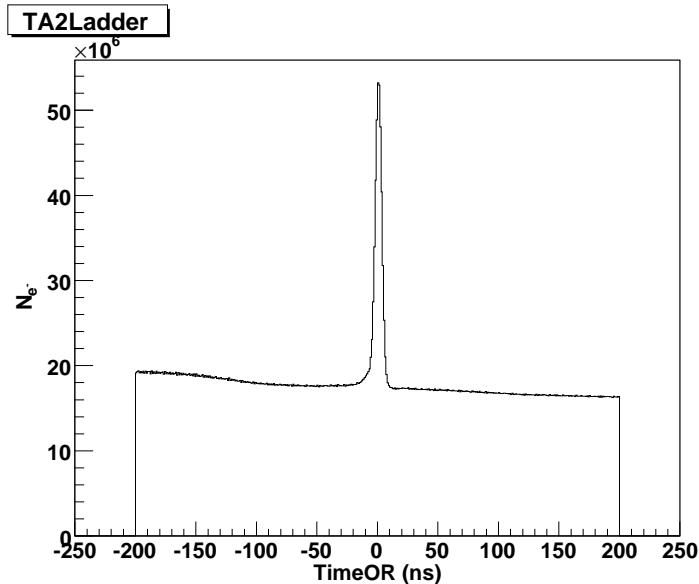


Figure 5.2: Time OR of tagger TDC hits.

a weighted subtraction was performed. This prompt / random discrimination was used to gate all distributions relying on tagger hits, for example missing masses, as used in section 5.6.

5.2.2 Event Reconstruction

A photon incident in the CB instigates an electromagnetic shower with $\sim 98\%$ of its energy deposited in 13 adjacent crystals [83]. Within the *AcquRoot* analysis code, a clustering algorithm selected the crystal in which the greatest amount of energy was deposited, then summed energies for this and any of the 12 neighbouring crystals which fired, see figure 5.3. Shower clusters containing < 15 MeV were rejected. The centre of an accepted shower was determined using the sum of each crystal's position within the cluster, weighted by the square root of the energy deposited in each. This gave hit position and hence angular information for each shower.

5.2.3 Particle Identification

A hit in the PID exceeding a threshold of ~ 0.1 MeV [104] indicates that a particle is charged. In the CB, particles for which no PID hit is detected are assumed neutral and so by default designated as photons, with the option to revise this designation at

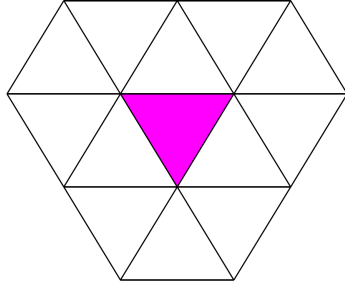


Figure 5.3: A cluster within the CB [85]. Each triangle represents the inward face of one NaI crystal, with the shaded triangle containing the largest energy deposit.

a later stage. For charged particles with correlated azimuthal angle, ϕ , in the CB and PID, polygon cuts — as depicted on the left hand side of figure 5.1 — are defined for each PID element. Particles with $(E, \Delta E)$ falling in the upper polygon are taken to be protons and assigned four-vectors using kinetic energy equal to that deposited in the CB, angle as gleaned from the clustering algorithm and mass of $938.27 \text{ MeV} \cdot \text{c}^{-2}$. Those particles lying inside the lower polygon are treated likewise, but are assumed to be charged pions with mass set to the π^+ value of $139.57 \text{ MeV} \cdot \text{c}^{-2}$.

Since the CB and PID calibrations were optimised respectively for photons and pions or protons and pions — as opposed to η mesons — scaling factors were applied to the NaI MeV-per-channel factor. Energy missed by the clustering algorithm was also compensated for thus. These factors were set by observing the 2γ and 6γ invariant mass spectra for events in which all η decay photons were detected by the CB and adjusting the CB gain factor until the η peak had its maximum at 547 MeV. This factor was 1.030 for 2γ and 1.047 for 6γ events in the CB.

5.3 η Photoproduction Differential Cross-Sections

The cross-section of a reaction is a measure of the probability of its occurrence quoted in units of area – conventionally barns, b, in experimental nuclear physics, where $1 \text{ b} = 10^{-28} \text{ m}^2$. The differential cross-section with respect to solid angle, $\frac{d\sigma}{d\Omega}$, quantifies the probability of the chosen reaction producing a given particle, within a specific angular bin for a certain range of incident photon energy. For η

photoproduction, this is calculated as follows in each energy bin [58]:

$$\frac{d\sigma}{d\Omega} = \frac{N_{\eta \rightarrow n\gamma\gamma}}{A_{\eta \rightarrow n\gamma\gamma} \cdot N_\gamma \rho_t \cdot \Delta\Omega \cdot \frac{\Gamma_{\eta \rightarrow n\gamma\gamma}}{\Gamma_{total}}}, \quad (5.1)$$

where:

- ρ_t = effective target thickness
- $N_{\eta \rightarrow n\gamma\gamma}$ = number of reconstructed events in an $(E_\gamma, \cos \theta_\eta^*)$ bin
- $A_{\eta \rightarrow n\gamma\gamma}$ = acceptance for an $(E_\gamma, \cos \theta_\eta^*)$ bin
- N_γ = number of incident photons in an E_γ bin
- $\Delta\Omega$ = $2\pi\Delta \cos \theta_\eta^*$: solid-angle interval for a $\cos \theta_\eta^*$ bin
- $\frac{\Gamma_{\eta \rightarrow n\gamma\gamma}}{\Gamma_{total}}$ = decay branching ratio
- n_γ = 2 or 6, for $\eta \rightarrow 2\gamma$ or $\eta \rightarrow 3\pi^0 \rightarrow 6\gamma$ respectively.

20 $\cos \theta_\eta^*$ bins were chosen for the 2γ decay mode, giving a solid angle interval of $\Delta\Omega = 0.2\pi$. The high statistics of this data set — especially in the threshold region — may allow finer binning to be used for future publication of this analysis. 10 angular bins were used for the 6γ decay mode due to the lower statistics obtained, giving $\Delta\Omega = 0.4\pi$. Branching ratios were taken from the PDG [7], as listed in section 5.4.1. Effective target thickness was calculated from known properties of liquid hydrogen and dimensions of the target cell, given in section 5.4.2. Photon flux was measured experimentally as described in section 5.5. The main components of the analysis detailed herein were extraction of η yield, Y_η , and calculation of combined detector and analytical acceptance, described in sections 5.6 and 5.7 respectively.

5.4 Constant Factors

5.4.1 Branching Ratios

The branching ratios of the decays of interest are [7]:

$$\begin{aligned} \eta \rightarrow 2\gamma & : (39.39 \pm 0.24) \% \\ \eta \rightarrow 3\pi^0 & : (32.52 \pm 0.26) \% \\ \pi^0 \rightarrow 2\gamma & : (98.798 \pm 0.032) \% \end{aligned}$$

rendering the $\eta \rightarrow 3\pi^0 \rightarrow 6\gamma$ branching ratio equal to $(31.36 \pm 0.25) \%$.

5.4.2 Effective Target Thickness

Effective target thickness is calculated thus [58]:

$$\rho_t = 2 \frac{\rho(H_2) N_A L}{M_{mol}(H_2)}, \quad (5.2)$$

where:

$$\begin{aligned} \rho(H_2) &= \text{density of liquid hydrogen} &= 0.0708 \text{ g}\cdot\text{cm}^{-3} \\ N_A &= \text{Avogadro number} &= 6.022 \times 10^{23} \text{ mol}^{-1} \\ L &= \text{target length [80]} &= (4.76 \pm 0.03) \text{ cm} \\ M_{mol}(H_2) &= \text{molar mass of liquid hydrogen} &= 2.01588 \text{ g}\cdot\text{mol}^{-1} \end{aligned}$$

and the factor of 2 accounts for hydrogen being diatomic. This gives:

$$\rho_t = (2.013 \pm 0.013) \times 10^{-7} \mu\text{b}^{-1}$$

5.5 Photon Flux

The total number of electrons hitting the tagger focal plane detector (N_{e^-}), as shown in the top left of figure 5.4, is measured by scalars, one connected to each tagger channel. The overall shape of this plot corresponds to the $\sim \frac{1}{E_\gamma}$ Bremsstrahlung distribution. The large spike in channels 27–28 and smaller peak in channel 152 are due to noise in their respective read-out cables. The dips, most notably around channel 188 are due either to poor connections, to discriminator thresholds being too high or to PMT HV supplies being too low. These thresholds and HV supplies were reset before subsequent experiments. The replacement of the read-out cables with more robust co-axial cables was made in October 2009. This eliminated both noise and loose connections.

The proportion of photons reaching the target after collimation which correspond to these incident electrons, "tagging efficiency" (ϵ_{tagg}), is detailed in section 3.6 and displayed in the top right of figure 5.4. Large dips appear in the noisy channels noted above and in channel 189.

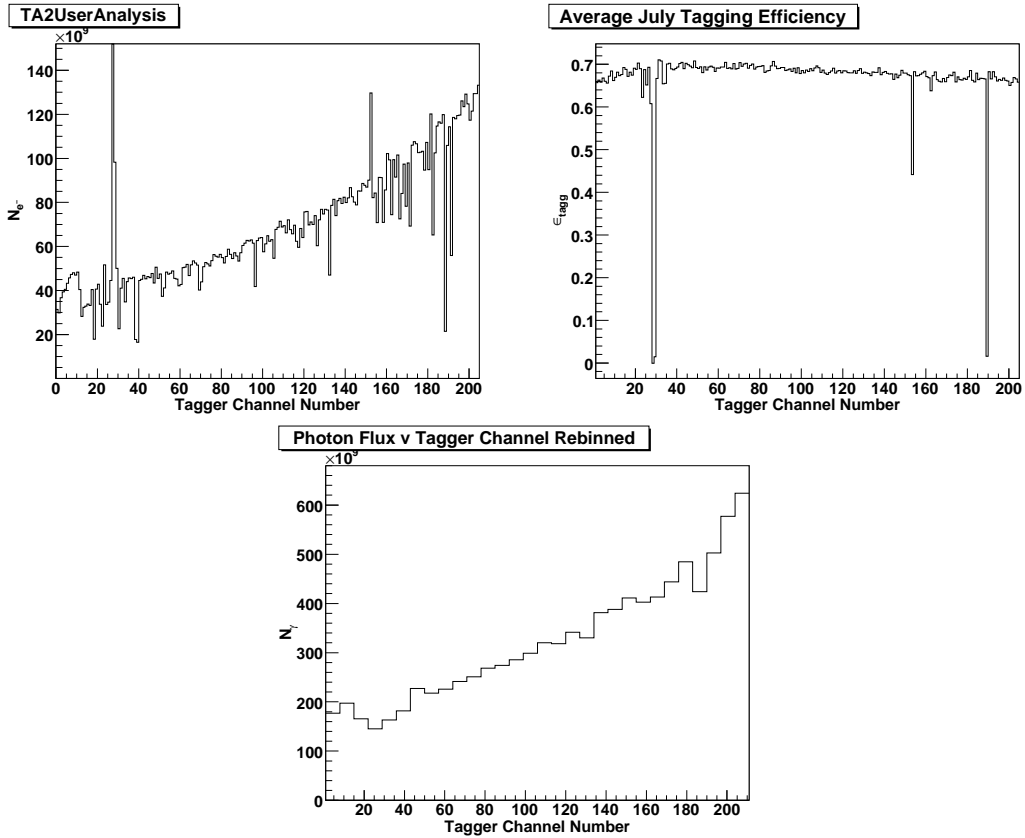


Figure 5.4: Top left: Scaler counts. Top right: Average tagging efficiency measured over the July 2007 run. Bottom: Photon flux.

The product of these gives the number of photons incident on the target, N_γ , for each tagger channel:

$$N_\gamma = N_{e^-} \cdot \varepsilon_{tagg} \quad (5.3)$$

This is displayed in the bottom of figure 5.4, re-binned as described in section 5.6.

The peaks and troughs visible in photon flux and tagging efficiency, respectively, in channels 27–28 and 152 cancel one another out. However, the dip in ε_{tagg} at channel 189, combined with several low scaler channels, result in a reduction in calculated photon flux in this region. Scaler dips will not affect the cross-section determination, since measurements of η yield and photon flux will be reduced equally, but the significant drops in ε_{tagg} are indicative of inaccurate readout and will cause unreliable cross-section determination.

Tagger scalers were intrinsically dead-time corrected, while the CB read-out was inhibited by the logical OR of busy signals for the whole detector system [71]. A

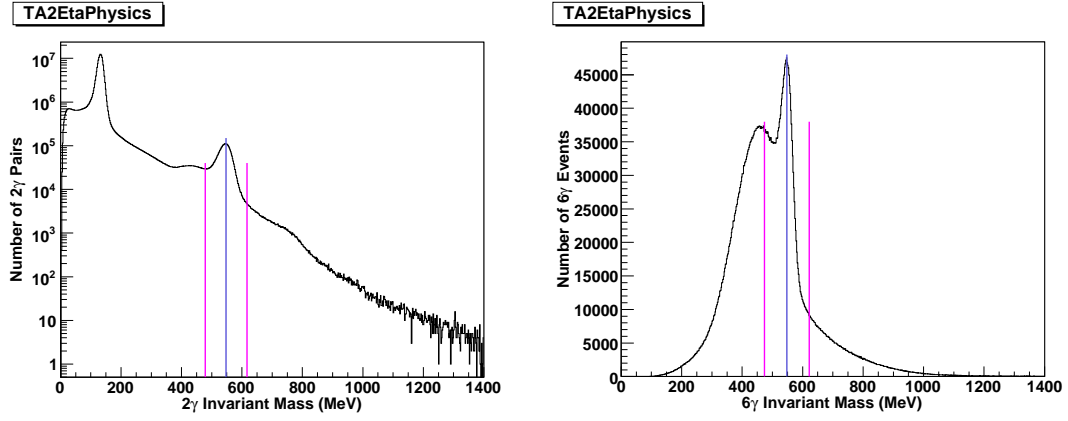


Figure 5.5: Invariant mass distributions of 2γ pairs (left) and 6γ events (right). Blue and magenta lines represent, respectively, the η invariant mass and cut ranges.

correction had therefore to be applied to tagger scalars to account for CB dead-time, as follows:

$$N_{e'} = N_e \cdot \frac{\Gamma_{tot}}{\Gamma_{tagg}} \quad (5.4)$$

where $N_{e'}$ is corrected electron flux, N_e is electron flux recorded by the tagger scalars, Γ_{tot} is the total system live-time fraction and Γ_{tagg} is the tagger live-time fraction. These fractions were obtained using the ratio of counts from a free-running pulser to those from pulsers gated by the respective busy signals. Values of $\Gamma_{tot} = 0.652$ and $\Gamma_{tagg} = 0.794$ were found, giving a correction factor of 0.821.

5.6 Yield Extraction

5.6.1 Event Selection

In this $\gamma p \rightarrow \eta p$ analysis, events were considered in which either 2 or 6 photons were detected simultaneously. For 2γ events, the 4-momenta of the photon pair were summed. From this, the invariant mass was calculated, as displayed in figure 5.5. Each 2γ invariant mass was compared to the PDG mass of the η , $m_\eta = 547.51$ MeV [7]. A difference of under 69 MeV was a necessary condition for acceptance as an $\eta \rightarrow 2\gamma$ event, with 69 MeV corresponding to 3σ when fitting a Gaussian to the $(2\gamma)_\eta$ peak.

For each 6γ event, there were 15 possible photon pairs. The combined 4-

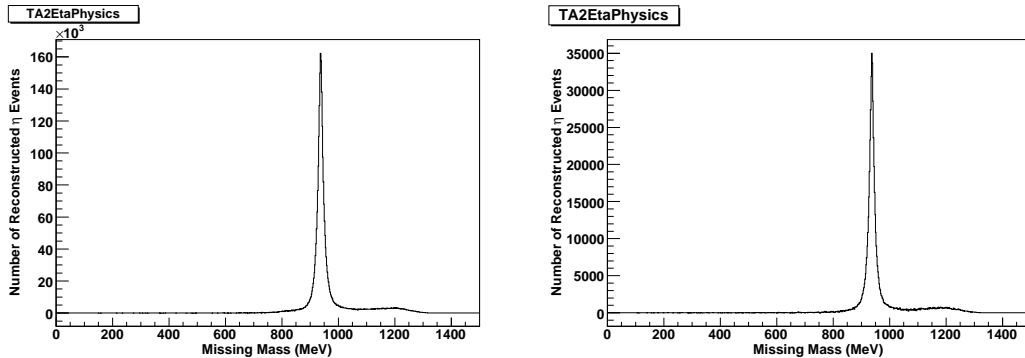


Figure 5.6: m_{miss} (random subtracted) for all accepted $\eta \rightarrow 2\gamma$ (left) and $\eta \rightarrow 6\gamma$ (right) events with m_η set to the PDG value of 547.51 MeV.

momentum and hence invariant mass of each pair was calculated and subtracted from the PDG π^0 mass, $m_{\pi^0} = 134.98$ MeV. These mass differences were sorted into ascending order for analysis. Starting from the lowest mass difference, each photon pair whose mass fell within 30 MeV of m_{π^0} , was accepted as a $\pi^0 \rightarrow 2\gamma$ event, unless either photon had been previously assigned to a meson. From the 6γ events, any originating from three such π^0 decays were selected. The three π^0 4-momenta were summed, so that the total invariant mass could be tested for compatibility with m_η . A difference of under 74 MeV was a necessary condition for acceptance as an $\eta \rightarrow 3\pi^0 \rightarrow 6\gamma$ event. Again, these 30 and 74 MeV cuts corresponded to 3σ of a Gaussian fit to the $(2\gamma)_{\pi^0}$ and $(6\gamma)_\eta$ invariant mass peaks.

For each accepted 2γ or 6γ event, the particle mass was set to be 547.51 MeV. Missing 4-momentum was then calculated, defined thus:

$$p_{miss} = p_{target} + p_{beam} - p_\eta \quad (5.5)$$

From this, missing mass, m_{miss} , was calculated. The resulting plot, see figure 5.6, shows a peak around the proton mass of 938.27 MeV. The width of this peak results from the finite energy resolution of the detectors. Missing mass was used because the efficiency of proton detection is much lower than that for photons in the CB and TAPS. Protons often lack sufficient kinetic energy to reach the detectors since the incident photon energy range covered by this experiment is in the region of the η -production threshold, resulting in only a fraction of the protons produced being detected.

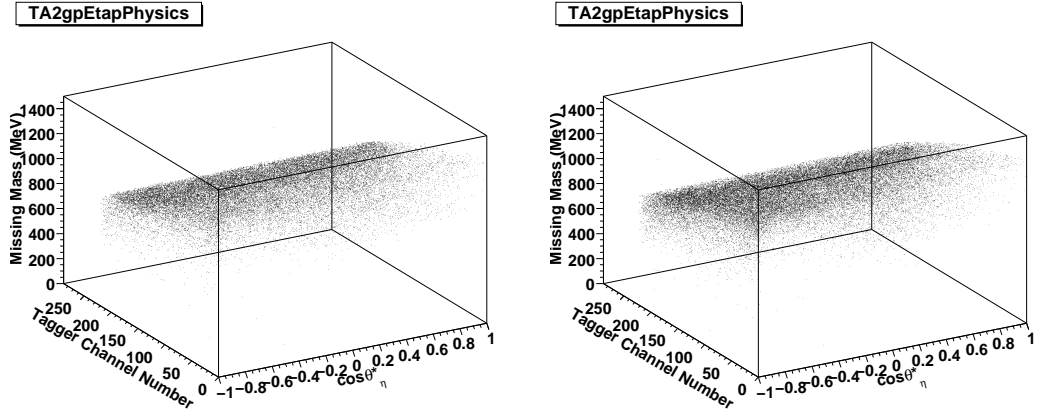


Figure 5.7: m_{miss} against T_{ch} against $\cos \theta_\eta^*$ for 2γ events passing the invariant mass cut. Left: prompt events. Right: random events.

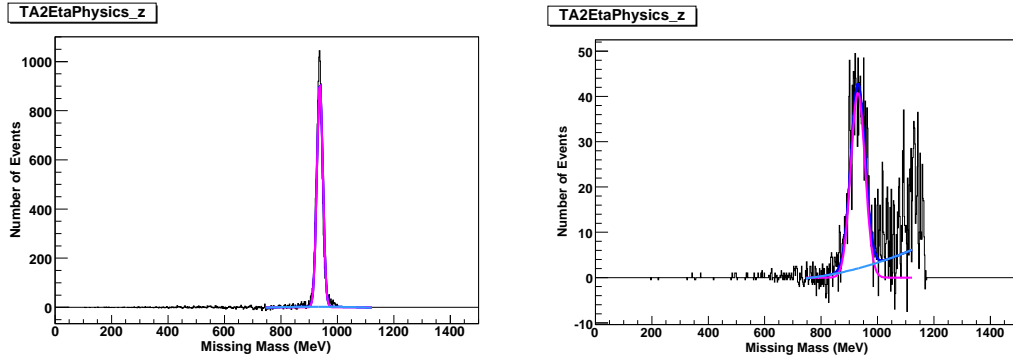


Figure 5.8: m_{miss} fit with the background quadratic in azure, signal Gaussian in magenta and total fit function in blue. Left: ($T_{ch} = 26, \cos \theta_\eta^* = 0.3$). Right: ($T_{ch} = 15, \cos \theta_\eta^* = -0.5$).

The η 4-momentum was also used to calculate the polar production angle in the centre of mass frame, θ_η^* , and the cosine thereof, $\cos \theta_\eta^*$. 3-dimensional histograms were made of m_{miss} versus tagger channel number, T_{ch} , versus $\cos \theta_\eta^*$ for prompt and random counts, for both final states, as shown in figure 5.7. These were used for yield extraction.

5.6.2 Energy and Angular Dependent η Yields

The 3D plots output by *AcquRoot* were analysed using CERN's *Root* package [105]. Projections were taken along the z-axes, returning 1D prompt and random m_{miss} plots for each $(T_{ch}, \cos \theta_\eta^*)$ bin, for both 2γ and 6γ modes. Random subtraction was

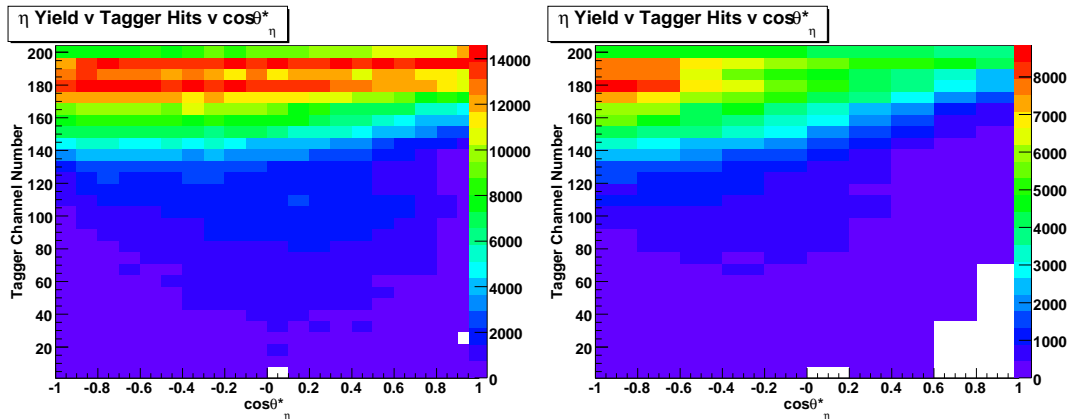


Figure 5.9: η yield as a function of E_γ and $\cos\theta_\eta^*$ with energy in terms of tagger channel number, T_{ch} . T_{ch} is in inverse proportion to E_γ . Left: for the 2γ decay, right: 6γ decay.

then performed (see section 5.2.1). In order to isolate the ηp final state, a fit was made from 744 to 1124 MeV around the proton mass peak in the random subtracted plot.

The background was fitted with a quadratic, ignoring counts in the peak region from 846 to 1004 MeV. A new function was then defined as the sum of this quadratic with a Gaussian and used to fit the full plot. The signal function was taken to be Gaussian with parameters read from the full fitting function. η yield, Y_η , was taken to be the integral of this Gaussian.

Fitting worked extremely well in bins with high statistics, as shown on the left hand side of figure 5.8. For less well populated bins — in which acceptance or cross-section was low, for example at high E_γ (low tagger channel number) and backward angle — the fit came reasonably close to matching the data, as shown on the right hand side of figure 5.8. In certain bins, predominantly at the highest tagger channels where the peaks were most narrow or at the lowest channels where background was greatest, the fitting routine failed. The former were rectified by fitting over a smaller range in m_{miss} . The latter required a wider definition of the peak region to be discounted when fitting the background quadratic. The resulting Y_η values were plotted against T_{ch} versus $\cos\theta_\eta^*$, as shown in figure 5.9.

A total of 2,515,723 $\gamma p \rightarrow \eta p$ events were reconstructed: 2,084,690 from the

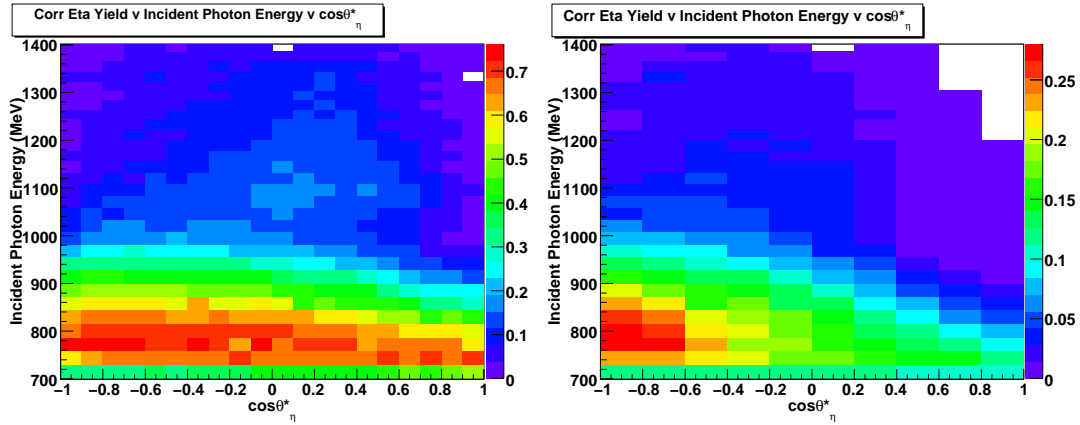


Figure 5.10: Corrected Y_η as a function of E_γ versus $\cos\theta_\eta^*$ for the 2γ (left) and 6γ (right) decay modes.

2γ decay mode and 431,033 from 6γ decay. As expected, yield was greatest at high channel number, above the η production threshold region, $E_\gamma = 707$ MeV, and concentrated at the $S_{11}(1535)$ invariant mass position.

5.6.3 Corrected Yield

Still working in tagger channel space — *ie.* before converting to photon energy space — yield was divided by solid angle interval, branching ratio, effective target thickness and photon flux to produce “corrected yield”.

The tagger energy calibration detailed in section 3.7 was then applied to convert from T_{ch} to E_γ , as shown in figure 5.10, before correction for acceptance was made.

5.7 Acceptance Determination

Simulation of $\gamma p \rightarrow \eta p$ events was performed via an *AcquRoot* event generator before these were passed through an A2-specific Geant4 model, then analysed in a process analogous to that of the experimental data, in order to assess the combined acceptance of the detectors and analysis.

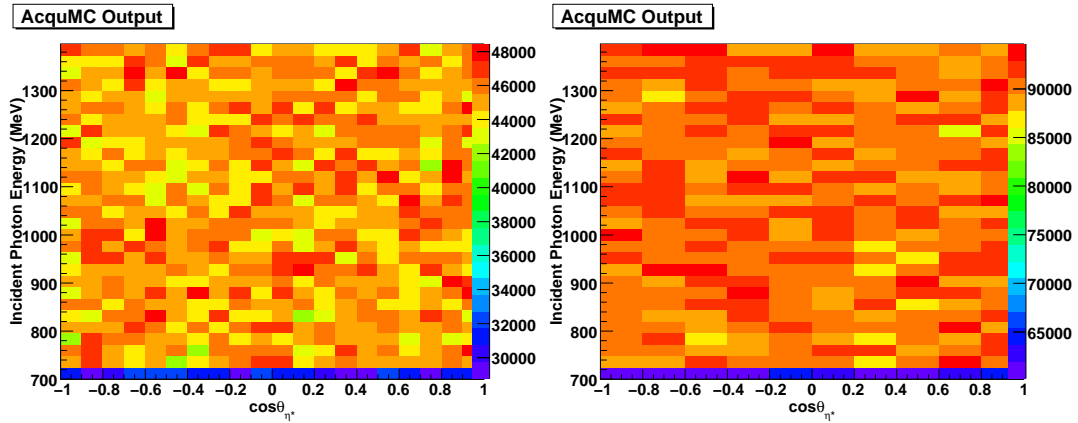


Figure 5.11: Generated η events as a function of E_γ and $\cos\theta_\eta^*$ using a phase space distribution in *AcquMC* for the 2γ (left) and 6γ (right) decay modes.

5.7.1 Event Generation

An event generator called *AcquMC* [98] was used to simulate 30 M events each for the 2γ and 6γ decay modes, with a phase space distribution. Parameters of the target and beam were specified, along with the decay products to be tracked. A uniform E_γ distribution, as opposed to the $\frac{1}{E_\gamma}$ Bremsstrahlung distribution, was employed to improve statistics at high incident photon energies. The E_γ range 700 to 1400 MeV was input to correspond to the experimental energy range. A uniform distribution of η production angles was specified.

A *Root* [105] ntuple was produced, containing 4-momentum components and a PDG index integer specifying particle type, for each reactant and final product — target, beam, proton and 2 or 6 η -decay photons — as well as the co-ordinates of the reaction vertex. Taking this, the η 4-vectors were reconstructed, along with their polar angles in the centre-of-mass and cosines thereof. Generated Y_η was plotted against E_γ versus $\cos\theta_\eta^*$, as shown in figure 5.11.

5.7.2 Experimental Model

The experimental apparatus was modelled in a Geant4-based simulation [106] called *A2* [107]. This model contained the CB, PID and TAPS, as depicted in figure 5.12. The *Root* ntuple produced by *AcquMC* was fed into this. The interaction of each particle with the detectors was simulated, taking account of electromagnetic physics

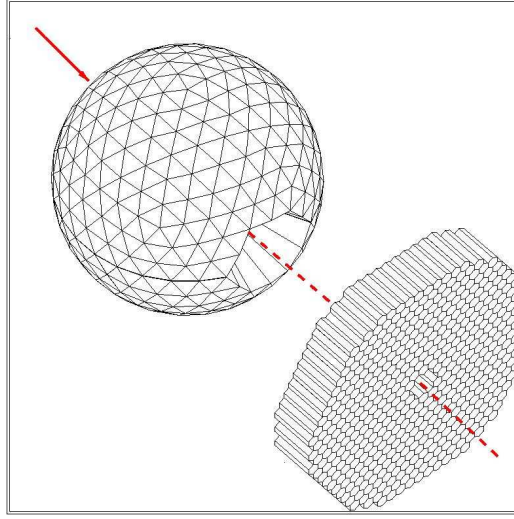


Figure 5.12: *A2* simulation representation of the CB and TAPS detectors [107].

processes as follows:

- Charged particles: multiple scattering, ionisation, Bremsstrahlung, high energy muon processes, annihilation and synchrotron-, Cerenkov- and transition-radiation.
- Photons: Compton scattering, pair production and photo-electric effects.

Hadronic processes were described by a theory-based Binary Cascade model [107].

Simulated signals in detector elements were produced and output to another *Root* ntuple which was analysed in an analogous manner to that employed for the experimental data.

5.7.3 Physics Analysis

The *A2* output file was analysed using *AcquRoot*. Exactly the same physics analysis code was used as for the experimental data, with TAPS again omitted. Detector energy resolution was included to give the η invariant mass peaks the same width as in the experimental data, as shown in figure 5.13.

As for the experimental data, a plot of m_{miss} versus E_γ versus $\cos\theta_\eta^*$ was made, see figure 5.14. Each projected $m_{miss}(E_\gamma, \cos\theta_\eta^*)$ was fitted by a Gaussian which was integrated to give Monte Carlo Y_η as a two dimensional function of E_γ versus $\cos\theta_\eta^*$, shown in figure 5.15.

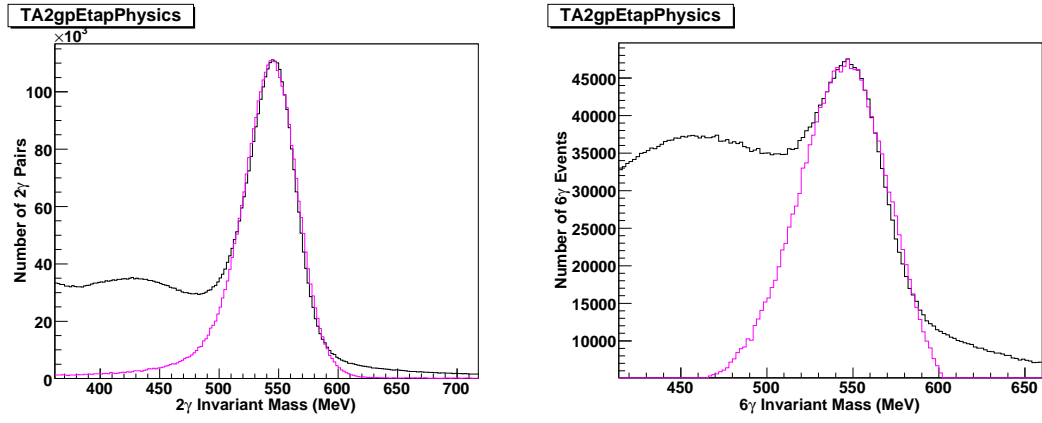


Figure 5.13: η mass peak in the invariant mass of 2γ pairs (left) and 6γ events (right) with experimental data in black, simulation in pink.

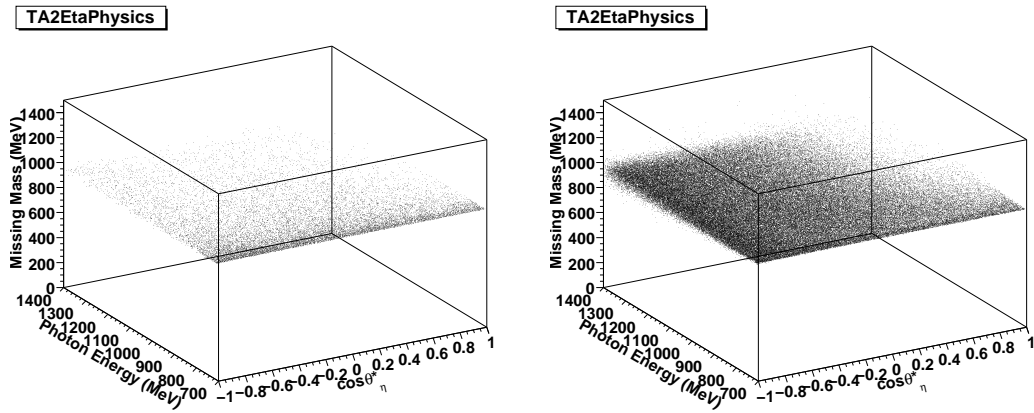


Figure 5.14: Monte Carlo m_{miss} versus E_{γ} against $\cos\theta_{\eta}^*$ from *AcquRoot* analysis. Left: $\eta \rightarrow 2\gamma$, right: $\eta \rightarrow 6\gamma$.

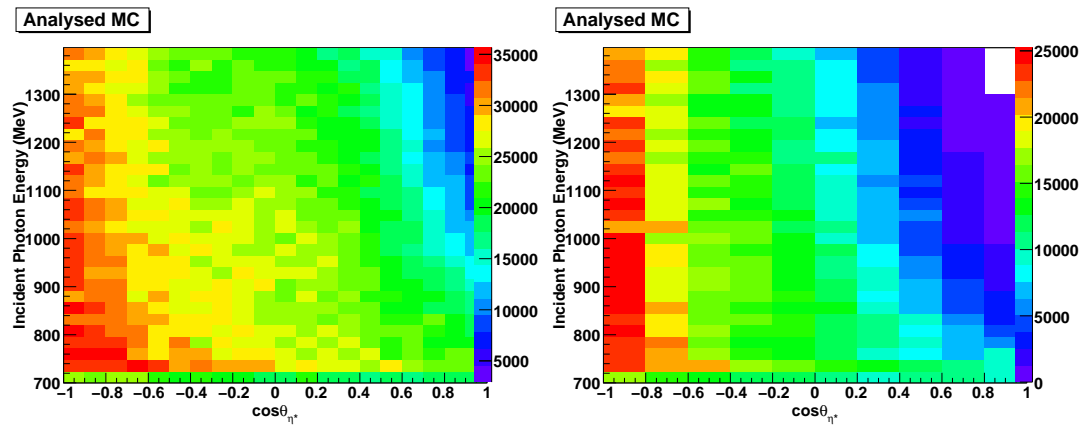


Figure 5.15: Monte Carlo Y_{η} as a function of E_{γ} and $\cos\theta_{\eta}^*$ after full analysis. Left: $\eta \rightarrow 2\gamma$, right: $\eta \rightarrow 6\gamma$.

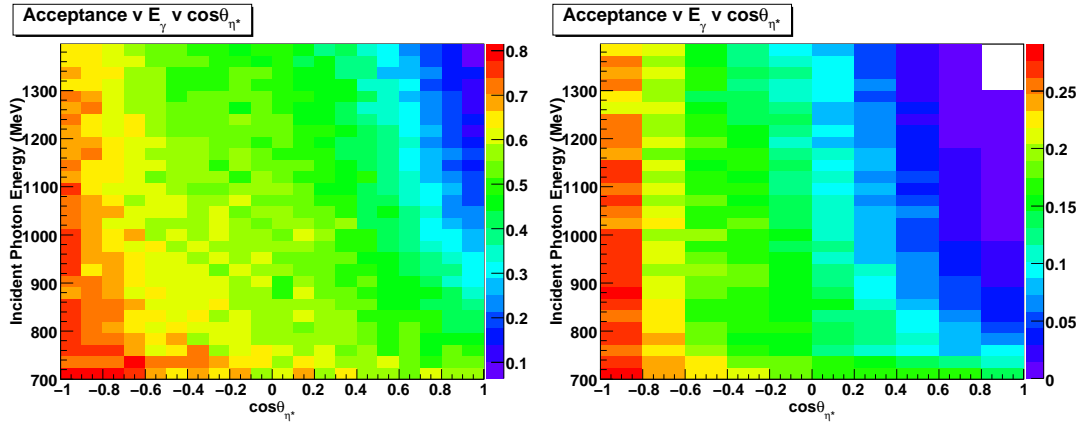


Figure 5.16: Acceptance as a function of E_γ and $\cos \theta_\eta^*$ for 2γ (left) and 6γ (right) decays.

5.7.4 Acceptance Calculation

Acceptance is a measure of the proportion of occurring events which are registered by the detector system and pass all analysis cuts, *ie.* the ratio of measured to actual events. This was calculated by division of the number of events remaining after full analysis — running through *A2*, analysis with *AcquRoot* and Y_η extraction — by those output from the event generator. In order to obtain values for each $(E_\gamma, \cos \theta_\eta^*)$ bin, the respective Y_η versus E_γ versus $\cos \theta_\eta^*$ plots — figures 5.15 and 5.11 — were divided, giving $A_{\eta \rightarrow n\gamma}(E_\gamma, \cos \theta_\eta^*)$ as shown in figure 5.16.

Acceptance is generally of the order of 0.55 for 2γ events. It peaks at 0.82 for $E_\gamma = 718 \text{ MeV}$, $\cos \theta_\eta^* = -1$ then decreases with increasing energy and angular cosine down to 0.06 at $E_\gamma = 1395 \text{ MeV}$, $\cos \theta_\eta^* = 0.9$. For the 6γ decay mode, acceptance is mostly ~ 0.15 . Variation is from 0.29 to 0, following a similar trend to that observed for the 2γ mode. This drop in efficiency at forward angles is expected, due to the exclusion of TAPS data from the analysis.

5.8 2D Differential Cross-Sections

$\frac{d\sigma}{d\Omega}$ as a two-dimensional function of E_γ and $\cos \theta_\eta^*$ is obtained by dividing corrected yield, figure 5.10, by acceptance, figure 5.16. The result is displayed in figure 5.17. Projections of this are taken to create the final results displayed in section 6.1.

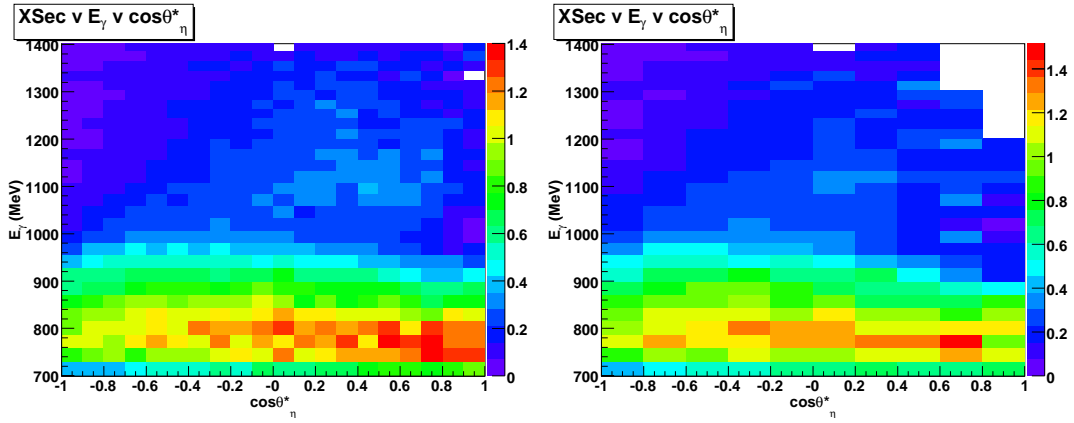


Figure 5.17: $\frac{d\sigma}{d\Omega}$, in $\mu\text{b}/\text{sr}$, as a function of E_γ and $\cos\theta_\eta^*$.

5.9 Error Evaluation

5.9.1 Statistical Uncertainties

Statistical errors in differential cross-sections, as calculated using equation 5.1, arise in three quantities:

- Number of detected η decays, $N_{\eta \rightarrow n_\gamma \gamma}$, for each $(E_\gamma, \cos\theta_\eta^*)$ bin.
- Acceptance, $A_{\eta \rightarrow n_\gamma \gamma}$, for each $(E_\gamma, \cos\theta_\eta^*)$ bin
- Number of incident photons, N_γ , in each E_γ interval.

In each of these, the error in a number of measurements N is equal to \sqrt{N} , so that the fractional error decreases with increasing statistics. For the 2γ decay, η yield varied from 14598 to 22 per bin, giving uncertainties of 0.8 to 21.3%. In the 6γ channel Y_η was between 8844 and 5 with corresponding uncertainties ranging from 1.1 to 44.7%. Uncertainty in acceptance depended on the number of generated events. This was chosen to be 30 million for each decay mode, giving uncertainties of 0.6 to 1.3% for 2γ and 0.6 to 18.2% for 6γ . Photon flux was of the order of 4×10^{11} , giving an uncertainty of $(1.6 \times 10^{-4})\%$. Total statistical errors are included in error bars in figures 6.1 and 6.2 and listed in tables B.3 to B.17 and C.2 to C.16 respectively for the 2γ and 6γ decay modes.

5.9.2 Systematic Uncertainties

The main systematic errors in these differential cross-section measurements arise, again, in yield extraction and acceptance calculation, in addition to those in effective target thickness and background due to interactions in the material containing the liquid hydrogen. There is uncertainty in measurement of the target length due to deformation of the inner window, as described in section 4.3, giving an uncertainty of 0.63%. Variation in the density due to boiling effects is negligible [81]. Empty target data was analysed and found to produce negligible cross-sections relative to the liquid hydrogen data.

Uncertainty in η yield arises from fitting proton peaks in missing mass spectra. This was quantified by comparing a fitting function with a cubic polynomial background to the quadratic used. Signal to background ratio and statistics are highest at low energy and central angles. Here, the discrepancy is small in the 2γ data, as low as 0.011% in some bins and typically remaining under 2% below $E_\gamma = 918$ MeV. As energy increases and Y_η decreases, uncertainties are $\sim 5\%$. For high energies at the most forward and backwards angles, where statistics are poorest and the signal to background ratio is lowest, uncertainties are typically around 12%, peaking at 31%. The 6γ mode shows a similar pattern, ranging from 0.016% to 34%, but typically under 2% at low energy and $\sim 5\%$ at central angles for higher energies.

For the acceptance calculation, uncertainty was assessed by comparing results using a phase space distribution with one dependent on the η photoproduction cross-sections from SAID (see section 2.1). For the 2γ decay mode, an average uncertainty of 4.7% was found. On a bin-by-bin basis, this varied from 0.0031% to 31%, with the largest discrepancies in the high E_γ , forward angle region. For 6γ events, the average uncertainty was higher, at 6.6%, ranging from 0.067% to 44%. Again, this was markedly higher at forward angles for high energies.

Combining these contributions, total systematic uncertainties are typically $\sim 7\%$ for the 2γ mode and $\sim 8\%$ for 6γ data, ranging from $\sim 0.01\%$ or $\sim 0.07\%$ in the threshold region up to $\sim 44\%$ or $\sim 56\%$ in a few high energy, forward angle bins for 2γ and 6γ data, respectively. See figures 6.1 and 6.2 and tables B.3 to B.17 and C.2 to C.16.

Chapter 6

Results and Discussion

This chapter presents differential cross-section measurements for η photoproduction on the proton:

$$\gamma p \rightarrow \eta p$$

in the energy range $707 \leq E_\gamma \leq 1403$ MeV over the full polar angular range, $0 \leq \theta_\eta^* \leq 180^\circ$. The two dominant η decay channels:

$$\eta \rightarrow 2\gamma \quad \text{and} \quad \eta \rightarrow 3\pi^0 \rightarrow 6\gamma$$

have been analysed separately. A comparison of results from these final states is given. Data are also compared to the SAID model and to recent experimental results from the GRAAL collaboration. Through this comparison, evaluation is made of the tagger upgrade.

6.1 η Photoproduction Differential Cross-Sections

6.1.1 Results

Differential cross-sections from threshold to 1100 MeV are shown in figure 6.1, with results from 1124 to 1395 MeV in figure 6.2. Plots are labelled using average incident photon energy weighted by photon flux. Combined statistical and systematic error bars are displayed. All values are listed in appendices B and C for the 2γ and 6γ analyses, respectively.

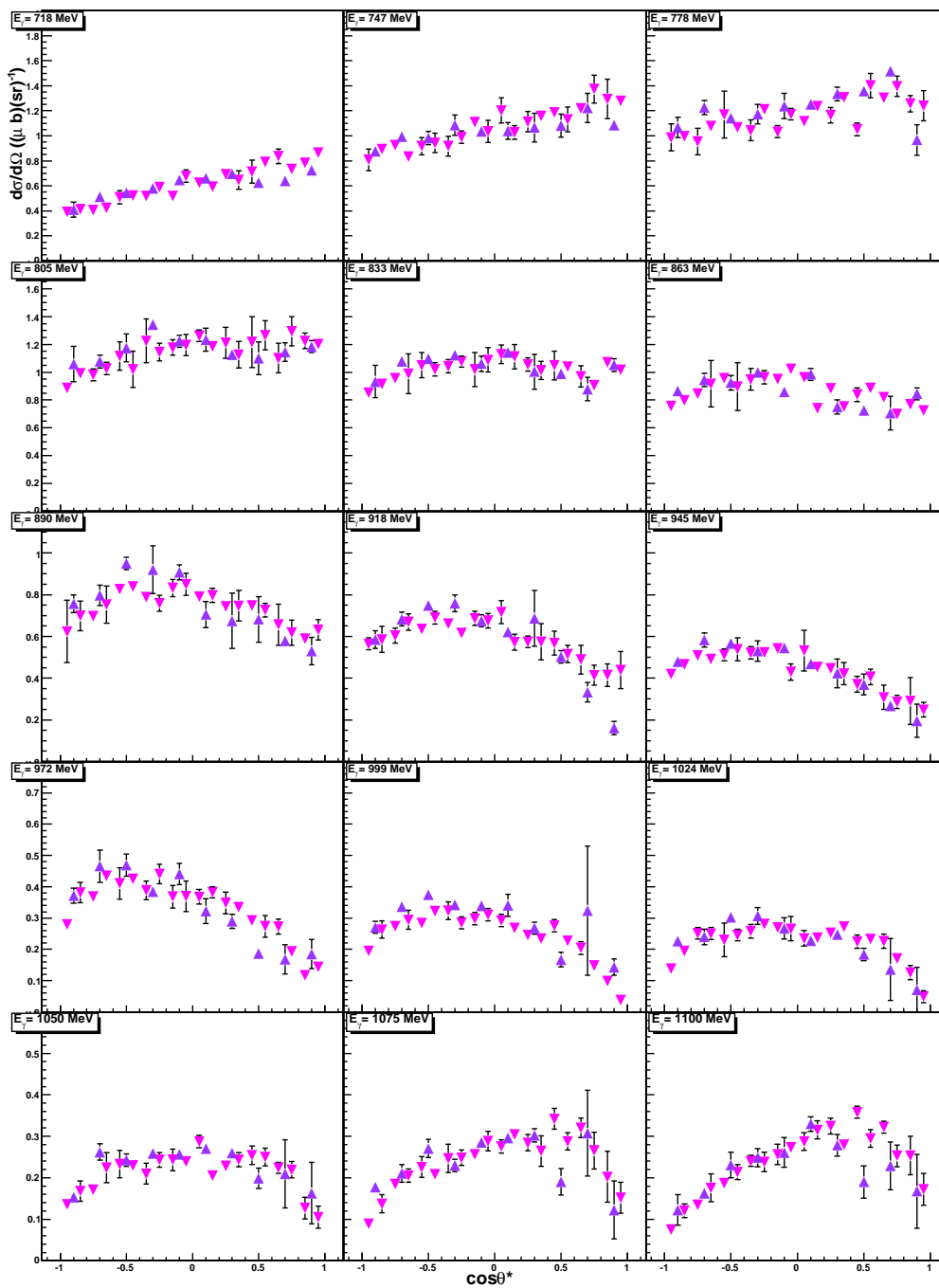


Figure 6.1: $\frac{d\sigma}{d\Omega}$ as a function of $\cos\theta_{\eta}^*$ for E_{γ} in the range 718 to 1100 MeV. Magenta, downwards pointing triangles are results of the $\eta \rightarrow 2\gamma$ analysis, purple upwards pointing triangles are those of the $\eta \rightarrow 6\gamma$ analysis.

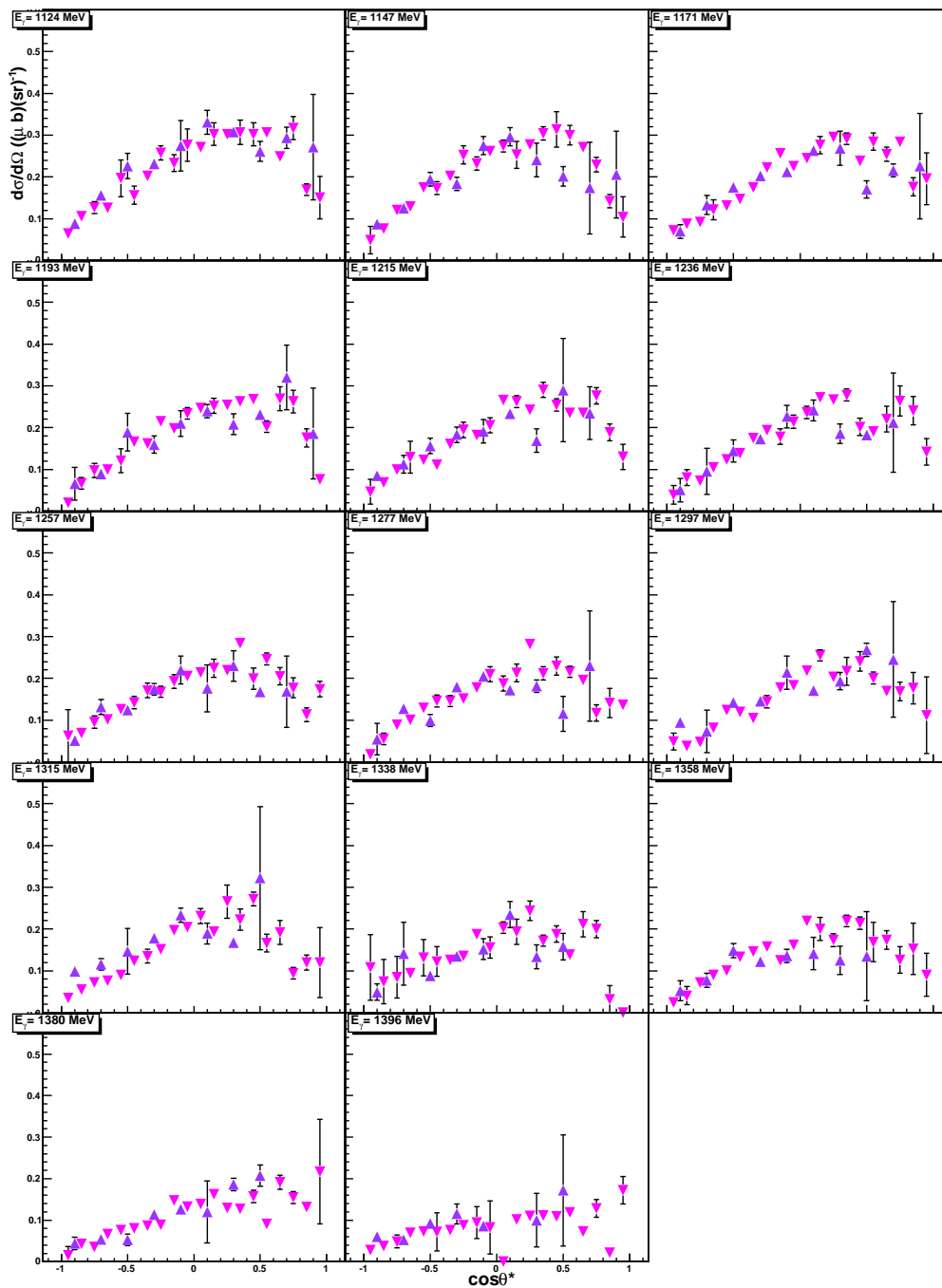


Figure 6.2: $\frac{d\sigma}{d\Omega}$ as a function of $\cos\theta_\eta^*$ for E_γ in the range 1124 to 1395 MeV, with symbols as defined in figure 6.1.

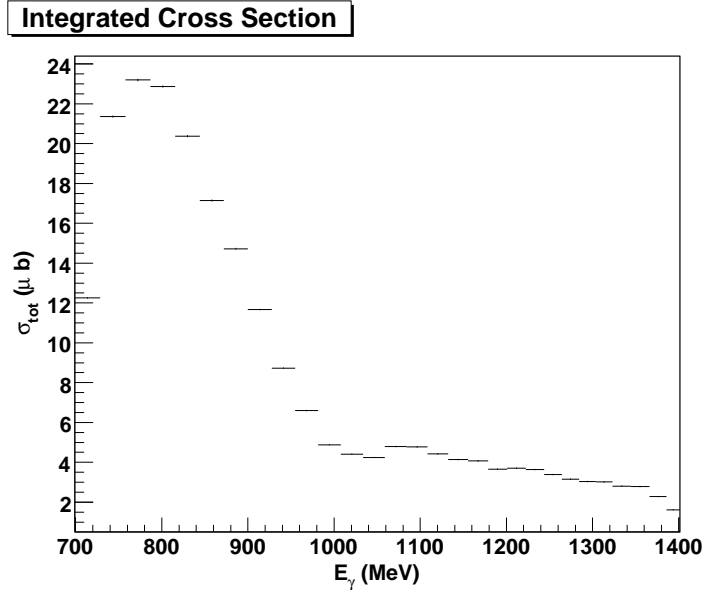


Figure 6.3: Integrated cross-section as a function of E_γ for the 2γ decay. Error bars include statistical errors only.

From the η photoproduction threshold at $E_\gamma = 707$ MeV to 890 MeV, the angular distribution of the differential cross-section is quite flat, indicating the dominance of S -wave processes in the reaction mechanism, in this case the $S_{11}(1535)$. The resonant shape is truncated at threshold and rises to a maximum at $E_\gamma = 805$ MeV, corresponding to the centre-of-mass energy of 1535 MeV, the S_{11} mass. This accounts for the cross-section being highest in this energy range, increasing from $\sim 0.55 \mu\text{b}/\text{sr}$ at threshold to $\sim 1.3 \mu\text{b}/\text{sr}$ at 757 and 786 MeV. The $S_{11}(1535)$ shape can also be seen in figure 6.3, which shows cross-section integrated over all angles for each energy bin.

From 918 to 1024 MeV, the differential cross-sections rise to a maximum value at backward angles, dropping towards forward angles. Cross-section decreases with increasing photon energy, from ~ 0.4 to $0.8 \mu\text{b}/\text{sr}$ at 918 MeV down to ~ 0.2 to $0.6 \mu\text{b}/\text{sr}$ at 1024 MeV.

By 1050 MeV this maximum has become more pronounced and moved to a forward angle. Cross-sections continue to decrease with increasing photon energy — from ~ 0.1 to $0.3 \mu\text{b}/\text{sr}$ at 1050 MeV down to ~ 0.02 to $0.12 \mu\text{b}/\text{sr}$ at 1395 MeV — but the rate of change lessens at higher E_γ .

Good agreement is found between the 2γ and 6γ analyses for all angles at low photon energies and at backward angles at higher E_γ . The discrepancies for $\cos\theta_\eta^* \geq 0.25$ at $E_\gamma \geq 1147$ MeV result from instability of the yield extraction fitting function — due to the poor statistics in this range where TAPS data has been excluded from the analysis — and from systematic uncertainty in the acceptance calculated, as described in section 5.9.2.

6.1.2 Comparison with Previous Data

The results of this analysis in the 2γ mode are compared to those of GRAAL [59] (see section 2.3) — using the closest available energy bins — and to the SAID model [40] (see section 2.1) in figures 6.4 and 6.5. Error bars on the GRAAL points include uncertainties in longitudinal target position, efficiency and hadronic background contamination, summed quadratically with statistical uncertainties. An additional systematic uncertainty of 2.3% in the absolute normalisation, due to uncertainties in beam flux monitoring efficiency, hydrogen density and target length, has not been included. Agreement between these two data sets and the partial wave analysis fit is in general reasonable, except at forward angles above 1193 MeV.

In the three lowest energy bins from threshold to 778 MeV, the results of the present analysis are close to those of GRAAL and SAID, but are not quite so flat. By 805 MeV the present work agrees well with SAID and GRAAL above $\cos\theta_\eta^* = -0.55$, although it is still slightly lower at backward angles. From 833 to 890 MeV this analysis and GRAAL agree well within errors, over the full $\cos\theta_\eta^*$ range. Both undercut SAID slightly at very forward and backward angles above 863 MeV. The same is true for this analysis in the 918 MeV bin. At 945 MeV, GRAAL agrees with SAID except at $\cos\theta_\eta^* = 0.95$. However, the present analysis is systematically lower aside from two points around $\cos\theta_\eta^* = 0.05$.

From 972 to 1050 MeV this analysis and GRAAL agree in all but a few points, but are lower than SAID, especially around $\cos\theta_\eta^* = 0.05$. At 1075 MeV all three agree and at 1100 MeV the present work agrees with SAID. At 1124 MeV, all data agree until $\cos\theta_\eta^* = 0.55$ where SAID and the A2 cross-sections drop towards forward angles while GRAAL's flatten out

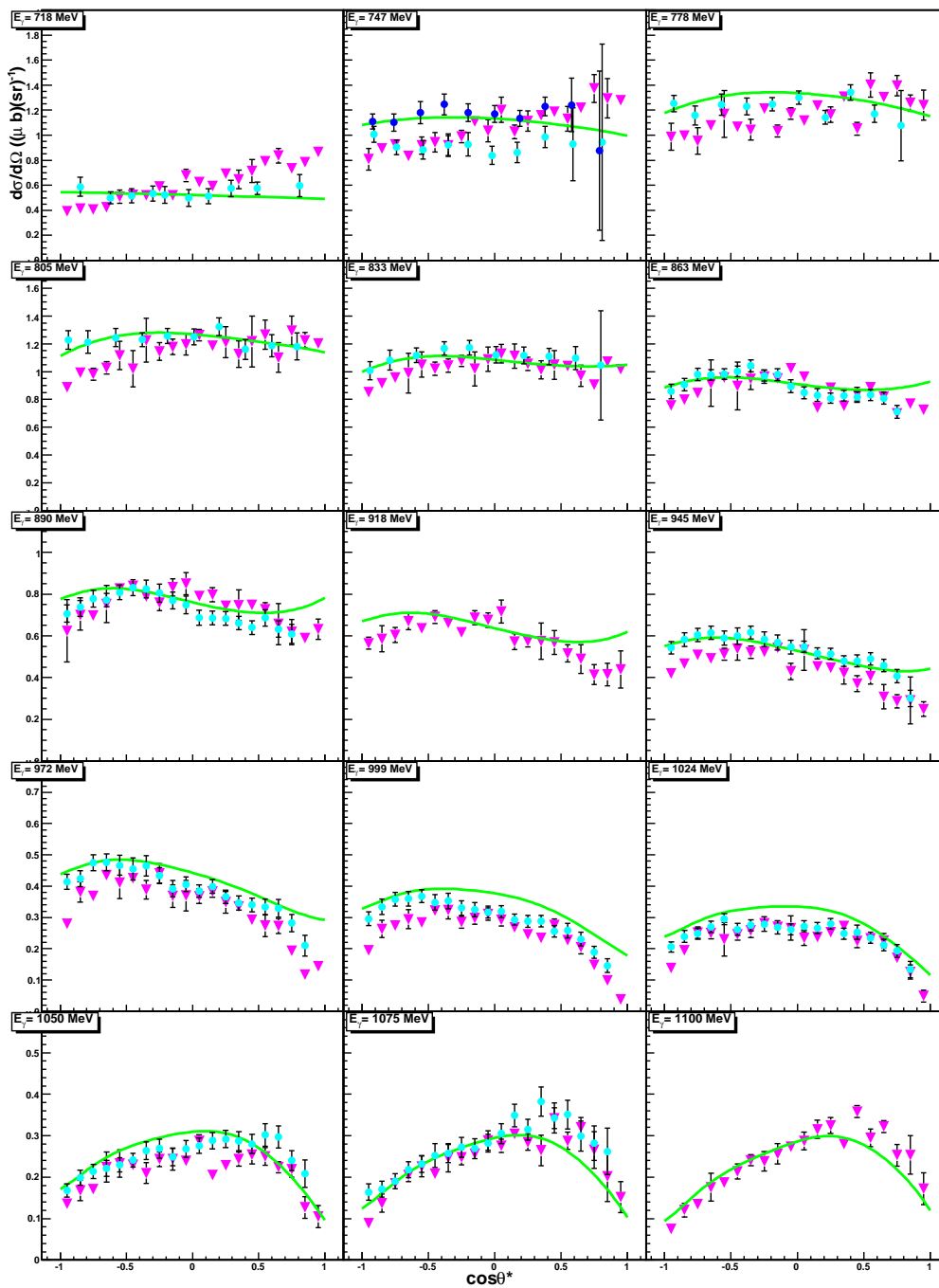


Figure 6.4: $\frac{d\sigma}{d\Omega}$ as a function of $\cos\theta_\eta^*$ for E_γ in the range 718 to 1100 MeV. Magenta triangles are the results of the $\eta \rightarrow 2\gamma$ analysis of the present work, blue circles are the GRAAL 2007 data [59] with the green line representing the SAID fit [40].

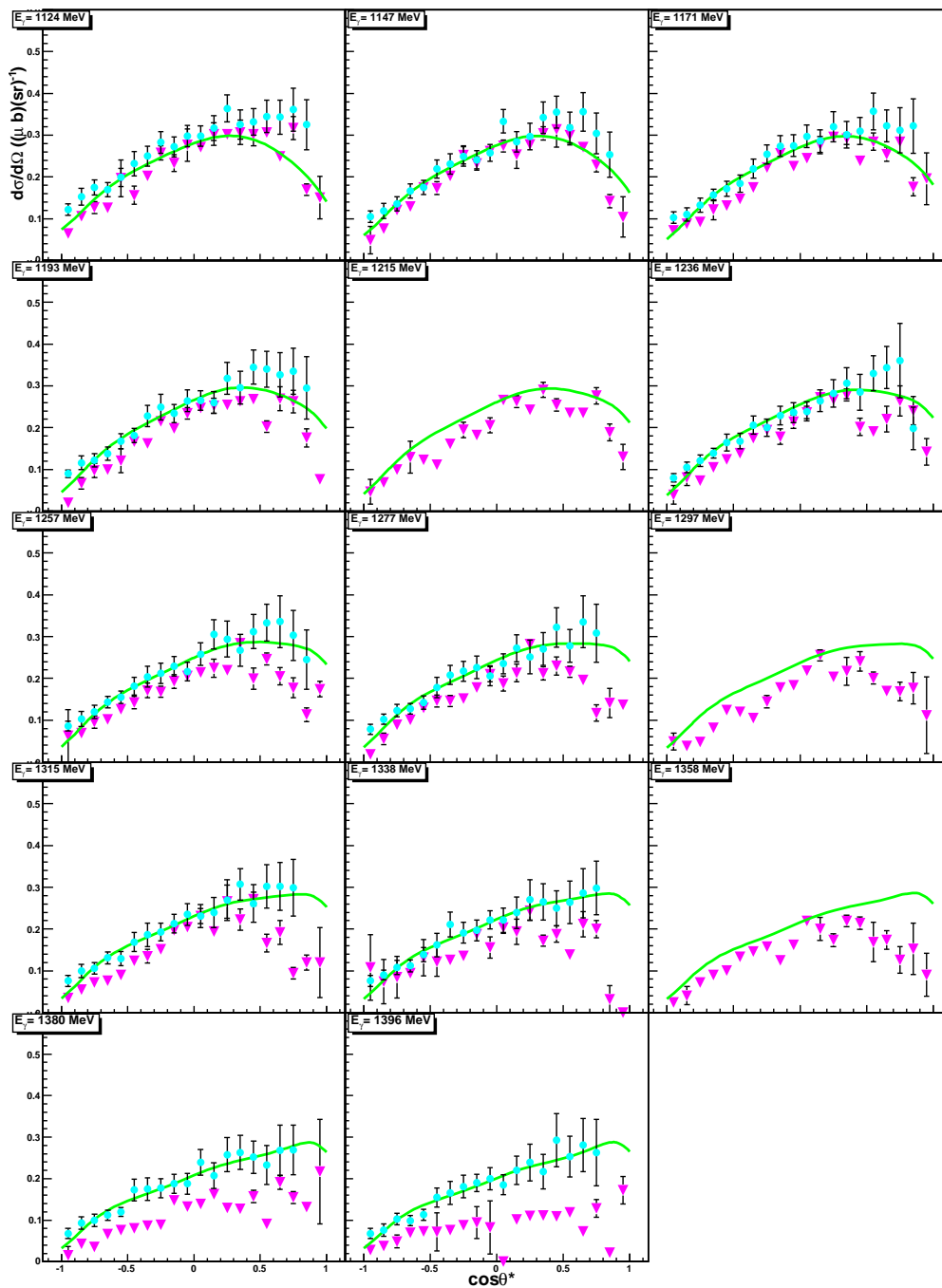


Figure 6.5: $\frac{d\sigma}{d\Omega}$ as a function of $\cos\theta_\eta^*$ for E_γ in the range 1124 to 1395 MeV, with symbols as defined in figure 6.4.

From 1147 to 1358 MeV all data agree up to at least $\cos\theta_\eta^* = 0.55$. Over this energy range, SAID shows a maximum in cross-sections moving from $\cos\theta_\eta^* \simeq 0.25$ to $\cos\theta_\eta^* \simeq 0.95$ as energy increases. The GRAAL results agree with SAID, but do not cover the furthest forward angles at high energy, so show no decrease with increasing angle above 1277 MeV. The present work indicates a decrease in cross-section from $\cos\theta_\eta^* \simeq 0.25$ for all energies above 1215 MeV and so differs from both SAID and GRAAL here. The CB-ELSA collaboration [58] also reports some low points in this region, as shown in figure 2.4. However, uncertainties in the present results are large in this range, as high as $\sim 44\%$ in a few bins, see section 5.9.2. An independent analysis of the $\eta \rightarrow 6\gamma$ decay mode [108] in this A2 data is underway. This involves use of the TAPS data, so should greatly increase statistics in the high energy, forward angle region, providing a more conclusive determination of the cross-section shape here.

In the two highest energy bins — 1380 and 1396 MeV — the results of this analysis are systematically lower than those of GRAAL and SAID. This can be accounted for by considering photon flux in the bottom plot of figure 5.4. The two lowest channel bins, corresponding to the highest photon energies, show high flux relative to their higher channel neighbours. This is due to noise in the scaler read-out cables which can be seen in the top left plot of figure 5.4.

6.2 Tagger Upgrade Appraisal

The good agreement of the η photoproduction differential cross-sections reported herein with those of the GRAAL collaboration and the SAID fit, along with the excitation function in figure 6.3, show that the upgraded tagger was working well in July 2007 and that the energy calibration for running at a main beam energy of 1508 MeV is satisfactory.

During this commissioning run, some minor problems were present. As discussed in section 5.5, the settings of discriminator voltages and of high voltage supplies of some channels were too high or low respectively, leading to low scaler counts. These have since been reset.

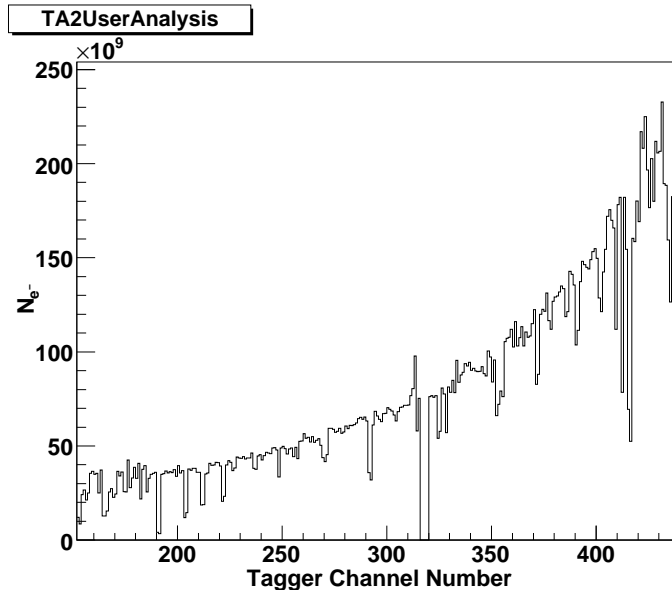


Figure 6.6: Tagger scalers from April 2009 [109].

Also visible in the scaler plot of figure 5.4 are anomalously high counts in certain channels. These were due to noise in read-out cables. Some dips in this plot were also due to poor connections in these cables. The cables in place for this work were SCSI cables with hand-crimped connectors. These were subsequently improved by soldering the connectors into place. The changes have resulted in a smoother scaler spectrum. Figure 6.6 shows an example from April 2009. Noise has been greatly reduced and the number of dips has decreased.

Some dips remain due to continuing instability in electrical connections. However, these should be remedied when replacement of the twisted-pair cables by more robust co-axial cables is complete. This was underway during January 2010.

6.3 Conclusions

Differential cross-section measurements for η photoproduction on the proton are presented, taken under the auspices of the A2 collaboration at the MAMI accelerator facility in Mainz, using the Crystal Ball and newly upgraded Glasgow Photon Tagging Spectrometer. These cover the incident photon energy range from threshold, at $E_\gamma = 707 \text{ MeV}$, to 1403 MeV over the full $\cos\theta_\eta^*$ range, -1 to 1. Internal

consistency is seen between the two η decay modes studied. Good agreement is also found with the most recent previous results, produced by the GRAAL collaboration in 2007 [59], and with the SAID fit to experimental data covering the time period 1963 to 2006 [40].

A total of 2,515,723 $\gamma p \rightarrow \eta p$ events were reconstructed in this analysis: 2,084,690 from the 2γ decay mode and 431,033 from 6γ decay. This is a two-and-a-half fold increase on the ~ 1 M events recorded by the 2007 GRAAL experiment [59], so provides a valuable addition to the world database of η photoproduction results.

The upgrade of the Glasgow Photon Tagging Spectrometer has also been described. The success of this project is reflected in the success of this analysis and the publication of other analyses from the A2 collaboration using the new detector [66, 110, 111]. More recent fine-tuning of discriminator thresholds and PMT supply voltages combined with cable repairs have improved the performance of the tagger. Installation of new cabling should fix the few remaining inefficient channels.

Analysis of this data set is ongoing. An independent investigation of the $\eta \rightarrow 3\pi^0$ decay mode has resulted in a publication for the A2 collaboration on the η slope parameter [66]. A second paper reporting η photoproduction differential cross-section measurements from that analysis and the present work is in preparation.

Further examination of η photoproduction is underway within A2. New data were taken in April 2009 from which the invariant ηp mass is being examined in order to search for a possible narrow resonance mooted by the GRAAL collaboration [112]. An extension of the analysis reported herein is also planned for the study of radiative η photoproduction — $\gamma p \rightarrow \eta p \gamma'$ — from which extraction of the $S_{11}(1535)$ magnetic dipole moment will be attempted [113].

The η meson and its connection to the $S_{11}(1535)$ resonance continue to be topics of theoretical and experimental interest. This thesis work has augmented the world data set of differential cross-section measurements and will continue to contribute to knowledge of the field as the Glasgow-Mainz Photon Tagging Spectrometer is used in the A2 collaboration for future experiments.

Bibliography

- [1] Edts. D. Adams et al. (1994) *Collins Gem English Dictionary*
- [2] Edts. J. Simpson et al. (1989) *Oxford English Dictionary*, 2nd Edition
- [3] A.V. Anisovich, A. Sarantsev, et al. (2005) *Photoproduction of Baryons Decaying into $N\pi$ and $N\eta$* , Eur. Phys. J. A **25**, pp 427–439
- [4] B. Krusche et al. (1995) *Near Threshold Photoproduction of η Mesons off the Proton*, Phys. Rev. Lett. **74**, pp 3736–3739
- [5] J.C. McGeorge, J.D. Kellie, E.F. McNicoll, et al. (2008) *Upgrade of the Glasgow Photon Tagging Spectrometer for Mainz MAMI-C*, Eur. Phys. J. A, **37**, pp 129–137
- [6] N. Bianchi, V. Muccifora, E. De Sanctis et al. (1996) *Total hadronic photoabsorption cross section on nuclei in the nucleon resonance region*, Phys. Rev. C **54**, pp 1688–1699
- [7] W.-M. Yao, et al. (2006), *Particle Data Group*, J. Phys. G **33**, p 1
- [8] M. Dugger (2001), *Eta(547) and Eta'(958) Photoproduction on the Proton*, PhD Thesis, Arizona State University
- [9] S. Capstick and N. Isgur (1986) *Baryons in a Relativized Quark Model with Chromodynamics*, Phys. Rev. D **34**, pp 2809–2835
- [10] L.Ya. Glozman, and D.O. Riska (1996) *Quark Model Explanation of the $N^* \rightarrow N \eta$ Branching Ratios*, Phys. Lett. B **366**, pp 305–310

- [11] N. Kaiser, P.B. Seigel and W. Weise (1995) *Chiral Dynamics and the $S_{11}(1535)$ Nucleon Resonance*, Phys. Lett. B **362**, pp 23–28
- [12] B. Krusche, Nimai C. Mukhopadhyay, J.-F. Zhang and M. Benmerrouche (1997) *Constraining $N^*(1535)$ Parameters from the Eta Photoproduction*, Phys. Lett. B **397**, pp 171–176
- [13] B. Krusche and S. Schadmand (2003) *Study of Non-Strange Baryon Resonances with Meson Photoproduction*, Prog. Part. Nuc. Phys. **51**, pp 399–485
- [14] M. MacCormick et al. (1996) *Total Photoabsorption Cross Sections for 1H , 2H and 3He from 200 to 800 MeV*, Phys. Rev. C **53**, pp 41–49
- [15] K. Buechler et al. (1994) *Photoproduction of Positive Pions from Hydrogen with PHOENICS at ELSA*, Phys. Rev. A **570**, pp 580–598
- [16] F. Haerter (1996) *Double Pion Photoproduction off the Proton at Threshold and in the Second Resonance Region*, PhD Thesis, Universität Basel
- [17] A. Braghieri, L.Y. Murphy et al. (1995) *Total Cross Section Measurement for the Three Double Pion Photoproduction Channels on the Proton*, Phys. Lett. B **363**, pp 46–50
- [18] F. Haerter et al. (1997) *Two Neutral Pion Photoproduction off the Proton Between Threshold and 800 MeV*, Phys. Lett. B **401**, pp 299–233
- [19] I.S. Barker, A. Donnachie and J.K. Storrow (1975) *Complete Experiments in Pseudoscalar Photoproduction*, Nuc. Phys. B. **95**, pp 347–356
- [20] B. Saghai and Z. Li (1998) *Study of the Baryon Resonance Structure via η Photoproduction*, Nuc. Phys. A **644**, pp 345–364
- [21] B. Saghai and Z. Li (2001) *Quark Model Study of the η Photo-production: Evidence for a New S_{11} Resonance*, Eur. Phys. J. A **11**, pp 217–230
- [22] B. Saghai and Z. Li (2003) *Beyond the Known Baryon Resonances*, Proceedings of the NSTAR2002 Workshop on the Physics of Excited Nucleons, Pittsburgh, 2002, arXiv.nucl-th/0305004

- [23] J. He, B. Saghai, Z. Li, Q. Zhao and J. Durand (2008) *Chiral Constituent Quark Model Study of the Process $\gamma p \rightarrow \eta p$* , Eur. Phys. J. A **35**, pp 312–324
- [24] L.Ya. Glozman, W. Plessas, K. Varga and R.F. Wagenbrunn (1998) *Unified Description of Light- and Strange-Baryon Spectra*, Phys. Rev. D **58**, p 094030
- [25] M. Benmerrouche and Nimai C. Mukhopadhyay (1991) *η Photoproduction from Threshold Through the $S_{11}(1535)$ Resonance*, Phys. Rev. Lett. **67**, pp 1070–1073
- [26] Nimai C. Mukhopadhyay, J.-F. Zhang and M. Benmerrouche (1995) *Photoproduction of η Mesons Near Threshold*, Phys. Rev. Lett. **75**, p 3022
- [27] L. Tiator, D. Drechsel, G. Knöchlein and C. Bennhold (1999) *Analysis of Resonance Multipoles from Polarization Observables in η Photoproduction*, Phys. Rev. C **60**, p 035210
- [28] W. Chiang, S.N. Yang, L. Tiator and D. Drechsel (2002) *An Isobar Model for η Photo- and Electroproduction on the Nucleon*, Nuc. Phys. A **700**, pp 429–456
- [29] W. Chiang, S.N. Yang, L. Tiator, M. Vanderhaeghen and D. Drechsel (2003) *A Reggeized Model for η and η' Photoproduction*, Phys. Rev. C **68**, p 045202
- [30] L. Tiator (2006) *Photoproduction of Eta and Etaprime Mesons on the Nucleon*, Proceedings of the Meson2006 Workshop, Cracow, arXiv.nucl-th/0610114
- [31] A.V. Sarantsev, V.A. Nikonov, A.V. Anisovich, et al. (2005) *Decays of Baryon Resonances into ΛK^+ , $\Sigma^0 K^+$ and $\Sigma^+ K^0$* , Eur. Phys. J. A **25**, pp 441–453
- [32] N. Kaiser, T. Waas and W. Weise (1996) *$SU(3)$ Chiral Dynamics With Coupled Channels Eta and Kaon Photoproduction*, Nuc. Phys. A **612**, pp 297–320
- [33] Z. Li and R. Workman (1996) *Do We Have Three S_{11} Resonances in the Second Resonance Region*, Phys. Rev. C **53**, pp 549–552
- [34] A.J.G. Hey, P.J. Litchfield and R.J. Cashmore (1975) *$SU(6)_W$ and Decays of Baryons Resonances*, Nuc. Phys. B **95**, pp 516–546

- [35] N. Isgur and G. Karl (1977) *Hyperfine Interactions in Negative Parity Baryons*, Phys. Lett. B **72**, pp 109–113
- [36] C.A. Paterson (2008) *Polarisation Observables in Strangeness Photoproduction with CLAS at Jefferson Lab*, PhD Thesis, University of Glasgow
- [37] H.R. Hicks, S.R. Deans, D.T. Jacobs, P.W. Lyons and D.L. Montgomery (1973) *Isobar Analysis of $\gamma p \rightarrow \eta p$* , Phys. Rev. D **7**, pp 2614–2626
- [38] M. Guidal, J.-M. Laget and M. Vanderhaeghen (1997) *Pion and Kaon Photoproduction at High Energies: Forward and Intermediate Angles*, Nuc. Phys. A **627**, pp 645–678
- [39] A.W. Thomas and W. Weise (2001) *The Structure of the Nucleon*, Wiley
- [40] R.A. Arndt et al., <http://gwdac.phys.gwu.edu>, last accessed 2nd January 2010
- [41] C. Bacci, G. Penso, G. Salvani and A. Wattenberg (1963) *Photoproduction and Neutral Decay Modes of the η Particle*, Phys. Rev. Lett. **11**, pp 37–42
- [42] C. Bacci, C. Mencuccini, G. Penso, G. Salvani and V. Silverstrini (1966) *Photoproduction of the η Particle at 800–1000 MeV. A Comparison Between the πN and the ηN System*, Phys. Rev. Lett. **16**, pp 157–161
- [43] C. Bacci, R. Baldini-Celio, C. Mencuccini, A. Reale, M. Spinetti and A. Zallo (1968) *Angular Distributions from Eta-Meson Photoproduction from Hydrogen at 775–850 MeV*, Phys. Rev. Lett. **20**, pp 571–574
- [44] B. Delcourt, J. Lefrançois, J.P. Perez-Y-Jorba, G. Sauvage and G. Mennessier (1969) *Photoproduction of η Mesons Between Threshold and 900 MeV*, Phys. Lett. B **29**, pp 75–78
- [45] M. Hongoh, et al. (1971) *Differential Cross Section and Recoil Proton Polarization of η -Meson Photoproduction at 890 MeV*, Lettere al Nuovo Cimento **2**, pp 317–320

- [46] P.S.L. Booth, L.J. Carroll, J.R. Holt, J.N. Jackson, W.H. Range, K.A. Sparkes and J.R. Wormald (1974) *Differential Cross Sections for the Photoproduction of Eta Mesons from Protons Near 2 GeV*, Nuc. Phys. B **71**, pp 211–216
- [47] S. Homma, M. Kanazawa, K. Maruyama, Y. Murata, H. Okuno, A. Sasaki and T. Taniguchi (1987) *Photoproduction of η Mesons from Protons at Incident Energies Below 1 GeV*, Journal of the Physical Society of Japan **57**, pp 828–843
- [48] S.A. Dytman et al. (1995) *Study of Baryon Resonances Through $\gamma p \rightarrow \eta p$ Differential Cross Sections*, Phys. Rev. C **51**, pp 2710–2715
- [49] M. Dugger, B.G. Ritchie, J. Ball, E. Pasyuk, et al. (2002) *η Photoproduction on the Proton for Photon Energies from 0.75 to 1.95 GeV*, Phys. Rev. Lett. **89**, p 222002
- [50] F. Renard et al. (2002) *Differential Cross Section Measurements of η Photoproduction on the Proton from Threshold to 1100 MeV*, Phys. Lett. B **528**, pp 215–220
- [51] J. Ahrens et al. (2003) *First Measurement of the Helicity-Dependent $\vec{\gamma} \vec{p} \rightarrow \eta p$ Differential Cross Section*, Eur. Phys. J. A **17**, pp 241–244
- [52] V. Credé, O. Bartholomy, et al. (2005) *Photoproduction of η Mesons off Protons for $0.75 \text{ GeV} < E_\gamma < 3 \text{ GeV}$* , Phys. Rev. Lett. **94**, p 012004
- [53] T. Nakabayashi, et al. (2006) *Photoproduction of η Mesons off Protons for $\leq 1.15 \text{ GeV}$* , Phys. Rev. C **74**, p 035202
- [54] A.W. Hendry and R.G. Moorhouse (1965) *Interpretation of the $N\eta$ state at the Production Threshold as a $J^P = \frac{1}{2}^-$ Resonance*, Phys. Letters **18**, p 171
- [55] A. Christ et al. (1973) *Photoproduction of η -Mesons on Hydrogen at Photon Energies Between 1.5 and 2.2 GeV*, Lettere al Nuovo Cimento **8**, pp 1039–1043

- [56] P.S.L. Booth, J.S. Barton, L.J. Carroll, J.R Holt, J.N. Jackson, W.H. Range, K.A. Sparkes and J.R. Wormald (1971) *The Photoproduction of Eta Mesons at Small Angles*, Nuc. Phys. B **25**, pp 510–518
- [57] H.A. Vartapetyan and S.E. Piliposyan (1980) *Measurements of Cross Section Asymmetry by Polarized Photons and Models of η^0 -Meson Photoproduction in the Energy Range $E_\gamma=1-2$ GeV*, Soviet Journal of Nuclear Physics **32**, pp 804–825
- [58] O.Bartholomy, R.Bogendörfer, V. Credé, et al. (2007), *Photoproduction of η -mesons Off Protons*, Eur. Phys. J. A, **33**, pp 133–146
- [59] O. Bartalini, et al. (2007), *Measurement of η -photoproduction on the Proton from Threshold to 1500 MeV*, Eur. Phys. J. A, **33**, pp 169–184
- [60] D. Diakonov, V. Petrov and M. Polyakov (1997) *Exotic Anti-Decuplet of Baryons: Prediction from Chiral Solitons*, Z. Phys. A **359**, pp 305–314
- [61] B.R. Martin and G. Shaw (2003) *Particle Physics, Second Edition*, Wiley pp 55-56
- [62] H.W. Koch and J.W. Motz (1959) *Bremsstrahlung Cross-Section Formulas and Related Data*, Rev. Mod. Phys. **31**, pp 920–955
- [63] J.D. Kellie, I. Anthony, S.J. Hall, A. McPherson, P.J. Thorley and S.L. Wan (1985) *A Tagged Photon Spectrometer for Use With the Mainz 180 MeV Microtron*, Nuc. Inst. Meth. A, **241**, pp 153–168
- [64] I. Anthony, J.D. Kellie, S.J. Hall and G.J. Miller (1991) *Design of a Tagged Photon Spectrometer for Use With the Mainz 840 MeV Microtron*, Nuc. Inst. Meth. A, **301**, pp 230–240
- [65] S.J. Hall, G.J. Miller, R. Beck and P. Jennewein (1996) *A Focal Plane System for the 885 MeV Tagged Photon Spectrometer at MAMI-B*, Nuc. Inst. Meth. A, **368**, pp 698–708

- [66] S. Prakhov, et al. (2009) *Measurement of the Slope Parameter α for the $\eta \rightarrow 3 \pi^0$ decay with the Crystal Ball at MAMI-C*, Phys. Rev C, **79**, p 035204
- [67] I. Anthony (2006) *Private Communication*
- [68] *Caylar Drusch Products Nuclear Magnetic Resonance NMR20 Gaussmeter, Manual*
- [69] J.C. McGeorge (2009) *Private Communication*
- [70] V. Bekrenev (2005) *Private communication*
- [71] J.R.M. Annand (2008) *The Glasgow / Mainz Bremsstrahlung Tagger Operations Manual*, CB@MAMI and A2-Collaboration Technical Report
- [72] J.R.M. Annand (2006) *Test Procedure for Tagger Amplifier / Discriminator Cards. Version 3L4, Procedure Version 2*, Internal Report
- [73] J.R.M. Annand (2006) *Commissioning of the Upgraded Glasgow / Mainz Tagger*, Internal Report
- [74] I. Anthony (2007) *Private Communication*
- [75] A. Reiter et al. (2007) *A Microscope for the Glasgow Photon Tagging Spectrometer in Mainz*, Eur. Phys. J. A, **30**, pp 461–467
- [76] J.C. McGeorge (2007) *Private Communication*
- [77] K.-H. Kaiser, et al. (2008), *The 1.5 GeV Harmonic Double-Sided Microtron at Mainz University*, Nuc. Inst. Meth. A, **593**, pp 159-170
- [78] A. Jankowiak (2006), *The Mainz Microtron MAMI — Past and Future*, Eur. Phys. J. A, **28**, pp 149–160
- [79] H. Herminhaus, A. Feder, K.H. Kaiser, W. Manz and H.v.d. Schmitt (1976) *The Design of a Cascaded 800 MeV Normal Conducting C.W. Race Track Microtron*, Nuc. Inst. Meth. **138**, pp 1–12

- [80] A. Thomas (2007) *Crystal Ball Hydrogen (Deuterium) Target Manual*, CB@MAMI and A2-Collaboration Technical Report
- [81] M. Korolija (2009), *Private Communication*
- [82] E.J. Downie (2006) *Radiative π^0 Photoproduction in the Region of the $\Delta(1232)$ Resonance*, PhD Thesis, University of Glasgow
- [83] E.D. Bloom and C.W. Peck (1983) *Physics With the Crystal Ball Detector*, Annu. Rev. Nucl. Part. Sci. **33**, pp 143–198
- [84] B.M.K. Nefkens (1995) *The Crystal Ball*, Internal Report
- [85] C.M. Tarbet (2007) *Coherent π^0 Photoproduction on Nuclei*, PhD Thesis, University of Edinburgh
- [86] A. Nikolaev (2006) *Status of the η Mass Measurement With the Crystal Ball at MAMI*, Acta Physica Slovaca **56**, pp 397–402
- [87] M. Unverzagt (2009) *Determination of the Dalitz plot parameter α for the $\eta \rightarrow 3\pi^0$ decay with the Crystal Ball at MAMI-B*, Eur. Phys J. A **39**, pp 169–177
- [88] T. Jude, D.I. Glazier and D.P Watts (2008) *Measurement of Polarisation Transfer in Hyperon Photoproduction at MAMI*, Int. J. Mod. Phys. A **24**, pp 607–610
- [89] D. Watts (2006) *New Particle ID Detector for Crystal Ball at MAMI-C*, A2-Collaboration Meeting Presentation
- [90] D. Watts (2004) *The Crystal Ball and TAPS Detectors at the MAMI Electron Beam Facility*, Internal Report
- [91] R. Novotny (1991) *The BaF₂ Photon Spectrometer TAPS*, IEEE Transaction on Nuclear Science **38**, pp 379-385
- [92] R. Novotny (2002) *Scintillators for Photon Detection at Medium Energies*, Nuc. Inst. Meth. A, **486**, pp 131-135

- [93] S. Janssen, W. Döring, V. Metag and R. Novotny (2000) *The New Charged-Particle Veto Detector for the Photon Spectrometer TAPS*, IEEE Transaction on Nuclear Science **47**, pp 250-254
- [94] J.R.M. Annand (2005) *Data Acquisition and Analysis Systems for Crystal Ball Experiments at the Mainz Tagged Photon Facility*, Presentation
- [95] P. Drexler, U. Thöring, et al. (2003) *The New Read-Out Electronics of the BaF₂-Calorimeter TAPS*, IEEE Transaction on Nuclear Science **50**, pp 969-973
- [96] J.R.M. Annand (2006) *Experimental Systems for A2 / Crystal Ball Experiments at the MAMI-C Tagged Photon Facility*, Presentation
- [97] J.R.M. Annand (2009) *Private communication*
- [98] J.R.M. Annand (2007) *Data Analysis Within an AcqRoot Framework*, Internal Report
- [99] I. Suarez (2009) *Private Communication*
- [100] J.W. Brudvik (2007) *Measurement of the Branching Ratio for Eta-Meson Decay into Neutral Pion and Two Photons*, PhD Thesis, University of California Los Angeles
- [101] R.F.B Codling (2008) *Photon Asymmetry of the $\vec{\gamma}p \rightarrow \pi^+n$ Reaction in the Region of the $\Delta(1232)$ Resonance*, Masters Thesis, University of Glasgow
- [102] T. Jude (2009), *Private Communication*
- [103] J.C. McGeorge (2009) *Use of Tagger TDCs for TAPS Time-of-Flight*, Internal Report
- [104] D. Watts (2009) *Private Communication*
- [105] Edts. Ilka Antcheva and Olivier Couet (2009) *Root Users Guide 5.22*, <http://Root.cern.ch>, last accessed 2nd January 2010
- [106] <http://geant4.web.cern.ch/geant4/>, last accessed 2nd January 2010

- [107] D. Glazier (2008) *A Geant4 Simulation for the CrystalBall@MAMI Setup*, Internal report
- [108] S. Prakhov (2009) *Private Communication*
- [109] J. Mancell (2009), *Private communication*
- [110] A. Starostin, et al. (2009) *Search for the Charge-Conjugation-Forbidden Decay $\omega \rightarrow \eta\pi^0$* , Phys. Rev. C, **79**, p 065201
- [111] V.L. Kashevarov, et al. (2009) *Photoproduction of $\pi^0\eta$ on Protons and the $\Delta(1700)D_{33}$ Resonance*, Submitted to Eur. Phys. J., arXiv:0901.3888
- [112] V. Kuznetsov, M.V. Polyakov, T. Boiko, J. Jang, A. Kim, W. Kim, H.S. Lee A. Ni and G.-S. Yang (2008), *Evidence for a Narrow $N(1685)$ Resonance in η Photoproduction off the Nucleon*, arXiv:0807.2316v1 [hep-ex]
- [113] M. Kotulla, J.R.M. Annand, B. Krusche and B.M.K. Nefkens (2005) *The Reaction $\gamma p \rightarrow \eta\gamma'p$ and the Magnetic Moment of the $S_{11}^+(1535)$ Resonance*, MAMI PAC Proposal
- [114] A.P. Balachandran, W.J. Meggs, J. Nuyts and P. Ramond (1968) *Simultaneous Partial-Wave Expansion in the Mandelstam Variables: The Group $SU(3)$* , Phys. Rev. **176**, pp 1700–1705
- [115] H. Denizli, J. Mueller et al. (2007) *Q^2 Dependence of the $S_{11}(1535)$ Photocoupling and Evidence for a P -wave Resonance in η Electroproduction*, Phys. Rev. C **76**, p 015204

Appendix A

Definitions

A.1 Quantum Numbers

Internal quantum numbers [61]:

- Charge (Q) is electric charge in units of electron charge.
- Baryon number (B) is defined:

$$B = \frac{1}{3}(N_q - N_{\bar{q}})$$

where N_q and $N_{\bar{q}}$ are, respectively, number of quarks and anti-quarks.

- Strangeness (S) is the difference between number of constituent anti-strange and strange quarks. Analogous quantum numbers associated with charm, top and bottom quarks are C , \tilde{B} and T , respectively.
- The third component of isospin (I_3) is defined thus:

$$I_3 = Q - \frac{1}{2}Y$$

where hypercharge, Y , is defined as:

$$Y = B + S + C + \tilde{B} + T$$

- Isospin (I) is the maximum value of I_3 within an isospin multiplet.

- Orbital Angular Momentum (L) is the angular momentum due to quarks orbiting one another within a particle.

Quantum numbers associated with space-time symmetries:

- Spin (S), or intrinsic angular momentum, is the angular momentum of a particle at rest.
- Total Angular Momentum (J) is the sum of orbital angular momentum and spin, $\vec{J} = \vec{L} + \vec{S}$.
- Parity (P) is the intrinsic parity of a particle at rest. $P = \pm 1$ are eigenstates of the parity operator, which performs spatial inversions.
- C -parity (C) also takes values of ± 1 , denoting even and odd symmetry under charge conjugation, the exchange of a particle with its antiparticle.

A.2 Properties of Particles and Resonances

Resonances are modelled using the relativistic Breit-Wigner distribution [12]:

$$f(E) \sim \frac{1}{(E^2 - M^2)^2 + M^2\Gamma^2} \quad (\text{A.2.1})$$

where, E is the centre-of-mass energy producing the resonance, M is the mass of the resonance and Γ the width of the resonance.

- Invariant mass, W , is the difference between the energy and momentum of a resonance:

$$W^2 = E^2 - \vec{p}^2$$

in natural units ($c = \hbar = 1$). This is constant in all frames of reference.

- Width, Γ , is related to the mean lifetime, τ of a resonance:

$$\Gamma = \frac{1}{\tau}$$

in natural units, when modelling resonances using the relativistic Breit-Wigner distribution. The branching ratio of a given decay is the ratio of the full width, Γ_{tot} , to the partial width, Γ , associated with that decay, $\frac{\Gamma_{tot}}{\Gamma}$.

General properties of particles and interactions include the following:

- A probability amplitude is a complex number whose absolute value squared represents a probability. The transition from the nucleon ground state to any resonant excited state can be expressed in terms of electromagnetic, or photon, helicity amplitudes [39], $A_{\frac{m}{2}}^N$, where $N = p, n$ is the nucleon and $\frac{m}{2}$ is the total helicity — the projection of spin along the direction of motion — of the γN state, equivalent to that of the resonance. These amplitudes are given in units of $GeV^{-\frac{1}{2}}$ [20] and are also known as photocoupling amplitudes.
- Coupling constants quantify the strength of an interaction and are dimensionless. These are normalised by $\frac{1}{4\pi}$. For example, $\frac{g_{\eta NN}^2}{4\pi}$ describes the strength of direct coupling of the nucleon to an $N\eta$ final state, *ie.* in the present work it quantifies the probability of a contribution to the η photoproduction cross-section from Born terms.
- Electrostrong coupling, ξ , is a model independent term related — for η photoproduction — to the photon helicity amplitude thus [21]:

$$A_{\frac{1}{2}}^p = \sqrt{\frac{q M_R \Gamma_T}{k M_p b_\eta}} \xi \quad (\text{A.2.2})$$

where k and q are the momenta of the incoming photon and outgoing η meson respectively, M_R and M_p are, respectively, the resonance and proton masses, Γ_T is the total width of the resonance and b_η is the branching ratio $\frac{\Gamma_{N\eta}}{\Gamma_T}$. Units are GeV^{-1} .

A.3 Mandelstam Variables

Mandelstam variables are a Lorentz-invariant means by which to describe scattering processes involving two particles in each of the initial and final states. These are defined as follows [114]:

$$s = (p_1 + p_2)^2 = (p_3 + p_4)^2 \quad (\text{A.3.3})$$

$$t = (p_1 - p_3)^2 = (p_2 - p_4)^2 \quad (\text{A.3.4})$$

$$u = (p_1 - p_4)^2 = (p_2 - p_3)^2 \quad (\text{A.3.5})$$

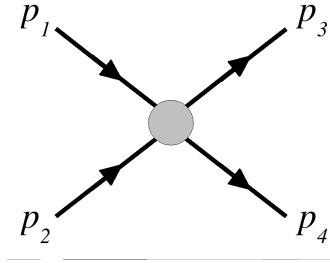


Figure A.1: 4-momenta of particles in a scattering process for which Mandelstam variables are defined.

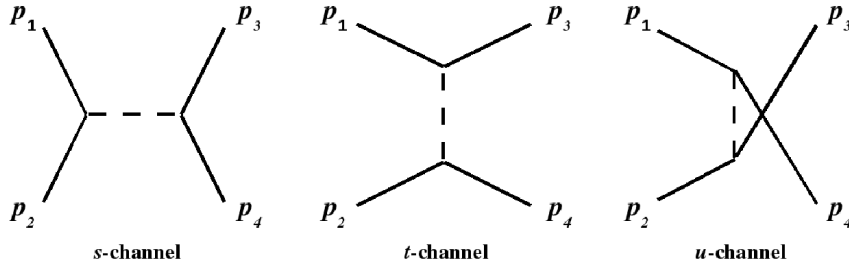


Figure A.2: Feynman diagrams for s , t and u -channels.

where p_1 and p_2 are four-momenta of the incoming particles while p_3 and p_4 are four-momenta of the outgoing particles, as shown in figure A.1. s is the invariant mass; t is the square of the momentum transfer.

s , t and u -channels are also defined, wherein an intermediate state with four-momentum s , t or u , respectively, is produced. Feynman diagrams for these processes are shown in figure A.2.

A.4 Electric and Magnetic Multipoles

Transitions between discrete excited states, such as the nucleon resonances, are confined to occur only with integer steps of angular momentum. Electric and magnetic radiation emitted or absorbed in these transitions is classified into multipoles. The photoproduction multipoles for pseudo-scalar mesons are denoted $\mathcal{M}_{\ell\pm} = E_{\ell\pm}, M_{\ell\pm}$ [28], where ℓ denotes the relative orbital angular momentum of the final meson–nucleon state (0, 1 and 2 correspond to S -, D - and P -waves respectively) and \pm indicates addition to or subtraction from ℓ of the nucleonic spin, $\frac{1}{2}$, to give the to-

tal angular momentum, J_{N^*} , of the intermediate resonance. The $S_{11}(1535)$ can be excited only by the E_{0+} multipole [4].

A.5 η Electroproduction

The proton can also be excited to the $S_{11}(1535)$ by η electroproduction [13]:

$$ep \rightarrow e'\eta p \tag{A.5.6}$$

wherein the incoming electron emits a virtual photon. Four-momentum is transferred, via the virtual photon, from the electron to the resonance. Q^2 is the invariant square of this momentum [115]. $Q^2 = 0$ represents the real photon limit, *ie.* photoproduction. In electroproduction, $A_{\frac{1}{2}}^p$ varies with Q^2 . Combined analyses of electro- and photoproduction are used in some of the models reviewed in section 1.3.

Appendix B

Tables of $\eta \rightarrow 2\gamma$ Results

Differential cross-sections, $\frac{d\sigma}{d\Omega}$, of η photoproduction are presented for the decay mode $\eta \rightarrow 2\gamma$ in the incident photon energy range $703 \leq E_\gamma \leq 1403$ MeV for $-1 \leq \cos\theta_\eta^* \leq 1$. Lower and upper bounds are listed with average values of E_γ and $\cos\theta_\eta^*$ bins, respectively in tables B.1 and B.2. Differential cross-sections, with statistical and systematic errors, are listed in tables B.3 to B.17.

Tagger Channels	Avg. E_γ (MeV)	Min. E_γ (MeV)	Max. E_γ (MeV)
197–203	718.3	703.4	733.2
190–196	747.0	732.8	762.3
183–189	777.7	761.9	791.3
176–182	805.2	790.9	820.0
169–175	833.4	819.6	848.4
162–168	862.6	848.1	876.5
155–161	889.9	876.2	904.4
148–154	918.0	902.0	931.7
141–147	945.2	931.5	958.8
134–140	972.0	958.5	985.5
127–133	998.8	985.2	1011.7
120–126	1024.5	1011.5	1037.6
113–119	1050.4	1037.3	1062.9
106–112	1075.0	1062.7	1087.7
99–105	1099.8	1087.6	1112.1
92–98	1124.3	1111.9	1136.0
85–91	1147.5	1135.8	1159.3
78–84	1170.6	1159.1	1182.0
71–77	1192.7	1181.8	1204.2
64–70	1215.2	1204.0	1225.8
57–63	1236.2	1225.7	1246.8
50–56	1256.9	1246.7	1267.3
43–49	1277.2	1267.2	1287.3
36–42	1297.4	1287.2	1306.7
29–35	1314.9	1306.7	1326.1
22–28	1337.9	1326.1	1347.6
15–21	1358.1	1347.5	1369.3
8–14	1379.9	1369.3	1372.2
1–7	1395.6	1388.3	1403.4

Table B.1: Minimum, maximum and flux-weighted average values for each incident photon energy bin.

Avg. $\cos \theta_\eta^*$	Min. $\cos \theta_\eta^*$	Max. $\cos \theta_\eta^*$
-0.95	-1.00	-0.90
-0.85	-0.90	-0.80
-0.75	-0.80	-0.70
-0.65	-0.70	-0.60
-0.55	-0.60	-0.50
-0.45	-0.50	-0.40
-0.35	-0.40	-0.30
-0.25	-0.30	-0.20
-0.15	-0.20	-0.10
-0.05	-0.10	0.00
0.05	0.00	0.10
0.15	0.10	0.20
0.25	0.20	0.30
0.35	0.30	0.40
0.45	0.40	0.50
0.55	0.50	0.60
0.65	0.60	0.70
0.75	0.70	0.80
0.85	0.80	0.90
0.95	0.90	1.00

Table B.2: Minimum, maximum and average values for each $\cos \theta_\eta^*$ bin used in the 2γ analysis.

$\cos\theta_\eta^*$	$E_\gamma = 718 \text{ MeV}$	$E_\gamma = 747 \text{ MeV}$
	$\frac{d\sigma}{d\Omega} \pm \Delta \left(\frac{d\sigma}{d\Omega} \right)_{stat.} \pm \Delta \left(\frac{d\sigma}{d\Omega} \right)_{sys.}$	$\frac{d\sigma}{d\Omega} \pm \Delta \left(\frac{d\sigma}{d\Omega} \right)_{stat.} \pm \Delta \left(\frac{d\sigma}{d\Omega} \right)_{sys.}$
-0.95	$0.3929 \pm 0.0050 \pm 0.0399$	$0.8076 \pm 0.0082 \pm 0.0861$
-0.85	$0.4150 \pm 0.0053 \pm 0.0122$	$0.8926 \pm 0.0088 \pm 0.0320$
-0.75	$0.4054 \pm 0.0051 \pm 0.0195$	$0.9245 \pm 0.0089 \pm 0.0061$
-0.65	$0.4234 \pm 0.0054 \pm 0.0129$	$0.8355 \pm 0.0082 \pm 0.0179$
-0.55	$0.5087 \pm 0.0063 \pm 0.0524$	$0.9174 \pm 0.0090 \pm 0.0681$
-0.45	$0.5214 \pm 0.0065 \pm 0.0405$	$0.9432 \pm 0.0093 \pm 0.0772$
-0.35	$0.5186 \pm 0.0064 \pm 0.0306$	$0.9174 \pm 0.0090 \pm 0.0785$
-0.25	$0.5899 \pm 0.0071 \pm 0.0152$	$0.9896 \pm 0.0097 \pm 0.0479$
-0.15	$0.5195 \pm 0.0064 \pm 0.0209$	$1.1093 \pm 0.0105 \pm 0.0058$
-0.05	$0.6772 \pm 0.0080 \pm 0.0486$	$1.0354 \pm 0.0100 \pm 0.0871$
0.05	$0.6257 \pm 0.0074 \pm 0.0126$	$1.2032 \pm 0.0116 \pm 0.0991$
0.15	$0.5920 \pm 0.0070 \pm 0.0304$	$1.0272 \pm 0.0101 \pm 0.0536$
0.25	$0.6915 \pm 0.0081 \pm 0.0098$	$1.1118 \pm 0.0108 \pm 0.0808$
0.35	$0.6454 \pm 0.0076 \pm 0.0737$	$1.1585 \pm 0.0112 \pm 0.0240$
0.45	$0.7138 \pm 0.0083 \pm 0.0915$	$1.1892 \pm 0.0116 \pm 0.0067$
0.55	$0.7934 \pm 0.0089 \pm 0.0419$	$1.1315 \pm 0.0108 \pm 0.0989$
0.65	$0.8361 \pm 0.0093 \pm 0.0587$	$1.2206 \pm 0.0119 \pm 0.0094$
0.75	$0.7367 \pm 0.0083 \pm 0.0259$	$1.3732 \pm 0.0132 \pm 0.1115$
0.85	$0.7833 \pm 0.0088 \pm 0.0338$	$1.2943 \pm 0.0125 \pm 0.1560$
0.95	$0.8675 \pm 0.0094 \pm 0.0379$	$1.2776 \pm 0.0123 \pm 0.0162$

 Table B.3: $\frac{d\sigma}{d\Omega}$, in $\mu\text{b/sr}$, for $E_\gamma = 718$ and 747 MeV from the $\eta \rightarrow 2\gamma$ decay mode.

$\cos\theta_\eta^*$	$E_\gamma = 778 \text{ MeV}$	$E_\gamma = 805 \text{ MeV}$
	$\frac{d\sigma}{d\Omega} \pm \Delta \left(\frac{d\sigma}{d\Omega} \right)_{stat.} \pm \Delta \left(\frac{d\sigma}{d\Omega} \right)_{sys.}$	$\frac{d\sigma}{d\Omega} \pm \Delta \left(\frac{d\sigma}{d\Omega} \right)_{stat.} \pm \Delta \left(\frac{d\sigma}{d\Omega} \right)_{sys.}$
-0.95	$0.9870 \pm 0.0099 \pm 0.1068$	$0.8877 \pm 0.0088 \pm 0.0338$
-0.85	$0.9974 \pm 0.0098 \pm 0.0249$	$0.9915 \pm 0.0095 \pm 0.0370$
-0.75	$0.9552 \pm 0.0096 \pm 0.1062$	$0.9816 \pm 0.0094 \pm 0.0424$
-0.65	$1.0788 \pm 0.0108 \pm 0.0283$	$1.0273 \pm 0.0099 \pm 0.0435$
-0.55	$1.1692 \pm 0.0118 \pm 0.1870$	$1.1159 \pm 0.0108 \pm 0.1018$
-0.45	$1.0682 \pm 0.0110 \pm 0.0295$	$1.0211 \pm 0.0099 \pm 0.1301$
-0.35	$1.0442 \pm 0.0105 \pm 0.0837$	$1.2251 \pm 0.0119 \pm 0.1575$
-0.25	$1.2108 \pm 0.0123 \pm 0.0356$	$1.1454 \pm 0.0111 \pm 0.0625$
-0.15	$1.0337 \pm 0.0109 \pm 0.0470$	$1.1779 \pm 0.0113 \pm 0.0556$
-0.05	$1.1733 \pm 0.0117 \pm 0.0429$	$1.1960 \pm 0.0116 \pm 0.0748$
0.05	$1.1166 \pm 0.0116 \pm 0.0084$	$1.2630 \pm 0.0123 \pm 0.0385$
0.15	$1.2379 \pm 0.0126 \pm 0.0050$	$1.1851 \pm 0.0116 \pm 0.0283$
0.25	$1.1656 \pm 0.0119 \pm 0.0605$	$1.2123 \pm 0.0119 \pm 0.1110$
0.35	$1.3066 \pm 0.0133 \pm 0.0213$	$1.1261 \pm 0.0112 \pm 0.0957$
0.45	$1.0523 \pm 0.0114 \pm 0.0506$	$1.2177 \pm 0.0123 \pm 0.1824$
0.55	$1.4019 \pm 0.0145 \pm 0.0971$	$1.2658 \pm 0.0129 \pm 0.1034$
0.65	$1.3032 \pm 0.0135 \pm 0.0399$	$1.1014 \pm 0.0114 \pm 0.1051$
0.75	$1.3957 \pm 0.0146 \pm 0.0812$	$1.2936 \pm 0.0134 \pm 0.1046$
0.85	$1.2567 \pm 0.0132 \pm 0.0640$	$1.2250 \pm 0.0129 \pm 0.0540$
0.95	$1.2398 \pm 0.0134 \pm 0.1198$	$1.2010 \pm 0.0129 \pm 0.0213$
0.95	$1.2398 \pm 0.0134 \pm 0.7051$	$1.2010 \pm 0.0129 \pm 0.0169$

 Table B.4: $\frac{d\sigma}{d\Omega}$, in $\mu\text{b}/\text{sr}$, for $E_\gamma = 788$ and 805 MeV from the $\eta \rightarrow 2\gamma$ decay mode.

$\cos\theta_\eta^*$	$E_\gamma = 833$ MeV	$E_\gamma = 863$ MeV
	$\frac{d\sigma}{d\Omega} \pm \Delta\left(\frac{d\sigma}{d\Omega}\right)_{stat.} \pm \Delta\left(\frac{d\sigma}{d\Omega}\right)_{sys.}$	$\frac{d\sigma}{d\Omega} \pm \Delta\left(\frac{d\sigma}{d\Omega}\right)_{stat.} \pm \Delta\left(\frac{d\sigma}{d\Omega}\right)_{sys.}$
-0.95	0.8511 \pm 0.0088 \pm 0.0317	0.7572 \pm 0.0086 \pm 0.0183
-0.85	0.9157 \pm 0.0094 \pm 0.0131	0.7983 \pm 0.0089 \pm 0.0021
-0.75	0.9575 \pm 0.0098 \pm 0.0299	0.8471 \pm 0.0093 \pm 0.0284
-0.65	0.9905 \pm 0.0102 \pm 0.1428	0.9164 \pm 0.0102 \pm 0.1666
-0.55	1.0508 \pm 0.0108 \pm 0.0891	0.9581 \pm 0.0105 \pm 0.0296
-0.45	1.0205 \pm 0.0106 \pm 0.0469	0.8969 \pm 0.0102 \pm 0.1709
-0.35	1.0441 \pm 0.0108 \pm 0.0467	0.9490 \pm 0.0104 \pm 0.0776
-0.25	1.0776 \pm 0.0112 \pm 0.0383	0.9637 \pm 0.0108 \pm 0.0471
-0.15	1.0202 \pm 0.0106 \pm 0.1220	0.9496 \pm 0.0107 \pm 0.0123
-0.05	1.0881 \pm 0.0113 \pm 0.0866	1.0235 \pm 0.0114 \pm 0.0106
0.05	1.1289 \pm 0.0118 \pm 0.0653	0.9642 \pm 0.0110 \pm 0.0299
0.15	1.1121 \pm 0.0118 \pm 0.0866	0.7420 \pm 0.0093 \pm 0.0351
0.25	1.0547 \pm 0.0112 \pm 0.0465	0.8849 \pm 0.0106 \pm 0.0066
0.35	1.0132 \pm 0.0110 \pm 0.0652	0.7531 \pm 0.0096 \pm 0.0243
0.45	1.0490 \pm 0.0116 \pm 0.1025	0.8385 \pm 0.0107 \pm 0.0472
0.55	1.0389 \pm 0.0117 \pm 0.0227	0.8879 \pm 0.0112 \pm 0.0017
0.65	0.9713 \pm 0.0111 \pm 0.0758	0.8209 \pm 0.0108 \pm 0.0224
0.75	0.9051 \pm 0.0111 \pm 0.0348	0.6994 \pm 0.0098 \pm 0.0370
0.85	1.0707 \pm 0.0128 \pm 0.0217	0.7703 \pm 0.0109 \pm 0.0039
0.95	1.0176 \pm 0.0125 \pm 0.0132	0.7243 \pm 0.0108 \pm 0.0158

 Table B.5: $\frac{d\sigma}{d\Omega}$, in $\mu\text{b/sr}$, for $E_\gamma = 833$ and 863 MeV from the $\eta \rightarrow 2\gamma$ decay mode.

$\cos\theta_\eta^*$	$E_\gamma = 890 \text{ MeV}$	$E_\gamma = 918 \text{ MeV}$
	$\frac{d\sigma}{d\Omega} \pm \Delta \left(\frac{d\sigma}{d\Omega} \right)_{stat.} \pm \Delta \left(\frac{d\sigma}{d\Omega} \right)_{sys.}$	$\frac{d\sigma}{d\Omega} \pm \Delta \left(\frac{d\sigma}{d\Omega} \right)_{stat.} \pm \Delta \left(\frac{d\sigma}{d\Omega} \right)_{sys.}$
-0.95	$0.6241 \pm 0.0077 \pm 0.1498$	$0.5648 \pm 0.0075 \pm 0.0285$
-0.85	$0.6987 \pm 0.0083 \pm 0.0707$	$0.5853 \pm 0.0075 \pm 0.0622$
-0.75	$0.6975 \pm 0.0084 \pm 0.0072$	$0.6049 \pm 0.0077 \pm 0.0353$
-0.65	$0.7519 \pm 0.0090 \pm 0.0889$	$0.6692 \pm 0.0086 \pm 0.0389$
-0.55	$0.8261 \pm 0.0098 \pm 0.0185$	$0.6355 \pm 0.0082 \pm 0.0199$
-0.45	$0.8389 \pm 0.0100 \pm 0.0139$	$0.6901 \pm 0.0088 \pm 0.0292$
-0.35	$0.7896 \pm 0.0097 \pm 0.0171$	$0.6617 \pm 0.0087 \pm 0.0119$
-0.25	$0.7589 \pm 0.0092 \pm 0.0378$	$0.6176 \pm 0.0082 \pm 0.0229$
-0.15	$0.8323 \pm 0.0101 \pm 0.0405$	$0.6868 \pm 0.0090 \pm 0.0331$
-0.05	$0.8509 \pm 0.0104 \pm 0.0521$	$0.6757 \pm 0.0089 \pm 0.0335$
0.05	$0.7913 \pm 0.0099 \pm 0.0223$	$0.7170 \pm 0.0097 \pm 0.0539$
0.15	$0.7968 \pm 0.0100 \pm 0.0330$	$0.5733 \pm 0.0080 \pm 0.0374$
0.25	$0.7434 \pm 0.0096 \pm 0.0030$	$0.5743 \pm 0.0084 \pm 0.0262$
0.35	$0.7471 \pm 0.0099 \pm 0.0716$	$0.5751 \pm 0.0085 \pm 0.0861$
0.45	$0.7491 \pm 0.0100 \pm 0.0137$	$0.5677 \pm 0.0087 \pm 0.0570$
0.55	$0.7261 \pm 0.0104 \pm 0.0307$	$0.5161 \pm 0.0084 \pm 0.0414$
0.65	$0.6563 \pm 0.0099 \pm 0.0984$	$0.4891 \pm 0.0084 \pm 0.0682$
0.75	$0.6181 \pm 0.0099 \pm 0.0600$	$0.4144 \pm 0.0076 \pm 0.0465$
0.85	$0.5902 \pm 0.0097 \pm 0.0210$	$0.4149 \pm 0.0081 \pm 0.0530$
0.95	$0.6320 \pm 0.0106 \pm 0.0474$	$0.4387 \pm 0.0090 \pm 0.0893$
0.95	$0.6320 \pm 0.0106 \pm 0.0299$	$0.4387 \pm 0.0090 \pm 0.0000$

 Table B.6: $\frac{d\sigma}{d\Omega}$, in $\mu\text{b/sr}$, for $E_\gamma = 890$ and 918 MeV from the $\eta \rightarrow 2\gamma$ decay mode.

$\cos\theta_\eta^*$	$E_\gamma = 945 \text{ MeV}$	$E_\gamma = 972 \text{ MeV}$
	$\frac{d\sigma}{d\Omega} \pm \Delta\left(\frac{d\sigma}{d\Omega}\right)_{stat.} \pm \Delta\left(\frac{d\sigma}{d\Omega}\right)_{sys.}$	$\frac{d\sigma}{d\Omega} \pm \Delta\left(\frac{d\sigma}{d\Omega}\right)_{stat.} \pm \Delta\left(\frac{d\sigma}{d\Omega}\right)_{sys.}$
-0.95	$0.4197 \pm 0.0063 \pm 0.0169$	$0.2796 \pm 0.0050 \pm 0.0065$
-0.85	$0.4661 \pm 0.0068 \pm 0.0020$	$0.3816 \pm 0.0063 \pm 0.0314$
-0.75	$0.5084 \pm 0.0073 \pm 0.0253$	$0.3687 \pm 0.0062 \pm 0.0108$
-0.65	$0.4929 \pm 0.0074 \pm 0.0147$	$0.4350 \pm 0.0069 \pm 0.0078$
-0.55	$0.5120 \pm 0.0077 \pm 0.0279$	$0.4108 \pm 0.0068 \pm 0.0495$
-0.45	$0.5384 \pm 0.0079 \pm 0.0544$	$0.4251 \pm 0.0070 \pm 0.0085$
-0.35	$0.5219 \pm 0.0077 \pm 0.0289$	$0.3892 \pm 0.0067 \pm 0.0289$
-0.25	$0.5229 \pm 0.0077 \pm 0.0098$	$0.4411 \pm 0.0075 \pm 0.0298$
-0.15	$0.5428 \pm 0.0081 \pm 0.0245$	$0.3684 \pm 0.0065 \pm 0.0352$
-0.05	$0.4295 \pm 0.0069 \pm 0.0389$	$0.3697 \pm 0.0067 \pm 0.0485$
0.05	$0.5318 \pm 0.0085 \pm 0.0975$	$0.3681 \pm 0.0067 \pm 0.0224$
0.15	$0.4536 \pm 0.0074 \pm 0.0252$	$0.3825 \pm 0.0069 \pm 0.0163$
0.25	$0.4480 \pm 0.0075 \pm 0.0241$	$0.3488 \pm 0.0067 \pm 0.0342$
0.35	$0.4220 \pm 0.0075 \pm 0.0526$	$0.3351 \pm 0.0067 \pm 0.0159$
0.45	$0.3713 \pm 0.0069 \pm 0.0383$	$0.2928 \pm 0.0063 \pm 0.0063$
0.55	$0.4064 \pm 0.0078 \pm 0.0362$	$0.2735 \pm 0.0064 \pm 0.0346$
0.65	$0.3078 \pm 0.0068 \pm 0.0578$	$0.2732 \pm 0.0065 \pm 0.0230$
0.75	$0.2864 \pm 0.0068 \pm 0.0312$	$0.1940 \pm 0.0058 \pm 0.0039$
0.85	$0.2907 \pm 0.0075 \pm 0.1115$	$0.1171 \pm 0.0045 \pm 0.0155$
0.95	$0.2489 \pm 0.0071 \pm 0.0334$	$0.1439 \pm 0.0055 \pm 0.0059$

 Table B.7: $\frac{d\sigma}{d\Omega}$, in $\mu\text{b/sr}$, for $E_\gamma = 945$ and 972 MeV from the $\eta \rightarrow 2\gamma$ decay mode.

$\cos\theta_\eta^*$	$E_\gamma = 999 \text{ MeV}$	$E_\gamma = 1024 \text{ MeV}$
	$\frac{d\sigma}{d\Omega} \pm \Delta\left(\frac{d\sigma}{d\Omega}\right)_{stat.} \pm \Delta\left(\frac{d\sigma}{d\Omega}\right)_{sys.}$	$\frac{d\sigma}{d\Omega} \pm \Delta\left(\frac{d\sigma}{d\Omega}\right)_{stat.} \pm \Delta\left(\frac{d\sigma}{d\Omega}\right)_{sys.}$
-0.95	$0.1944 \pm 0.0045 \pm 0.0074$	$0.1378 \pm 0.0037 \pm 0.0037$
-0.85	$0.2633 \pm 0.0055 \pm 0.0268$	$0.1945 \pm 0.0046 \pm 0.0066$
-0.75	$0.2738 \pm 0.0056 \pm 0.0165$	$0.2518 \pm 0.0054 \pm 0.0173$
-0.65	$0.2945 \pm 0.0060 \pm 0.0295$	$0.2508 \pm 0.0055 \pm 0.0189$
-0.55	$0.2845 \pm 0.0060 \pm 0.0137$	$0.2304 \pm 0.0052 \pm 0.0538$
-0.45	$0.3228 \pm 0.0064 \pm 0.0094$	$0.2457 \pm 0.0056 \pm 0.0177$
-0.35	$0.3233 \pm 0.0067 \pm 0.0273$	$0.2579 \pm 0.0056 \pm 0.0212$
-0.25	$0.2848 \pm 0.0061 \pm 0.0180$	$0.2818 \pm 0.0060 \pm 0.0114$
-0.15	$0.2983 \pm 0.0063 \pm 0.0187$	$0.2699 \pm 0.0059 \pm 0.0083$
-0.05	$0.3110 \pm 0.0063 \pm 0.0193$	$0.2658 \pm 0.0060 \pm 0.0385$
0.05	$0.2918 \pm 0.0064 \pm 0.0187$	$0.2352 \pm 0.0056 \pm 0.0247$
0.15	$0.2688 \pm 0.0062 \pm 0.0078$	$0.2377 \pm 0.0056 \pm 0.0124$
0.25	$0.2454 \pm 0.0059 \pm 0.0056$	$0.2531 \pm 0.0059 \pm 0.0051$
0.35	$0.2351 \pm 0.0058 \pm 0.0062$	$0.2726 \pm 0.0065 \pm 0.0145$
0.45	$0.2749 \pm 0.0068 \pm 0.0186$	$0.2247 \pm 0.0058 \pm 0.0204$
0.55	$0.2272 \pm 0.0061 \pm 0.0079$	$0.2337 \pm 0.0064 \pm 0.0130$
0.65	$0.2042 \pm 0.0062 \pm 0.0199$	$0.2266 \pm 0.0067 \pm 0.0215$
0.75	$0.1476 \pm 0.0055 \pm 0.0027$	$0.1708 \pm 0.0060 \pm 0.0131$
0.85	$0.0994 \pm 0.0048 \pm 0.0077$	$0.1255 \pm 0.0055 \pm 0.0220$
0.95	$0.0388 \pm 0.0031 \pm 0.0126$	$0.0488 \pm 0.0035 \pm 0.0189$

 Table B.8: $\frac{d\sigma}{d\Omega}$, in $\mu\text{b}/\text{sr}$, for $E_\gamma = 999$ and 1024 MeV from the $\eta \rightarrow 2\gamma$ decay mode.

$\cos\theta_\eta^*$	$E_\gamma = 1050 \text{ MeV}$	$E_\gamma = 1075 \text{ MeV}$
	$\frac{d\sigma}{d\Omega} \pm \Delta\left(\frac{d\sigma}{d\Omega}\right)_{stat.} \pm \Delta\left(\frac{d\sigma}{d\Omega}\right)_{sys.}$	$\frac{d\sigma}{d\Omega} \pm \Delta\left(\frac{d\sigma}{d\Omega}\right)_{stat.} \pm \Delta\left(\frac{d\sigma}{d\Omega}\right)_{sys.}$
-0.95	$0.1354 \pm 0.0038 \pm 0.0098$	$0.0889 \pm 0.0031 \pm 0.0019$
-0.85	$0.1679 \pm 0.0044 \pm 0.0242$	$0.1372 \pm 0.0040 \pm 0.0217$
-0.75	$0.1716 \pm 0.0046 \pm 0.0044$	$0.1852 \pm 0.0049 \pm 0.0122$
-0.65	$0.2244 \pm 0.0052 \pm 0.0358$	$0.2056 \pm 0.0052 \pm 0.0153$
-0.55	$0.2329 \pm 0.0058 \pm 0.0328$	$0.2260 \pm 0.0056 \pm 0.0246$
-0.45	$0.2294 \pm 0.0055 \pm 0.0102$	$0.2085 \pm 0.0053 \pm 0.0090$
-0.35	$0.2099 \pm 0.0053 \pm 0.0246$	$0.2464 \pm 0.0059 \pm 0.0336$
-0.25	$0.2435 \pm 0.0057 \pm 0.0166$	$0.2483 \pm 0.0057 \pm 0.0178$
-0.15	$0.2432 \pm 0.0058 \pm 0.0252$	$0.2559 \pm 0.0060 \pm 0.0049$
-0.05	$0.2397 \pm 0.0059 \pm 0.0043$	$0.2887 \pm 0.0065 \pm 0.0227$
0.05	$0.2873 \pm 0.0065 \pm 0.0132$	$0.2753 \pm 0.0061 \pm 0.0148$
0.15	$0.2052 \pm 0.0052 \pm 0.0094$	$0.3042 \pm 0.0066 \pm 0.0079$
0.25	$0.2282 \pm 0.0057 \pm 0.0096$	$0.2847 \pm 0.0066 \pm 0.0181$
0.35	$0.2440 \pm 0.0062 \pm 0.0160$	$0.2645 \pm 0.0062 \pm 0.0362$
0.45	$0.2546 \pm 0.0064 \pm 0.0213$	$0.3421 \pm 0.0079 \pm 0.0239$
0.55	$0.2501 \pm 0.0068 \pm 0.0200$	$0.2878 \pm 0.0075 \pm 0.0196$
0.65	$0.2241 \pm 0.0068 \pm 0.0116$	$0.3206 \pm 0.0080 \pm 0.0223$
0.75	$0.2196 \pm 0.0073 \pm 0.0182$	$0.2658 \pm 0.0082 \pm 0.0434$
0.85	$0.1270 \pm 0.0057 \pm 0.0254$	$0.2022 \pm 0.0075 \pm 0.0610$
0.95	$0.1048 \pm 0.0056 \pm 0.0263$	$0.1516 \pm 0.0069 \pm 0.0369$

 Table B.9: $\frac{d\sigma}{d\Omega}$, in $\mu\text{b}/\text{sr}$, for $E_\gamma = 1050$ and 1075 MeV from the $\eta \rightarrow 2\gamma$ decay mode.

$\cos\theta_\eta^*$	$E_\gamma = 1100 \text{ MeV}$	$E_\gamma = 1124 \text{ MeV}$
	$\frac{d\sigma}{d\Omega} \pm \Delta\left(\frac{d\sigma}{d\Omega}\right)_{stat.} \pm \Delta\left(\frac{d\sigma}{d\Omega}\right)_{sys.}$	$\frac{d\sigma}{d\Omega} \pm \Delta\left(\frac{d\sigma}{d\Omega}\right)_{stat.} \pm \Delta\left(\frac{d\sigma}{d\Omega}\right)_{sys.}$
-0.95	$0.0755 \pm 0.0030 \pm 0.0020$	$0.0646 \pm 0.0028 \pm 0.0020$
-0.85	$0.1204 \pm 0.0038 \pm 0.0164$	$0.1060 \pm 0.0037 \pm 0.0075$
-0.75	$0.1347 \pm 0.0041 \pm 0.0047$	$0.1271 \pm 0.0041 \pm 0.0138$
-0.65	$0.1757 \pm 0.0049 \pm 0.0331$	$0.1258 \pm 0.0043 \pm 0.0080$
-0.55	$0.1875 \pm 0.0051 \pm 0.0074$	$0.1968 \pm 0.0053 \pm 0.0434$
-0.45	$0.2135 \pm 0.0055 \pm 0.0170$	$0.1564 \pm 0.0047 \pm 0.0208$
-0.35	$0.2409 \pm 0.0060 \pm 0.0120$	$0.2028 \pm 0.0056 \pm 0.0039$
-0.25	$0.2386 \pm 0.0058 \pm 0.0225$	$0.2577 \pm 0.0064 \pm 0.0153$
-0.15	$0.2562 \pm 0.0063 \pm 0.0236$	$0.2332 \pm 0.0059 \pm 0.0191$
-0.05	$0.2733 \pm 0.0064 \pm 0.0036$	$0.2764 \pm 0.0068 \pm 0.0382$
0.05	$0.2870 \pm 0.0065 \pm 0.0205$	$0.2711 \pm 0.0067 \pm 0.0019$
0.15	$0.3154 \pm 0.0072 \pm 0.0207$	$0.3027 \pm 0.0071 \pm 0.0264$
0.25	$0.3248 \pm 0.0073 \pm 0.0177$	$0.3017 \pm 0.0073 \pm 0.0106$
0.35	$0.2795 \pm 0.0068 \pm 0.0078$	$0.3069 \pm 0.0075 \pm 0.0281$
0.45	$0.3583 \pm 0.0084 \pm 0.0116$	$0.3026 \pm 0.0079 \pm 0.0265$
0.55	$0.2948 \pm 0.0074 \pm 0.0195$	$0.3068 \pm 0.0079 \pm 0.0049$
0.65	$0.3221 \pm 0.0085 \pm 0.0114$	$0.2488 \pm 0.0078 \pm 0.0082$
0.75	$0.2528 \pm 0.0080 \pm 0.0251$	$0.3171 \pm 0.0096 \pm 0.0258$
0.85	$0.2538 \pm 0.0092 \pm 0.0451$	$0.1696 \pm 0.0077 \pm 0.0110$
0.95	$0.1722 \pm 0.0080 \pm 0.0371$	$0.1505 \pm 0.0080 \pm 0.0498$

Table B.10: $\frac{d\sigma}{d\Omega}$, in $\mu\text{b}/\text{sr}$, for $E_\gamma = 1100$ and 1124 MeV from the $\eta \rightarrow 2\gamma$ decay mode.

$\cos\theta_\eta^*$	$E_\gamma = 1147 \text{ MeV}$	$E_\gamma = 1171 \text{ MeV}$
	$\frac{d\sigma}{d\Omega} \pm \Delta\left(\frac{d\sigma}{d\Omega}\right)_{stat.} \pm \Delta\left(\frac{d\sigma}{d\Omega}\right)_{sys.}$	$\frac{d\sigma}{d\Omega} \pm \Delta\left(\frac{d\sigma}{d\Omega}\right)_{stat.} \pm \Delta\left(\frac{d\sigma}{d\Omega}\right)_{sys.}$
-0.95	$0.0487 \pm 0.0024 \pm 0.0327$	$0.0720 \pm 0.0031 \pm 0.0060$
-0.85	$0.0761 \pm 0.0033 \pm 0.0096$	$0.0884 \pm 0.0035 \pm 0.0073$
-0.75	$0.1208 \pm 0.0042 \pm 0.0120$	$0.0928 \pm 0.0037 \pm 0.0075$
-0.65	$0.1289 \pm 0.0043 \pm 0.0039$	$0.1216 \pm 0.0043 \pm 0.0233$
-0.55	$0.1745 \pm 0.0051 \pm 0.0108$	$0.1316 \pm 0.0047 \pm 0.0102$
-0.45	$0.1732 \pm 0.0052 \pm 0.0143$	$0.1470 \pm 0.0049 \pm 0.0034$
-0.35	$0.2023 \pm 0.0058 \pm 0.0069$	$0.1748 \pm 0.0054 \pm 0.0030$
-0.25	$0.2528 \pm 0.0067 \pm 0.0203$	$0.2229 \pm 0.0061 \pm 0.0069$
-0.15	$0.2323 \pm 0.0061 \pm 0.0149$	$0.2566 \pm 0.0069 \pm 0.0077$
-0.05	$0.2619 \pm 0.0066 \pm 0.0016$	$0.2261 \pm 0.0062 \pm 0.0076$
0.05	$0.2745 \pm 0.0067 \pm 0.0126$	$0.2449 \pm 0.0066 \pm 0.0075$
0.15	$0.2529 \pm 0.0065 \pm 0.0315$	$0.2764 \pm 0.0074 \pm 0.0194$
0.25	$0.2778 \pm 0.0074 \pm 0.0094$	$0.2954 \pm 0.0074 \pm 0.0061$
0.35	$0.3041 \pm 0.0078 \pm 0.0136$	$0.2917 \pm 0.0078 \pm 0.0111$
0.45	$0.3143 \pm 0.0082 \pm 0.0416$	$0.2384 \pm 0.0068 \pm 0.0109$
0.55	$0.2998 \pm 0.0083 \pm 0.0219$	$0.2842 \pm 0.0084 \pm 0.0189$
0.65	$0.2715 \pm 0.0083 \pm 0.0060$	$0.2543 \pm 0.0083 \pm 0.0144$
0.75	$0.2294 \pm 0.0084 \pm 0.0157$	$0.2846 \pm 0.0100 \pm 0.0064$
0.85	$0.1423 \pm 0.0070 \pm 0.0140$	$0.1763 \pm 0.0082 \pm 0.0200$
0.95	$0.1044 \pm 0.0070 \pm 0.0478$	$0.1957 \pm 0.0101 \pm 0.0608$

Table B.11: $\frac{d\sigma}{d\Omega}$, in $\mu\text{b}/\text{sr}$, for $E_\gamma = 1147$ and 1171 MeV from the $\eta \rightarrow 2\gamma$ decay mode.

$\cos\theta_\eta^*$	$E_\gamma = 1193 \text{ MeV}$	$E_\gamma = 1215 \text{ MeV}$
	$\frac{d\sigma}{d\Omega} \pm \Delta\left(\frac{d\sigma}{d\Omega}\right)_{stat.} \pm \Delta\left(\frac{d\sigma}{d\Omega}\right)_{sys.}$	$\frac{d\sigma}{d\Omega} \pm \Delta\left(\frac{d\sigma}{d\Omega}\right)_{stat.} \pm \Delta\left(\frac{d\sigma}{d\Omega}\right)_{sys.}$
-0.95	$0.0207 \pm 0.0017 \pm 0.0066$	$0.0471 \pm 0.0027 \pm 0.0296$
-0.85	$0.0664 \pm 0.0032 \pm 0.0134$	$0.0691 \pm 0.0032 \pm 0.0041$
-0.75	$0.0977 \pm 0.0039 \pm 0.0166$	$0.0994 \pm 0.0040 \pm 0.0037$
-0.65	$0.0995 \pm 0.0040 \pm 0.0120$	$0.1295 \pm 0.0047 \pm 0.0378$
-0.55	$0.1209 \pm 0.0044 \pm 0.0286$	$0.1228 \pm 0.0047 \pm 0.0013$
-0.45	$0.1661 \pm 0.0055 \pm 0.0063$	$0.1113 \pm 0.0045 \pm 0.0051$
-0.35	$0.1622 \pm 0.0054 \pm 0.0046$	$0.1608 \pm 0.0055 \pm 0.0044$
-0.25	$0.2149 \pm 0.0065 \pm 0.0057$	$0.1947 \pm 0.0062 \pm 0.0175$
-0.15	$0.1985 \pm 0.0059 \pm 0.0105$	$0.1823 \pm 0.0058 \pm 0.0064$
-0.05	$0.2345 \pm 0.0067 \pm 0.0118$	$0.2055 \pm 0.0063 \pm 0.0167$
0.05	$0.2475 \pm 0.0069 \pm 0.0038$	$0.2659 \pm 0.0074 \pm 0.0076$
0.15	$0.2523 \pm 0.0069 \pm 0.0166$	$0.2624 \pm 0.0075 \pm 0.0120$
0.25	$0.2540 \pm 0.0072 \pm 0.0091$	$0.2431 \pm 0.0072 \pm 0.0055$
0.35	$0.2630 \pm 0.0074 \pm 0.0102$	$0.2902 \pm 0.0084 \pm 0.0162$
0.45	$0.2680 \pm 0.0079 \pm 0.0060$	$0.2544 \pm 0.0080 \pm 0.0130$
0.55	$0.2024 \pm 0.0072 \pm 0.0117$	$0.2356 \pm 0.0079 \pm 0.0079$
0.65	$0.2690 \pm 0.0092 \pm 0.0270$	$0.2350 \pm 0.0087 \pm 0.0037$
0.75	$0.2624 \pm 0.0098 \pm 0.0253$	$0.2763 \pm 0.0103 \pm 0.0171$
0.85	$0.1755 \pm 0.0093 \pm 0.0192$	$0.1890 \pm 0.0095 \pm 0.0179$
0.95	$0.0765 \pm 0.0067 \pm 0.0064$	$0.1299 \pm 0.0085 \pm 0.0291$

Table B.12: $\frac{d\sigma}{d\Omega}$, in $\mu\text{b}/\text{sr}$, for $E_\gamma = 1193$ and 1215 MeV from the $\eta \rightarrow 2\gamma$ decay mode.

$\cos\theta_\eta^*$	$E_\gamma = 1236 \text{ MeV}$	$E_\gamma = 1257 \text{ MeV}$
	$\frac{d\sigma}{d\Omega} \pm \Delta\left(\frac{d\sigma}{d\Omega}\right)_{stat.} \pm \Delta\left(\frac{d\sigma}{d\Omega}\right)_{sys.}$	$\frac{d\sigma}{d\Omega} \pm \Delta\left(\frac{d\sigma}{d\Omega}\right)_{stat.} \pm \Delta\left(\frac{d\sigma}{d\Omega}\right)_{sys.}$
-0.95	$0.0392 \pm 0.0025 \pm 0.0226$	$0.0623 \pm 0.0032 \pm 0.0632$
-0.85	$0.0807 \pm 0.0036 \pm 0.0188$	$0.0690 \pm 0.0034 \pm 0.0049$
-0.75	$0.0732 \pm 0.0035 \pm 0.0071$	$0.0953 \pm 0.0042 \pm 0.0143$
-0.65	$0.1053 \pm 0.0044 \pm 0.0100$	$0.1013 \pm 0.0043 \pm 0.0077$
-0.55	$0.1239 \pm 0.0047 \pm 0.0105$	$0.1256 \pm 0.0050 \pm 0.0061$
-0.45	$0.1393 \pm 0.0052 \pm 0.0015$	$0.1419 \pm 0.0054 \pm 0.0138$
-0.35	$0.1754 \pm 0.0059 \pm 0.0044$	$0.1712 \pm 0.0061 \pm 0.0168$
-0.25	$0.1945 \pm 0.0063 \pm 0.0114$	$0.1678 \pm 0.0061 \pm 0.0117$
-0.15	$0.1784 \pm 0.0060 \pm 0.0174$	$0.1927 \pm 0.0065 \pm 0.0150$
-0.05	$0.2143 \pm 0.0069 \pm 0.0145$	$0.2061 \pm 0.0067 \pm 0.0111$
0.05	$0.2364 \pm 0.0071 \pm 0.0131$	$0.2137 \pm 0.0068 \pm 0.0064$
0.15	$0.2720 \pm 0.0079 \pm 0.0100$	$0.2243 \pm 0.0071 \pm 0.0207$
0.25	$0.2668 \pm 0.0079 \pm 0.0078$	$0.2194 \pm 0.0072 \pm 0.0048$
0.35	$0.2781 \pm 0.0084 \pm 0.0120$	$0.2839 \pm 0.0086 \pm 0.0071$
0.45	$0.2018 \pm 0.0072 \pm 0.0191$	$0.1990 \pm 0.0074 \pm 0.0242$
0.55	$0.1903 \pm 0.0075 \pm 0.0052$	$0.2461 \pm 0.0087 \pm 0.0113$
0.65	$0.2205 \pm 0.0085 \pm 0.0290$	$0.2049 \pm 0.0088 \pm 0.0188$
0.75	$0.2635 \pm 0.0109 \pm 0.0343$	$0.1774 \pm 0.0087 \pm 0.0220$
0.85	$0.2405 \pm 0.0118 \pm 0.0316$	$0.1129 \pm 0.0084 \pm 0.0137$
0.95	$0.1425 \pm 0.0098 \pm 0.0303$	$0.1741 \pm 0.0122 \pm 0.0140$

Table B.13: $\frac{d\sigma}{d\Omega}$, in $\mu\text{b}/\text{sr}$, for $E_\gamma = 1236$ and 1257 MeV from the $\eta \rightarrow 2\gamma$ decay mode.

$\cos\theta_\eta^*$	$E_\gamma = 1277 \text{ MeV}$	$E_\gamma = 1297 \text{ MeV}$
	$\frac{d\sigma}{d\Omega} \pm \Delta\left(\frac{d\sigma}{d\Omega}\right)_{stat.} \pm \Delta\left(\frac{d\sigma}{d\Omega}\right)_{sys.}$	$\frac{d\sigma}{d\Omega} \pm \Delta\left(\frac{d\sigma}{d\Omega}\right)_{stat.} \pm \Delta\left(\frac{d\sigma}{d\Omega}\right)_{sys.}$
-0.95	$0.0183 \pm 0.0017 \pm 0.0093$	$0.0487 \pm 0.0031 \pm 0.0198$
-0.85	$0.0550 \pm 0.0031 \pm 0.0137$	$0.0382 \pm 0.0027 \pm 0.0041$
-0.75	$0.0893 \pm 0.0040 \pm 0.0123$	$0.0478 \pm 0.0033 \pm 0.0024$
-0.65	$0.1004 \pm 0.0041 \pm 0.0077$	$0.0815 \pm 0.0044 \pm 0.0055$
-0.55	$0.1294 \pm 0.0049 \pm 0.0016$	$0.1242 \pm 0.0054 \pm 0.0090$
-0.45	$0.1458 \pm 0.0056 \pm 0.0130$	$0.1199 \pm 0.0055 \pm 0.0036$
-0.35	$0.1458 \pm 0.0054 \pm 0.0126$	$0.1052 \pm 0.0052 \pm 0.0050$
-0.25	$0.1515 \pm 0.0055 \pm 0.0036$	$0.1440 \pm 0.0061 \pm 0.0138$
-0.15	$0.1778 \pm 0.0059 \pm 0.0110$	$0.1779 \pm 0.0072 \pm 0.0046$
-0.05	$0.2100 \pm 0.0067 \pm 0.0171$	$0.1830 \pm 0.0068 \pm 0.0057$
0.05	$0.1879 \pm 0.0062 \pm 0.0168$	$0.2186 \pm 0.0078 \pm 0.0072$
0.15	$0.2129 \pm 0.0070 \pm 0.0203$	$0.2553 \pm 0.0088 \pm 0.0100$
0.25	$0.2823 \pm 0.0083 \pm 0.0019$	$0.2033 \pm 0.0078 \pm 0.0040$
0.35	$0.2121 \pm 0.0073 \pm 0.0141$	$0.2168 \pm 0.0083 \pm 0.0321$
0.45	$0.2297 \pm 0.0080 \pm 0.0204$	$0.2405 \pm 0.0096 \pm 0.0217$
0.55	$0.2160 \pm 0.0084 \pm 0.0102$	$0.2005 \pm 0.0090 \pm 0.0109$
0.65	$0.1959 \pm 0.0084 \pm 0.0024$	$0.1694 \pm 0.0085 \pm 0.0089$
0.75	$0.1170 \pm 0.0073 \pm 0.0184$	$0.1686 \pm 0.0100 \pm 0.0204$
0.85	$0.1412 \pm 0.0088 \pm 0.0337$	$0.1766 \pm 0.0114 \pm 0.0358$
0.95	$0.1372 \pm 0.0098 \pm 0.0048$	$0.1117 \pm 0.0108 \pm 0.0910$

Table B.14: $\frac{d\sigma}{d\Omega}$, in $\mu\text{b}/\text{sr}$, for $E_\gamma = 1277$ and 1297 MeV from the $\eta \rightarrow 2\gamma$ decay mode.

$\cos\theta_\eta^*$	$E_\gamma = 1315$ MeV	$E_\gamma = 1338$ MeV
	$\frac{d\sigma}{d\Omega} \pm \Delta\left(\frac{d\sigma}{d\Omega}\right)_{stat.} \pm \Delta\left(\frac{d\sigma}{d\Omega}\right)_{sys.}$	$\frac{d\sigma}{d\Omega} \pm \Delta\left(\frac{d\sigma}{d\Omega}\right)_{stat.} \pm \Delta\left(\frac{d\sigma}{d\Omega}\right)_{sys.}$
-0.95	$0.0349 \pm 0.0027 \pm 0.0034$	$0.1082 \pm 0.0053 \pm 0.0780$
-0.85	$0.0548 \pm 0.0035 \pm 0.0065$	$0.0740 \pm 0.0044 \pm 0.0527$
-0.75	$0.0725 \pm 0.0042 \pm 0.0065$	$0.0844 \pm 0.0048 \pm 0.0497$
-0.65	$0.0763 \pm 0.0045 \pm 0.0078$	$0.0947 \pm 0.0053 \pm 0.0052$
-0.55	$0.0903 \pm 0.0049 \pm 0.0068$	$0.1310 \pm 0.0062 \pm 0.0429$
-0.45	$0.1236 \pm 0.0060 \pm 0.0113$	$0.1223 \pm 0.0065 \pm 0.0345$
-0.35	$0.1349 \pm 0.0062 \pm 0.0155$	$0.1257 \pm 0.0065 \pm 0.0093$
-0.25	$0.1511 \pm 0.0066 \pm 0.0096$	$0.1361 \pm 0.0068 \pm 0.0048$
-0.15	$0.1966 \pm 0.0076 \pm 0.0091$	$0.1872 \pm 0.0077 \pm 0.0093$
-0.05	$0.2042 \pm 0.0078 \pm 0.0053$	$0.1561 \pm 0.0073 \pm 0.0242$
0.05	$0.2307 \pm 0.0085 \pm 0.0159$	$0.2035 \pm 0.0084 \pm 0.0108$
0.15	$0.1935 \pm 0.0076 \pm 0.0102$	$0.1934 \pm 0.0084 \pm 0.0295$
0.25	$0.2655 \pm 0.0094 \pm 0.0391$	$0.2437 \pm 0.0094 \pm 0.0216$
0.35	$0.2228 \pm 0.0087 \pm 0.0240$	$0.1722 \pm 0.0079 \pm 0.0112$
0.45	$0.2715 \pm 0.0101 \pm 0.0131$	$0.1880 \pm 0.0096 \pm 0.0175$
0.55	$0.1662 \pm 0.0086 \pm 0.0192$	$0.1388 \pm 0.0085 \pm 0.0094$
0.65	$0.1922 \pm 0.0101 \pm 0.0270$	$0.2115 \pm 0.0110 \pm 0.0277$
0.75	$0.0941 \pm 0.0077 \pm 0.0117$	$0.1999 \pm 0.0126 \pm 0.0162$
0.85	$0.1196 \pm 0.0097 \pm 0.0152$	$0.0320 \pm 0.0057 \pm 0.0322$
0.95	$0.1198 \pm 0.0127 \pm 0.0825$	$0.0000 \pm 0.0000 \pm 0.0000$

Table B.15: $\frac{d\sigma}{d\Omega}$, in $\mu\text{b}/\text{sr}$, for $E_\gamma = 1315$ and 1338 MeV from the $\eta \rightarrow 2\gamma$ decay mode.

$\cos\theta_\eta^*$	$E_\gamma = 1358 \text{ MeV}$	$E_\gamma = 1380 \text{ MeV}$
	$\frac{d\sigma}{d\Omega} \pm \Delta\left(\frac{d\sigma}{d\Omega}\right)_{stat.} \pm \Delta\left(\frac{d\sigma}{d\Omega}\right)_{sys.}$	$\frac{d\sigma}{d\Omega} \pm \Delta\left(\frac{d\sigma}{d\Omega}\right)_{stat.} \pm \Delta\left(\frac{d\sigma}{d\Omega}\right)_{sys.}$
-0.95	$0.0238 \pm 0.0023 \pm 0.0096$	$0.0151 \pm 0.0017 \pm 0.0215$
-0.85	$0.0405 \pm 0.0030 \pm 0.0215$	$0.0426 \pm 0.0029 \pm 0.0016$
-0.75	$0.0718 \pm 0.0041 \pm 0.0064$	$0.0355 \pm 0.0027 \pm 0.0019$
-0.65	$0.0902 \pm 0.0048 \pm 0.0077$	$0.0668 \pm 0.0037 \pm 0.0084$
-0.55	$0.1007 \pm 0.0052 \pm 0.0022$	$0.0760 \pm 0.0043 \pm 0.0041$
-0.45	$0.1339 \pm 0.0064 \pm 0.0113$	$0.0803 \pm 0.0044 \pm 0.0016$
-0.35	$0.1462 \pm 0.0065 \pm 0.0085$	$0.0865 \pm 0.0046 \pm 0.0059$
-0.25	$0.1577 \pm 0.0069 \pm 0.0073$	$0.0894 \pm 0.0047 \pm 0.0104$
-0.15	$0.1248 \pm 0.0060 \pm 0.0092$	$0.1477 \pm 0.0061 \pm 0.0069$
-0.05	$0.1617 \pm 0.0067 \pm 0.0099$	$0.1327 \pm 0.0060 \pm 0.0072$
0.05	$0.2191 \pm 0.0080 \pm 0.0102$	$0.1388 \pm 0.0060 \pm 0.0100$
0.15	$0.2001 \pm 0.0080 \pm 0.0262$	$0.1629 \pm 0.0069 \pm 0.0050$
0.25	$0.1734 \pm 0.0074 \pm 0.0137$	$0.1290 \pm 0.0059 \pm 0.0092$
0.35	$0.2193 \pm 0.0091 \pm 0.0102$	$0.1272 \pm 0.0066 \pm 0.0071$
0.45	$0.2140 \pm 0.0091 \pm 0.0114$	$0.1571 \pm 0.0070 \pm 0.0128$
0.55	$0.1689 \pm 0.0094 \pm 0.0462$	$0.0910 \pm 0.0061 \pm 0.0049$
0.65	$0.1742 \pm 0.0100 \pm 0.0200$	$0.1914 \pm 0.0094 \pm 0.0147$
0.75	$0.1261 \pm 0.0091 \pm 0.0309$	$0.1548 \pm 0.0100 \pm 0.0103$
0.85	$0.1527 \pm 0.0118 \pm 0.0601$	$0.1321 \pm 0.0103 \pm 0.0077$
0.95	$0.0904 \pm 0.0095 \pm 0.0507$	$0.2172 \pm 0.0185 \pm 0.1245$

Table B.16: $\frac{d\sigma}{d\Omega}$, in $\mu\text{b}/\text{sr}$, for $E_\gamma = 1358$ and 1380 MeV from the $\eta \rightarrow 2\gamma$ decay mode.

$\cos\theta_\eta^*$	$E_\gamma = 1396 \text{ MeV}$
	$\frac{d\sigma}{d\Omega} \pm \Delta\left(\frac{d\sigma}{d\Omega}\right)_{stat.} \pm \Delta\left(\frac{d\sigma}{d\Omega}\right)_{sys.}$
-0.95	$0.0286 \pm 0.0024 \pm 0.0035$
-0.85	$0.0374 \pm 0.0028 \pm 0.0033$
-0.75	$0.0488 \pm 0.0033 \pm 0.0155$
-0.65	$0.0694 \pm 0.0041 \pm 0.0068$
-0.55	$0.0731 \pm 0.0043 \pm 0.0036$
-0.45	$0.0719 \pm 0.0044 \pm 0.0453$
-0.35	$0.0762 \pm 0.0046 \pm 0.0063$
-0.25	$0.0880 \pm 0.0049 \pm 0.0066$
-0.15	$0.0948 \pm 0.0053 \pm 0.0380$
-0.05	$0.0826 \pm 0.0049 \pm 0.0638$
0.05	$0.0000 \pm 0.0000 \pm 0.0000$
0.15	$0.1020 \pm 0.0057 \pm 0.0085$
0.25	$0.1104 \pm 0.0062 \pm 0.0065$
0.35	$0.1115 \pm 0.0060 \pm 0.0092$
0.45	$0.1094 \pm 0.0065 \pm 0.0031$
0.55	$0.1188 \pm 0.0071 \pm 0.0051$
0.65	$0.0734 \pm 0.0067 \pm 0.0112$
0.75	$0.1282 \pm 0.0099 \pm 0.0187$
0.85	$0.0217 \pm 0.0046 \pm 0.0036$
0.95	$0.1723 \pm 0.0194 \pm 0.0265$

Table B.17: $\frac{d\sigma}{d\Omega}$, in $\mu\text{b/sr}$, for $E_\gamma = 1396 \text{ MeV}$ from the $\eta \rightarrow 2\gamma$ decay mode.

Appendix C

Tables of $\eta \rightarrow 6\gamma$ Results

Differential cross-sections, $\frac{d\sigma}{d\Omega}$, of η photoproduction are presented for the decay mode $\eta \rightarrow 3\pi^0 \rightarrow 6\gamma$ in the incident photon energy range $703 \leq E_\gamma \leq 1403$ MeV for $-1 \leq \cos\theta_\eta^* \leq 1$. Lower and upper bounds are listed with average values of E_γ and $\cos\theta_\eta^*$ bins, respectively in tables B.1 and C.1. Differential cross-sections, with statistical and systematic errors, are listed in tables C.2 to C.16.

Avg. $\cos \theta_\eta^*$	Min. $\cos \theta_\eta^*$	Max. $\cos \theta_\eta^*$
-0.90	-1.00	-0.80
-0.70	-0.80	-0.60
-0.50	-0.60	-0.40
-0.30	-0.40	-0.20
-0.10	-0.20	0.00
0.10	0.00	0.20
0.30	0.20	0.40
0.50	0.40	0.60
0.70	0.60	0.80
0.90	0.80	1.00

Table C.1: Minimum, maximum and average values for each $\cos \theta_\eta^*$ bin used in the 6γ analysis.

$\cos \theta_\eta^*$	$E_\gamma = 718 \text{ MeV}$	$E_\gamma = 747 \text{ MeV}$
	$\frac{d\sigma}{d\Omega} \pm \Delta \left(\frac{d\sigma}{d\Omega} \right)_{stat.} \pm \Delta \left(\frac{d\sigma}{d\Omega} \right)_{sys.}$	$\frac{d\sigma}{d\Omega} \pm \Delta \left(\frac{d\sigma}{d\Omega} \right)_{stat.} \pm \Delta \left(\frac{d\sigma}{d\Omega} \right)_{sys.}$
-0.90	$0.4099 \pm 0.0017 \pm 0.0601$	$0.8747 \pm 0.0029 \pm 0.0399$
-0.70	$0.5135 \pm 0.0021 \pm 0.0415$	$0.9935 \pm 0.0033 \pm 0.0165$
-0.50	$0.5448 \pm 0.0022 \pm 0.0063$	$0.9812 \pm 0.0032 \pm 0.0527$
-0.30	$0.5793 \pm 0.0023 \pm 0.0017$	$1.0839 \pm 0.0036 \pm 0.0809$
-0.10	$0.6471 \pm 0.0026 \pm 0.0371$	$1.0367 \pm 0.0035 \pm 0.0224$
0.10	$0.6599 \pm 0.0026 \pm 0.0403$	$1.0403 \pm 0.0034 \pm 0.0675$
0.30	$0.6963 \pm 0.0028 \pm 0.0110$	$1.0660 \pm 0.0036 \pm 0.1137$
0.50	$0.6251 \pm 0.0025 \pm 0.0334$	$1.0821 \pm 0.0036 \pm 0.0911$
0.70	$0.6381 \pm 0.0026 \pm 0.0378$	$1.2223 \pm 0.0040 \pm 0.1164$
0.90	$0.7242 \pm 0.0029 \pm 0.0281$	$1.0842 \pm 0.0036 \pm 0.0332$

Table C.2: $\frac{d\sigma}{d\Omega}$, in $\mu\text{b}/\text{sr}$, for $E_\gamma = 718$ and 747 MeV from the $\eta \rightarrow 6\gamma$ decay mode.

$\cos\theta_\eta^*$	$E_\gamma = 778$ MeV	$E_\gamma = 805$ MeV
	$\frac{d\sigma}{d\Omega} \pm \Delta\left(\frac{d\sigma}{d\Omega}\right)_{stat.} \pm \Delta\left(\frac{d\sigma}{d\Omega}\right)_{sys.}$	$\frac{d\sigma}{d\Omega} \pm \Delta\left(\frac{d\sigma}{d\Omega}\right)_{stat.} \pm \Delta\left(\frac{d\sigma}{d\Omega}\right)_{sys.}$
-0.90	$1.0676 \pm 0.0035 \pm 0.0812$	$1.0585 \pm 0.0035 \pm 0.1268$
-0.70	$1.2268 \pm 0.0041 \pm 0.0557$	$1.0770 \pm 0.0036 \pm 0.0466$
-0.50	$1.1432 \pm 0.0038 \pm 0.0150$	$1.1742 \pm 0.0040 \pm 0.1006$
-0.30	$1.1737 \pm 0.0039 \pm 0.0769$	$1.3424 \pm 0.0045 \pm 0.0373$
-0.10	$1.2382 \pm 0.0041 \pm 0.0998$	$1.2229 \pm 0.0041 \pm 0.0428$
0.10	$1.2527 \pm 0.0041 \pm 0.0304$	$1.2331 \pm 0.0041 \pm 0.0819$
0.30	$1.3353 \pm 0.0044 \pm 0.0544$	$1.1247 \pm 0.0038 \pm 0.0219$
0.50	$1.3558 \pm 0.0045 \pm 0.0137$	$1.1010 \pm 0.0037 \pm 0.1176$
0.70	$1.5177 \pm 0.0050 \pm 0.0301$	$1.1453 \pm 0.0039 \pm 0.0665$
0.90	$0.9673 \pm 0.0032 \pm 0.1210$	$1.1847 \pm 0.0039 \pm 0.0425$

 Table C.3: $\frac{d\sigma}{d\Omega}$, in $\mu\text{b}/\text{sr}$, for $E_\gamma = 778$ and 805 MeV from the $\eta \rightarrow 6\gamma$ decay mode.

$\cos\theta_\eta^*$	$E_\gamma = 833$ MeV	$E_\gamma = 863$ MeV
	$\frac{d\sigma}{d\Omega} \pm \Delta\left(\frac{d\sigma}{d\Omega}\right)_{stat.} \pm \Delta\left(\frac{d\sigma}{d\Omega}\right)_{sys.}$	$\frac{d\sigma}{d\Omega} \pm \Delta\left(\frac{d\sigma}{d\Omega}\right)_{stat.} \pm \Delta\left(\frac{d\sigma}{d\Omega}\right)_{sys.}$
-0.90	$0.9334 \pm 0.0031 \pm 0.1154$	$0.8661 \pm 0.0029 \pm 0.0084$
-0.70	$1.0797 \pm 0.0036 \pm 0.0363$	$0.9453 \pm 0.0032 \pm 0.0472$
-0.50	$1.0959 \pm 0.0037 \pm 0.0131$	$0.9242 \pm 0.0031 \pm 0.0523$
-0.30	$1.1229 \pm 0.0037 \pm 0.0389$	$0.9983 \pm 0.0033 \pm 0.0355$
-0.10	$1.0608 \pm 0.0035 \pm 0.0562$	$0.8591 \pm 0.0029 \pm 0.0271$
0.10	$1.1404 \pm 0.0038 \pm 0.0177$	$0.9852 \pm 0.0033 \pm 0.0423$
0.30	$1.0037 \pm 0.0033 \pm 0.1253$	$0.7507 \pm 0.0025 \pm 0.0521$
0.50	$0.9892 \pm 0.0033 \pm 0.0301$	$0.7239 \pm 0.0024 \pm 0.0254$
0.70	$0.8785 \pm 0.0029 \pm 0.0849$	$0.7055 \pm 0.0024 \pm 0.1210$
0.90	$1.0515 \pm 0.0035 \pm 0.0453$	$0.8445 \pm 0.0028 \pm 0.0420$

 Table C.4: $\frac{d\sigma}{d\Omega}$, in $\mu\text{b}/\text{sr}$, for $E_\gamma = 833$ and 863 MeV from the $\eta \rightarrow 6\gamma$ decay mode.

$\cos\theta_\eta^*$	$E_\gamma = 890$ MeV	$E_\gamma = 918$ MeV
	$\frac{d\sigma}{d\Omega} \pm \Delta\left(\frac{d\sigma}{d\Omega}\right)_{stat.} \pm \Delta\left(\frac{d\sigma}{d\Omega}\right)_{sys.}$	$\frac{d\sigma}{d\Omega} \pm \Delta\left(\frac{d\sigma}{d\Omega}\right)_{stat.} \pm \Delta\left(\frac{d\sigma}{d\Omega}\right)_{sys.}$
-0.90	$0.7564 \pm 0.0025 \pm 0.0418$	$0.5847 \pm 0.0019 \pm 0.0419$
-0.70	$0.7968 \pm 0.0027 \pm 0.0484$	$0.6835 \pm 0.0023 \pm 0.0335$
-0.50	$0.9501 \pm 0.0031 \pm 0.0303$	$0.7493 \pm 0.0025 \pm 0.0254$
-0.30	$0.9210 \pm 0.0030 \pm 0.1145$	$0.7591 \pm 0.0025 \pm 0.0396$
-0.10	$0.9074 \pm 0.0030 \pm 0.0357$	$0.6749 \pm 0.0023 \pm 0.0286$
0.10	$0.7049 \pm 0.0024 \pm 0.0619$	$0.6218 \pm 0.0021 \pm 0.0234$
0.30	$0.6749 \pm 0.0022 \pm 0.1324$	$0.6872 \pm 0.0023 \pm 0.1337$
0.50	$0.6816 \pm 0.0023 \pm 0.1090$	$0.5019 \pm 0.0016 \pm 0.0297$
0.70	$0.5794 \pm 0.0019 \pm 0.0262$	$0.3330 \pm 0.0011 \pm 0.0472$
0.90	$0.5304 \pm 0.0018 \pm 0.0652$	$0.1610 \pm 0.0005 \pm 0.0324$

 Table C.5: $\frac{d\sigma}{d\Omega}$, in $\mu\text{b}/\text{sr}$, for $E_\gamma = 890$ and 918 MeV from the $\eta \rightarrow 6\gamma$ decay mode.

$\cos\theta_\eta^*$	$E_\gamma = 945$ MeV	$E_\gamma = 972$ MeV
	$\frac{d\sigma}{d\Omega} \pm \Delta\left(\frac{d\sigma}{d\Omega}\right)_{stat.} \pm \Delta\left(\frac{d\sigma}{d\Omega}\right)_{sys.}$	$\frac{d\sigma}{d\Omega} \pm \Delta\left(\frac{d\sigma}{d\Omega}\right)_{stat.} \pm \Delta\left(\frac{d\sigma}{d\Omega}\right)_{sys.}$
-0.90	$0.4782 \pm 0.0016 \pm 0.0233$	$0.3717 \pm 0.0012 \pm 0.0246$
-0.70	$0.5831 \pm 0.0020 \pm 0.0340$	$0.4657 \pm 0.0015 \pm 0.0517$
-0.50	$0.5654 \pm 0.0019 \pm 0.0121$	$0.4692 \pm 0.0015 \pm 0.0358$
-0.30	$0.5303 \pm 0.0017 \pm 0.0492$	$0.3838 \pm 0.0013 \pm 0.0079$
-0.10	$0.5450 \pm 0.0018 \pm 0.0107$	$0.4405 \pm 0.0015 \pm 0.0338$
0.10	$0.4683 \pm 0.0016 \pm 0.0203$	$0.3223 \pm 0.0011 \pm 0.0394$
0.30	$0.4232 \pm 0.0014 \pm 0.0687$	$0.2893 \pm 0.0010 \pm 0.0225$
0.50	$0.3695 \pm 0.0012 \pm 0.0495$	$0.1864 \pm 0.0006 \pm 0.0153$
0.70	$0.2664 \pm 0.0009 \pm 0.0255$	$0.1676 \pm 0.0006 \pm 0.0467$
0.90	$0.1958 \pm 0.0007 \pm 0.0793$	$0.1846 \pm 0.0006 \pm 0.0466$

 Table C.6: $\frac{d\sigma}{d\Omega}$, in $\mu\text{b}/\text{sr}$, for $E_\gamma = 945$ and 972 MeV from the $\eta \rightarrow 6\gamma$ decay mode.

$\cos\theta_\eta^*$	$E_\gamma = 999 \text{ MeV}$	$E_\gamma = 1024 \text{ MeV}$
	$\frac{d\sigma}{d\Omega} \pm \Delta \left(\frac{d\sigma}{d\Omega} \right)_{stat.} \pm \Delta \left(\frac{d\sigma}{d\Omega} \right)_{sys.}$	$\frac{d\sigma}{d\Omega} \pm \Delta \left(\frac{d\sigma}{d\Omega} \right)_{stat.} \pm \Delta \left(\frac{d\sigma}{d\Omega} \right)_{sys.}$
-0.90	$0.2702 \pm 0.0009 \pm 0.0192$	$0.2267 \pm 0.0008 \pm 0.0052$
-0.70	$0.3360 \pm 0.0011 \pm 0.0103$	$0.2397 \pm 0.0008 \pm 0.0248$
-0.50	$0.3745 \pm 0.0012 \pm 0.0147$	$0.3023 \pm 0.0010 \pm 0.0040$
-0.30	$0.3415 \pm 0.0011 \pm 0.0160$	$0.3067 \pm 0.0010 \pm 0.0270$
-0.10	$0.3394 \pm 0.0011 \pm 0.0157$	$0.2674 \pm 0.0009 \pm 0.0338$
0.10	$0.3410 \pm 0.0011 \pm 0.0353$	$0.2280 \pm 0.0008 \pm 0.0082$
0.30	$0.2679 \pm 0.0009 \pm 0.0189$	$0.2476 \pm 0.0008 \pm 0.0135$
0.50	$0.1673 \pm 0.0006 \pm 0.0230$	$0.1832 \pm 0.0006 \pm 0.0196$
0.70	$0.3238 \pm 0.0011 \pm 0.2064$	$0.1359 \pm 0.0005 \pm 0.0990$
0.90	$0.1433 \pm 0.0005 \pm 0.0260$	$0.0700 \pm 0.0002 \pm 0.0724$

 Table C.7: $\frac{d\sigma}{d\Omega}$, in $\mu\text{b}/\text{sr}$, for $E_\gamma = 999$ and 1024 MeV from the $\eta \rightarrow 6\gamma$ decay mode.

$\cos\theta_\eta^*$	$E_\gamma = 1050 \text{ MeV}$	$E_\gamma = 1075 \text{ MeV}$
	$\frac{d\sigma}{d\Omega} \pm \Delta \left(\frac{d\sigma}{d\Omega} \right)_{stat.} \pm \Delta \left(\frac{d\sigma}{d\Omega} \right)_{sys.}$	$\frac{d\sigma}{d\Omega} \pm \Delta \left(\frac{d\sigma}{d\Omega} \right)_{stat.} \pm \Delta \left(\frac{d\sigma}{d\Omega} \right)_{sys.}$
-0.90	$0.1524 \pm 0.0005 \pm 0.0048$	$0.1777 \pm 0.0006 \pm 0.0105$
-0.70	$0.2621 \pm 0.0009 \pm 0.0198$	$0.2107 \pm 0.0007 \pm 0.0217$
-0.50	$0.2424 \pm 0.0008 \pm 0.0145$	$0.2706 \pm 0.0009 \pm 0.0219$
-0.30	$0.2585 \pm 0.0009 \pm 0.0128$	$0.2302 \pm 0.0008 \pm 0.0149$
-0.10	$0.2559 \pm 0.0009 \pm 0.0102$	$0.2847 \pm 0.0010 \pm 0.0126$
0.10	$0.2705 \pm 0.0009 \pm 0.0074$	$0.2963 \pm 0.0010 \pm 0.0051$
0.30	$0.2596 \pm 0.0009 \pm 0.0091$	$0.3021 \pm 0.0010 \pm 0.0158$
0.50	$0.1987 \pm 0.0007 \pm 0.0242$	$0.1905 \pm 0.0006 \pm 0.0323$
0.70	$0.2092 \pm 0.0007 \pm 0.0823$	$0.3074 \pm 0.0010 \pm 0.1034$
0.90	$0.1629 \pm 0.0005 \pm 0.0741$	$0.1225 \pm 0.0004 \pm 0.0703$

 Table C.8: $\frac{d\sigma}{d\Omega}$, in $\mu\text{b}/\text{sr}$, for $E_\gamma = 1050$ and 1075 MeV from the $\eta \rightarrow 6\gamma$ decay mode.

$\cos\theta_\eta^*$	$E_\gamma = 1100 \text{ MeV}$	$E_\gamma = 1124 \text{ MeV}$
	$\frac{d\sigma}{d\Omega} \pm \Delta \left(\frac{d\sigma}{d\Omega} \right)_{stat.} \pm \Delta \left(\frac{d\sigma}{d\Omega} \right)_{sys.}$	$\frac{d\sigma}{d\Omega} \pm \Delta \left(\frac{d\sigma}{d\Omega} \right)_{stat.} \pm \Delta \left(\frac{d\sigma}{d\Omega} \right)_{sys.}$
-0.90	$0.1225 \pm 0.0004 \pm 0.0373$	$0.0882 \pm 0.0003 \pm 0.0094$
-0.70	$0.1624 \pm 0.0005 \pm 0.0086$	$0.1554 \pm 0.0005 \pm 0.0064$
-0.50	$0.2308 \pm 0.0008 \pm 0.0309$	$0.2259 \pm 0.0008 \pm 0.0303$
-0.30	$0.2485 \pm 0.0008 \pm 0.0215$	$0.2308 \pm 0.0008 \pm 0.0109$
-0.10	$0.2609 \pm 0.0009 \pm 0.0358$	$0.2746 \pm 0.0009 \pm 0.0605$
0.10	$0.3297 \pm 0.0011 \pm 0.0177$	$0.3306 \pm 0.0011 \pm 0.0284$
0.30	$0.2785 \pm 0.0009 \pm 0.0262$	$0.3078 \pm 0.0010 \pm 0.0032$
0.50	$0.1898 \pm 0.0006 \pm 0.0391$	$0.2612 \pm 0.0009 \pm 0.0241$
0.70	$0.2285 \pm 0.0008 \pm 0.0574$	$0.2933 \pm 0.0010 \pm 0.0253$
0.90	$0.1678 \pm 0.0006 \pm 0.0891$	$0.2712 \pm 0.0009 \pm 0.1259$

 Table C.9: $\frac{d\sigma}{d\Omega}$, in $\mu\text{b}/\text{sr}$, for $E_\gamma = 1100$ and 1124 MeV from the $\eta \rightarrow 6\gamma$ decay mode.

$\cos\theta_\eta^*$	$E_\gamma = 1147 \text{ MeV}$	$E_\gamma = 1171 \text{ MeV}$
	$\frac{d\sigma}{d\Omega} \pm \Delta \left(\frac{d\sigma}{d\Omega} \right)_{stat.} \pm \Delta \left(\frac{d\sigma}{d\Omega} \right)_{sys.}$	$\frac{d\sigma}{d\Omega} \pm \Delta \left(\frac{d\sigma}{d\Omega} \right)_{stat.} \pm \Delta \left(\frac{d\sigma}{d\Omega} \right)_{sys.}$
-0.90	$0.0868 \pm 0.0003 \pm 0.0074$	$0.0697 \pm 0.0002 \pm 0.0166$
-0.70	$0.1247 \pm 0.0004 \pm 0.0093$	$0.1329 \pm 0.0004 \pm 0.0225$
-0.50	$0.1945 \pm 0.0006 \pm 0.0164$	$0.1753 \pm 0.0006 \pm 0.0120$
-0.30	$0.1833 \pm 0.0006 \pm 0.0163$	$0.2028 \pm 0.0007 \pm 0.0087$
-0.10	$0.2751 \pm 0.0009 \pm 0.0212$	$0.2123 \pm 0.0007 \pm 0.0083$
0.10	$0.2961 \pm 0.0010 \pm 0.0218$	$0.2625 \pm 0.0009 \pm 0.0108$
0.30	$0.2404 \pm 0.0008 \pm 0.0402$	$0.2685 \pm 0.0009 \pm 0.0407$
0.50	$0.2014 \pm 0.0007 \pm 0.0231$	$0.1704 \pm 0.0006 \pm 0.0205$
0.70	$0.1736 \pm 0.0006 \pm 0.1098$	$0.2156 \pm 0.0007 \pm 0.0152$
0.90	$0.2055 \pm 0.0007 \pm 0.1039$	$0.2260 \pm 0.0008 \pm 0.1264$

 Table C.10: $\frac{d\sigma}{d\Omega}$, in $\mu\text{b}/\text{sr}$, for $E_\gamma = 1147$ and 1171 MeV from the $\eta \rightarrow 6\gamma$ decay mode.

$\cos\theta_\eta^*$	$E_\gamma = 1193 \text{ MeV}$	$E_\gamma = 1215 \text{ MeV}$
	$\frac{d\sigma}{d\Omega} \pm \Delta\left(\frac{d\sigma}{d\Omega}\right)_{stat.} \pm \Delta\left(\frac{d\sigma}{d\Omega}\right)_{sys.}$	$\frac{d\sigma}{d\Omega} \pm \Delta\left(\frac{d\sigma}{d\Omega}\right)_{stat.} \pm \Delta\left(\frac{d\sigma}{d\Omega}\right)_{sys.}$
-0.90	$0.0658 \pm 0.0002 \pm 0.0389$	$0.0853 \pm 0.0003 \pm 0.0023$
-0.70	$0.0887 \pm 0.0003 \pm 0.0047$	$0.1125 \pm 0.0004 \pm 0.0216$
-0.50	$0.1892 \pm 0.0006 \pm 0.0449$	$0.1563 \pm 0.0005 \pm 0.0184$
-0.30	$0.1595 \pm 0.0005 \pm 0.0208$	$0.1830 \pm 0.0006 \pm 0.0188$
-0.10	$0.2098 \pm 0.0007 \pm 0.0307$	$0.1913 \pm 0.0006 \pm 0.0283$
0.10	$0.2394 \pm 0.0008 \pm 0.0157$	$0.2329 \pm 0.0008 \pm 0.0015$
0.30	$0.2083 \pm 0.0007 \pm 0.0248$	$0.1690 \pm 0.0006 \pm 0.0284$
0.50	$0.2306 \pm 0.0008 \pm 0.0092$	$0.2896 \pm 0.0010 \pm 0.1237$
0.70	$0.3205 \pm 0.0011 \pm 0.0775$	$0.2347 \pm 0.0008 \pm 0.0632$
0.90	$0.1859 \pm 0.0006 \pm 0.1088$	

Table C.11: $\frac{d\sigma}{d\Omega}$, in $\mu\text{b}/\text{sr}$, for $E_\gamma = 1193$ and 1215 MeV from the $\eta \rightarrow 6\gamma$ decay mode.

$\cos\theta_\eta^*$	$E_\gamma = 1236 \text{ MeV}$	$E_\gamma = 1257 \text{ MeV}$
	$\frac{d\sigma}{d\Omega} \pm \Delta\left(\frac{d\sigma}{d\Omega}\right)_{stat.} \pm \Delta\left(\frac{d\sigma}{d\Omega}\right)_{sys.}$	$\frac{d\sigma}{d\Omega} \pm \Delta\left(\frac{d\sigma}{d\Omega}\right)_{stat.} \pm \Delta\left(\frac{d\sigma}{d\Omega}\right)_{sys.}$
-0.90	$0.0507 \pm 0.0002 \pm 0.0281$	$0.0505 \pm 0.0002 \pm 0.0020$
-0.70	$0.0957 \pm 0.0003 \pm 0.0550$	$0.1310 \pm 0.0004 \pm 0.0181$
-0.50	$0.1446 \pm 0.0005 \pm 0.0264$	$0.1241 \pm 0.0004 \pm 0.0044$
-0.30	$0.1727 \pm 0.0006 \pm 0.0104$	$0.1739 \pm 0.0006 \pm 0.0141$
-0.10	$0.2264 \pm 0.0007 \pm 0.0274$	$0.2198 \pm 0.0007 \pm 0.0337$
0.10	$0.2413 \pm 0.0008 \pm 0.0245$	$0.1760 \pm 0.0006 \pm 0.0563$
0.30	$0.1853 \pm 0.0006 \pm 0.0234$	$0.2297 \pm 0.0008 \pm 0.0368$
0.50	$0.1826 \pm 0.0006 \pm 0.0056$	$0.1680 \pm 0.0006 \pm 0.0017$
0.70	$0.2119 \pm 0.0007 \pm 0.1189$	$0.1681 \pm 0.0006 \pm 0.0853$

Table C.12: $\frac{d\sigma}{d\Omega}$, in $\mu\text{b}/\text{sr}$, for $E_\gamma = 1236$ and 1257 MeV from the $\eta \rightarrow 6\gamma$ decay mode.

$\cos\theta_\eta^*$	$E_\gamma = 1277 \text{ MeV}$	$E_\gamma = 1297 \text{ MeV}$
	$\frac{d\sigma}{d\Omega} \pm \Delta\left(\frac{d\sigma}{d\Omega}\right)_{stat.} \pm \Delta\left(\frac{d\sigma}{d\Omega}\right)_{sys.}$	$\frac{d\sigma}{d\Omega} \pm \Delta\left(\frac{d\sigma}{d\Omega}\right)_{stat.} \pm \Delta\left(\frac{d\sigma}{d\Omega}\right)_{sys.}$
-0.90	$0.0543 \pm 0.0002 \pm 0.0373$	$0.0943 \pm 0.0003 \pm 0.0096$
-0.70	$0.1270 \pm 0.0004 \pm 0.0116$	$0.0730 \pm 0.0002 \pm 0.0509$
-0.50	$0.0989 \pm 0.0003 \pm 0.0141$	$0.1422 \pm 0.0005 \pm 0.0132$
-0.30	$0.1788 \pm 0.0006 \pm 0.0103$	$0.1447 \pm 0.0005 \pm 0.0041$
-0.10	$0.2042 \pm 0.0007 \pm 0.0062$	$0.2137 \pm 0.0007 \pm 0.0400$
0.10	$0.1715 \pm 0.0006 \pm 0.0123$	$0.1706 \pm 0.0006 \pm 0.0100$
0.30	$0.1810 \pm 0.0006 \pm 0.0150$	$0.1933 \pm 0.0006 \pm 0.0204$
0.50	$0.1150 \pm 0.0004 \pm 0.0421$	$0.2685 \pm 0.0009 \pm 0.0159$
0.70	$0.2296 \pm 0.0008 \pm 0.1317$	$0.2454 \pm 0.0008 \pm 0.1385$

Table C.13: $\frac{d\sigma}{d\Omega}$, in $\mu\text{b}/\text{sr}$, for $E_\gamma = 1277$ and 1297 MeV from the $\eta \rightarrow 6\gamma$ decay mode.

$\cos\theta_\eta^*$	$E_\gamma = 1315 \text{ MeV}$	$E_\gamma = 1338 \text{ MeV}$
	$\frac{d\sigma}{d\Omega} \pm \Delta\left(\frac{d\sigma}{d\Omega}\right)_{stat.} \pm \Delta\left(\frac{d\sigma}{d\Omega}\right)_{sys.}$	$\frac{d\sigma}{d\Omega} \pm \Delta\left(\frac{d\sigma}{d\Omega}\right)_{stat.} \pm \Delta\left(\frac{d\sigma}{d\Omega}\right)_{sys.}$
-0.90	$0.0984 \pm 0.0003 \pm 0.0074$	$0.0491 \pm 0.0002 \pm 0.0194$
-0.70	$0.1157 \pm 0.0004 \pm 0.0140$	$0.1411 \pm 0.0005 \pm 0.0751$
-0.50	$0.1465 \pm 0.0005 \pm 0.0545$	$0.0879 \pm 0.0003 \pm 0.0056$
-0.30	$0.1784 \pm 0.0006 \pm 0.0041$	$0.1344 \pm 0.0004 \pm 0.0095$
-0.10	$0.2336 \pm 0.0008 \pm 0.0170$	$0.1519 \pm 0.0005 \pm 0.0247$
0.10	$0.1893 \pm 0.0006 \pm 0.0249$	$0.2347 \pm 0.0008 \pm 0.0311$
0.30	$0.1679 \pm 0.0006 \pm 0.0050$	$0.1333 \pm 0.0004 \pm 0.0284$
0.50	$0.3218 \pm 0.0011 \pm 0.1715$	$0.1582 \pm 0.0005 \pm 0.0318$

Table C.14: $\frac{d\sigma}{d\Omega}$, in $\mu\text{b}/\text{sr}$, for $E_\gamma = 1315$ and 1338 MeV from the $\eta \rightarrow 6\gamma$ decay mode.

$\cos\theta_\eta^*$	$E_\gamma = 1358 \text{ MeV}$	$E_\gamma = 1380 \text{ MeV}$
	$\frac{d\sigma}{d\Omega} \pm \Delta\left(\frac{d\sigma}{d\Omega}\right)_{stat.} \pm \Delta\left(\frac{d\sigma}{d\Omega}\right)_{sys.}$	$\frac{d\sigma}{d\Omega} \pm \Delta\left(\frac{d\sigma}{d\Omega}\right)_{stat.} \pm \Delta\left(\frac{d\sigma}{d\Omega}\right)_{sys.}$
-0.90	$0.0522 \pm 0.0002 \pm 0.0242$	$0.0437 \pm 0.0001 \pm 0.0148$
-0.70	$0.0773 \pm 0.0003 \pm 0.0170$	$0.0533 \pm 0.0002 \pm 0.0068$
-0.50	$0.1484 \pm 0.0005 \pm 0.0169$	$0.0527 \pm 0.0002 \pm 0.0136$
-0.30	$0.1221 \pm 0.0004 \pm 0.0033$	$0.1131 \pm 0.0004 \pm 0.0113$
-0.10	$0.1354 \pm 0.0004 \pm 0.0159$	$0.1266 \pm 0.0004 \pm 0.0104$
0.10	$0.1412 \pm 0.0005 \pm 0.0389$	$0.1198 \pm 0.0004 \pm 0.0749$
0.30	$0.1249 \pm 0.0004 \pm 0.0339$	$0.1863 \pm 0.0006 \pm 0.0148$
0.50	$0.1350 \pm 0.0004 \pm 0.1065$	$0.2072 \pm 0.0007 \pm 0.0253$

Table C.15: $\frac{d\sigma}{d\Omega}$, in $\mu\text{b}/\text{sr}$, for $E_\gamma = 1358$ and 1380 MeV from the $\eta \rightarrow 6\gamma$ decay mode.

$\cos\theta_\eta^*$	$E_\gamma = 1396 \text{ MeV}$
	$\frac{d\sigma}{d\Omega} \pm \Delta\left(\frac{d\sigma}{d\Omega}\right)_{stat.} \pm \Delta\left(\frac{d\sigma}{d\Omega}\right)_{sys.}$
-0.90	$0.0603 \pm 0.0002 \pm 0.0113$
-0.70	$0.0530 \pm 0.0002 \pm 0.0034$
-0.50	$0.0926 \pm 0.0003 \pm 0.0090$
-0.30	$0.1152 \pm 0.0004 \pm 0.0236$
-0.10	$0.0852 \pm 0.0003 \pm 0.0124$
0.10	$0.0000 \pm 0.0000 \pm 0.0000$
0.30	$0.1001 \pm 0.0003 \pm 0.0649$
0.50	$0.1720 \pm 0.0006 \pm 0.1337$

Table C.16: $\frac{d\sigma}{d\Omega}$, in $\mu\text{b}/\text{sr}$, for $E_\gamma = 1396 \text{ MeV}$ from the $\eta \rightarrow 6\gamma$ decay mode.